REYNOLDS STRESS MEASUREMENTS IN A TURBINE TIP LEAKAGE VORTEX

by

Scott P. Heckel

Thesis submitted to the Faculty of the
Virginia Polytechnic Institute and State University
in partial fulfillment of the requirements for the degree of

MASTER OF SCIENCE
in
Mechanical Engineering

Approved:

J. Moore, Chairman

E.F. Brown

F.J. Pierce

December 1992

Blacksburg, Virginia

Reynolds Stress Measurements in a Turbine Tip Leakage Vortex

by

Scott P. Heckel

Committee Chairman: Dr. John Moore

Mechanical Engineering

(ABSTRACT)

An experimental study of the structure of turbulence in a tip leakage vortex was conducted in a large scale, linear turbine cascade. The study was performed in a cross sectional plane 0.96 of the axial chord length downstream of the blade leading edge. The cascade consisted of five blades with an aspect ratio of one and an axial chord of 235.2 mm. The tip clearance gap was nominally 2.1% of the blade span.

A specially designed rotatable x-wire hot wire probe with high spatial resolution was used to measure both the mean velocity distribution and all six components of the Reynolds stress tensor. An automated probe positioning and digital signal processing system was developed to facilitate quick, accurate measurements at a large number of data points. A geared stepper-motor drive mechanism was used to rotate the endflow hot-wire probe about its axis. Performance of the probe and the data analysis routines was verified by measurements in a fully developed pipe flow.

The contribution of turbulence to the overall losses was investigated by studying both the general level of turbulence and the work done on the fluid by the turbulence stresses . This allowed the study of the physical mechanisms of loss production;

spanwise mixing processes were found to be major contributors. The high level of turbulence in the tip leakage vortex was found to amount to about 36% of the total pressure loss generated by the plane near the blade trailing edge.

Acknowledgments

I owe a debt of gratitude to my advisor, Dr. John Moore, whose guidance through this project has been indispensable. His belief of being a "student of nature" has helped me to understand even the most complicated concepts encountered in this work by investigating the fundamental physics behind them. I also thank Joan Moore for the assistance she freely gave in computer programming and in the preparation of this thesis.

I would also like to thank Dr. Brown and Dr. Pierce for reviewing this thesis and serving on my examining committee. I greatly admire the professionalism of the Faculty of the Mechanical Engineering Department for their commitment to excellence in teaching. Each course that I have taken at Virginia Tech has proved to be better than I had hoped for.

My deepest thanks go to my wife, Cheryl, and daughter, Layla, for their endless patience and support throughout my education. My gratitude also goes out to the late Elaine Scott for her enthusiasm and belief in my potential. Finally, I would like to thank my parents for supporting and standing behind me.

Table of Contents

Nomenclature

A	Flow area
a	Wire linearity calibration constant, Eq. (II8), Pipe Radius, Fig. 22
(AX, N1, N2)	Wire coordinate directions, Fig D1
c	Blade axial chord, Fig. 9
C_{Pt}	Total pressure loss coeficient, Eq. (II6)
E,e	Mean and fluctuating wire voltages
$(\hat{i}, \hat{j}, \hat{k})$	Fixed coordinate directions, Fig. D1
ℓ/d	Ratio of wire effective length to diameter
N	nondimensionalization factor: $N = \frac{c}{\frac{1}{2}\overline{V_n} A \rho U_0^2}$, Eq. (V4)
n	Frequency, Fig. 29
k^2	Wire angular calibration constant, Eq. (II8)
P,p	Mean and fluctuating static pressure
Q,q	Mean and fluctuating effective cooling velocity
Q_0	Velocity magnitude, Eq. (II8)
Q_{ref}	Reference position velocity magnitude
(r, θ, z)	Pipe coordinate directions, Fig. 22
r'	Measurement coordinate in pipe, Fig. 22
TKE	Turbulence kinetic energy, Eq. (II3)
T_u	rms turbulence intensity, Eq.(II3)
U,u	Mean and fluctuating primary velocity components, Fig. 10
U_{max}	Pipe centerline velocity

U_0	Upstream freestream velocity
U_τ	Pipe shear velocity ($\equiv\sqrt{\tau_0/\rho}$), Eq. (A3)
$\overline{u^2}, \overline{v^2}, \overline{w^2}$	Turbulent (Reynolds) normal stresses, Eq. (II1)
$\overline{uv}, \overline{uw}, \overline{vw}$	Turbulent (Reynolds) shear stresses, Eq. (II1)
V,v	Mean and fluctuating pitchwise velocity components, Fig. 10
V_n	Velocity component normal to measurement plane, Fig. 10, axial velocity
W,w	Mean and fluctuating spanise velocity components, Fig. 10
(X, Y, Z)	Cascade coordinate directions, Fig. 9
(x, y, z)	Flow Coordinates, Fig. 11
ΔY	Blade pitch, Fig. 9
ΔZ	Blade span, Fig. 9
ΔP	Static pressure drop along 5.9 meters of pipe, Eq. (A1)
α_0, α_w	Wire angles, Fig. D1,D2
α'_0, α'_w	Measured wire angles, Fig. D2
α_r, α_p	Flow angles relative to fixed coordinates, Fig. C1
β_1, β_2	Cascade blade mean camber line angles, Fig. 9
δ	Boundary layer thickness
μ	Absolute viscosity
ρ	Density
τ_0	Pipe wall shear stress, Eq. (A2)
Φ	Wire yaw angle, Eq. (II8)
Φcone	Cone angle, Eq. (III1)

Subscripts

A,B	Wire designation
0	Property upstream of cascade in freestream flow
t	total, stagnation
s	static

Overbars

_	time averaged
=	mass averaged

List of Figures

List of Tables

Chapter I
Introduction

In order to improve the performance of axial flow turbomachinery a solid understanding of the physical mechanisms which produce losses is required. An understanding of these loss production mechanisms can enable the design of turbomachinery with increased efficiency.

A major source of losses is tip leakage flow. Tip leakage flow results from blade loading and the necessary gap between the tips of a rotor and the annular casing. The pressure gradient from the pressure to the suction side of a blade causes the fluid to flow between the blade tip and the casing. After the flow exits the tip gap it rolls up into a tip leakage vortex. Losses are generated both in the tip gap due to separation and as the tip leakage vortex mixes into the mean flow.

One mechanism of loss production in the tip gap and the tip leakage vortex is the production and dissipation of turbulence. The energy contained in turbulent motion contributes to a decrease in the mean kinetic energy of the fluid. The conversion from mean kinetic energy to turbulence kinetic energy may help to explain the overall losses in a turbomachine.

Studies performed in linear cascades can assist in the understanding of the mechanisms of loss production in the tip gap as well as other regions of the flow. The VPI&SU turbine cascade has been the subject of several experimental and computational studies. These previous studies as well as the current study of the turbulence in the tip leakage vortex can serve to provide a better understanding of the mechanisms of loss production in a blade row with tip leakage.

The work in this thesis included the development of a new rotatable hot wire probe with high spatial resolution to enable accurate mean flowfield and turbulent measurements. A system to digitally sample and analyze the fluctuating hot wire signals as well as a system to traverse the probe in the measurement plane and automatically rotate the probe through several angular settings was also developed.

Turbulence measurements were verified in fully developed pipe flow to check the probe, instrumentation and experimental procedure for consistency. Turbulence measurements were then performed in a linear cascade in the tip leakage vortex in a plane 0.96 axial chord lengths downstream of the blade leading edge.

The results that were obtained in the cascade are the distribution of all six terms of the Reynolds stress tensor, the turbulence kinetic energy distribution and the velocity field. The high turbulence flow generated in the tip gap proceeded along the bottom endwall until it separated from and was convected around the outside of the tip leakage vortex.

Chapter II
Literature Review

II.A. Secondary Flow Mechanisms

Secondary flow can be defined as the difference between the actual flow and the ideal primary flow, usually defined as inviscid, 2-dimensional potential flow. There are three secondary flow mechanisms observed in the VPI&SU tip-leakage turbine cascade:

1.) A passage vortex is formed when the inlet flow contains an initial distribution of normal vorticity, such as the vorticity in an endwall boundary layer, which is converted into a streamwise component of vorticity due to flow curvature. Also contributing to the generation of the passage vortex is the migration of the endwall boundary layer fluid to the suction side of the passage.

2.) A horseshoe vortex is generated by the interaction of the endwall boundary layer with the blade leading edge. When the boundary layer encounters the leading edge of the blade the vortex line is stretched and convected around either side of the blade, creating streamwise vorticity. The pressure side leg of the horseshoe vortex is convected across the passage, while the suction side leg of the vortex wraps around the blade.

3.) In an unshrouded rotor the clearance between the tips of the blade and the annular casing is known as the tip gap. This clearance allows a flow to develop driven by the pressure difference between the pressure and suction sides of the blade. The flow through the tip gap exits the gap as a jet which eventually rolls up into a tip leakage vortex.

II.B. Turbulence in Tip Leakage Flows

In a tip leakage vortex the effects of the turbulence created in the tip gap have a major influence on the losses in this region. Moore, Shaffer and Moore [1] found that in a passage vortex the turbulent stresses contribute to a decrease in mean kinetic energy resulting in larger mixed out losses.

When describing a turbulent flow it is convenient to separate various quantities into mean components and fluctuating or turbulent components. This can be thought of as the superposition of a random fluctuating flow onto a steady flow. The following relations for the three components of instantaneous velocity are an example written in the convention used throughout this thesis:

$$U(t) = U + u; V(t) = V + v; W(t) = W + w$$

where U, V and W represent time averaged properties, for example:

$$U = \frac{1}{t_1}\int_{t_0}^{t_0+t_1} U(t)\, dt$$

By introducing time averaged and fluctuating quantities into the Navier-Stokes equations of motion and time averaging, the following system of equations results for steady, incompressible flow with constant viscosity:

$$\rho\left(U\frac{\partial U}{\partial x}+V\frac{\partial U}{\partial y}+W\frac{\partial U}{\partial z}\right)=-\frac{\partial P}{\partial x}+\mu\nabla^2U-\rho\left(\frac{\partial\overline{u^2}}{\partial x}+\frac{\partial\overline{uv}}{\partial y}+\frac{\partial\overline{uw}}{\partial z}\right)$$

$$\rho\left(U\frac{\partial V}{\partial x}+V\frac{\partial V}{\partial y}+W\frac{\partial V}{\partial z}\right)=-\frac{\partial P}{\partial y}+\mu\nabla^2V-\rho\left(\frac{\partial\overline{uv}}{\partial x}+\frac{\partial\overline{v^2}}{\partial y}+\frac{\partial\overline{vw}}{\partial z}\right)$$

$$\rho\left(U\frac{\partial W}{\partial x}+V\frac{\partial W}{\partial y}+W\frac{\partial W}{\partial z}\right)=-\frac{\partial P}{\partial z}+\mu\nabla^2W-\rho\left(\frac{\partial\overline{uw}}{\partial x}+\frac{\partial\overline{vw}}{\partial y}+\frac{\partial\overline{w^2}}{\partial z}\right)$$

(II1)

where P is the time averaged static pressure. Here the additional or Reynolds stresses appear from the addition of turbulence. The components of the stress tensor due to turbulence can be written:

$$\rho\begin{pmatrix}\overline{u^2} & \overline{uv} & \overline{uw}\\ \overline{uv} & \overline{v^2} & \overline{vw}\\ \overline{uw} & \overline{vw} & \overline{w^2}\end{pmatrix}$$

For convenience the Reynolds stresses referred to in this thesis are the Reynolds stresses as defined above divided by the density, ρ.

By multiplying equations II1 by U, V and W respectively and summing, the following equation for the kinetic energy of the mean motion is obtained. In Cartesian tensor notation:

$$\rho\frac{\partial}{\partial t}\left(\tfrac{1}{2}U_iU_j\right)+\frac{\partial}{\partial x_i}U_i\left(P+\tfrac{1}{2}\rho U_jU_j\right)=$$
$$\rho\,\overline{u_iu_j}\frac{\partial U_i}{\partial x_j}+\frac{\partial}{\partial x_j}\left(-\rho\,\overline{u_iu_j}U_i\right)+ \qquad \text{(II2)}$$
$$\mu\frac{\partial}{\partial x_i}\left[U_j\left(\frac{\partial U_i}{\partial x_j}+\frac{\partial U_j}{\partial x_i}\right)\right]-\mu\left(\frac{\partial U_i}{\partial x_j}+\frac{\partial U_j}{\partial x_i}\right)\frac{\partial U_i}{\partial x_j}$$

The first term appearing on the right hand side of the equation is the turbulence production or work-deformation term. This term explains a decrease in mean kinetic energy as the level of turbulence increases.

Of particular interest in the study of energy transfer and losses in turbulent flow is the turbulence kinetic energy, TKE:

$$TKE=\frac{\overline{q^2}}{2}=\frac{\left(\overline{u^2+v^2+w^2}\right)}{2} \qquad \text{(II3)}$$

where q is the absolute instantaneous fluctuating velocity; and the rms turbulence intensity:

$$T_u=\sqrt{\frac{1}{3}\frac{\overline{q^2}}{U_o^2}} \qquad \text{(II4)}$$

Where U_0 = is the upstream velocity in the freestream.

Introducing the turbulence kinetic energy conservation relation:

$$\rho \frac{D}{Dt}\left(\frac{\overline{q^2}}{2}\right) = -\rho \overline{u_i u_j} \frac{\partial U_j}{\partial x_i} - \frac{\partial}{\partial x_i}\left[u_i\left(p + \frac{\rho q^2}{2}\right)\right] + \mu \frac{\partial}{\partial x_i}\left[u_j\left(\frac{\partial u_i}{\partial x_j} + \frac{\partial u_j}{\partial x_i}\right)\right] - \mu\left(\frac{\partial u_i}{\partial x_j} + \frac{\partial u_j}{\partial x_i}\right)\frac{\partial u_j}{\partial x_i} \quad \text{(II5)}$$

Here the work-deformation term again appears, but with opposite sign. This shows that for an increase in turbulence kinetic energy there is a 1:1 decrease in mean kinetic energy.

II.C. Previous Findings

The previous studies at VPI&SU have involved the use of two cascades. Both cascades were designed to be geometrically similar to that used by Langston et al. [2]. The first cascade used was identical to the present cascade (See section III.A.2) but without a tip gap. This first cascade also had a relatively thick inlet boundary layer, δ = 38 mm (16% of blade span) which allowed the study of large secondary flows.

Of particular interest to this current study is the work of Moore, Shaffer and Moore [1] and Shaffer[3]. They developed a rotatable x-wire hot wire probe to measure turbulence quantities in the wake of the cascade in a cross sectional plane at X/c= 1.1 (See Fig. 1). They found that the conversion of mean kinetic energy into turbulence kinetic energy contributed significantly to the decay of secondary kinetic energy. This mechanism of energy exchange contributed to a loss in total pressure since the turbulence kinetic energy was dissipated downstream of the trailing edge through viscous effects causing an irreversible rise in the internal energy of the fluid. This loss was found to be responsible

irreversible rise in the internal energy of the fluid. This loss was found to be responsible for 21% of the mass averaged total pressure loss. The measured distributions of $\overline{u^2}$, $\overline{v^2}$ *and* $\overline{w^2}$, were distributed non-isotropically with peak values of $\overline{u^2}$ being lower than peak values of $\overline{v^2}$ *and* $\overline{w^2}$.

The current cascade used in VPI&SU studies includes a tip gap of 2.1% of the blade span and a thinner inlet boundary layer, δ = 2.2 mm (0.9% blade span), allowing tip leakage effects to dominate over other secondary flow effects.

Moore and Tilton [4] used static pressure tappings along the bottom endwall and under the tip of the blade to study the flow in the tip gap region. They concluded that the flow involved:

1.) Separation of the flow at the inlet to the tip gap

2.) The development of a vena contracta downstream of the inlet

3.) Mixing of the flow after the vena contracta to the exit of the tip gap.

Figure 2 gives an illustration of this model.

Dishart and Moore [5] used a pressure probe to measure the flow at the tip gap exit plane at several chordwise positions. Their results are consistent with the model of Tilton. They also determined that 5.7% of the flow passed through the tip gap and that the losses at the exit amounted to 10.9% of the inlet passage kinetic energy.

A convenient parameter for the evaluation of losses in turbomachinery is the total pressure loss coefficient:

$$C_{P_t} = \frac{p_{to} - p_t}{\frac{1}{2}\rho U_0^2} \qquad \text{(II6)}$$

where, p_{to} = Upstream total pressure

p_t = Local total pressure

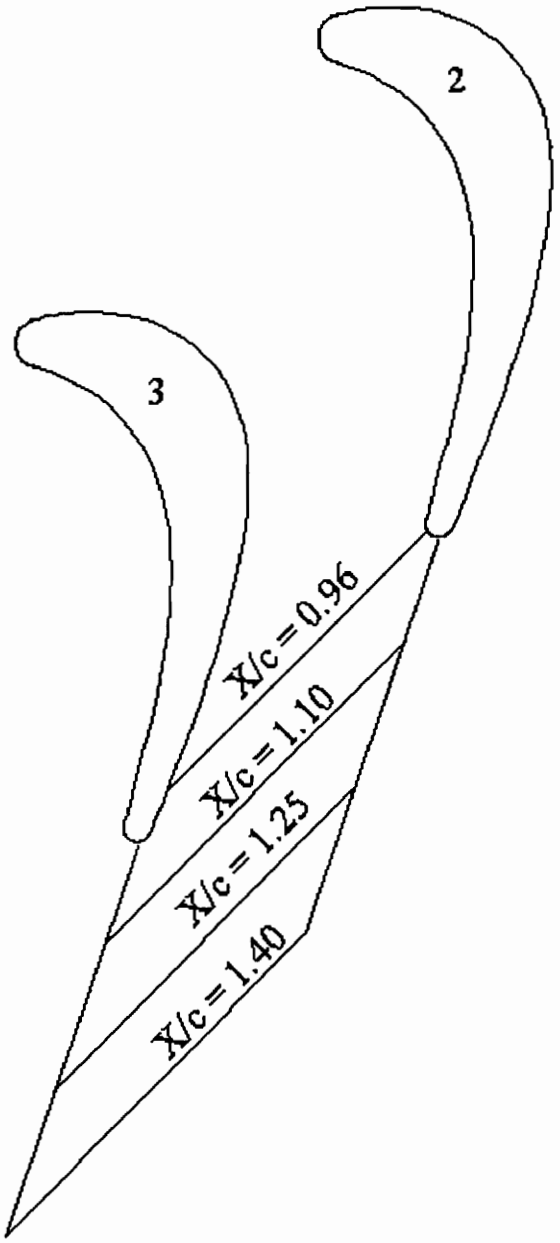

Figure 1. Location of Measurement Planes

Dishart and Moore also studied the loss distribution at a measurement plane of X/c = 1.4. They found that the additional losses due to tip leakage had a 1:1 correspondence to the sum of the loss generated within the tip gap and the dissipation of the kinetic energy exiting the tip gap normal to the blade. The measured secondary velocity vectors at X/c = 1.4 are shown in Fig. 3 and the measured total pressure loss coefficient at X/c = 1.4 in Fig. 4.

Peters [6] conducted an extensive survey of the losses at a measurement plane of X/c =0.96. A vector plot of the secondary velocities projected into a cross sectional plane normal to the primary flow direction is shown in Fig. 5. In the lower half of the measurement plane the flow is dominated by the tip leakage vortex with a small remnant of the passage vortex generated from the inlet boundary layer. The maximum secondary velocity was 1.7 U_0 in the tip leakage vortex compared to 0.55 U_0 measured by Dishart also in the tip leakage vortex . This is evidence of the dissipation of the strength of the tip leakage vortex downstream of the trailing edge.

A plot of the contours of total pressure loss coefficient at X/c = 0.96 is given in Fig. 6. A maximum total pressure loss coefficient of 3.0 was measured in the tip leakage vortex core. A low pressure core was also found in the tip leakage vortex core, having a static pressure coefficient , C_{ps} , of -3.34 where:

$$C_{Ps} = \frac{p_s - p_{s,o}}{\frac{1}{2}\rho U_0^2} \qquad \text{(II7)}$$

where, $p_{s,o}$ = Upstream static pressure

p_s = Local static pressure

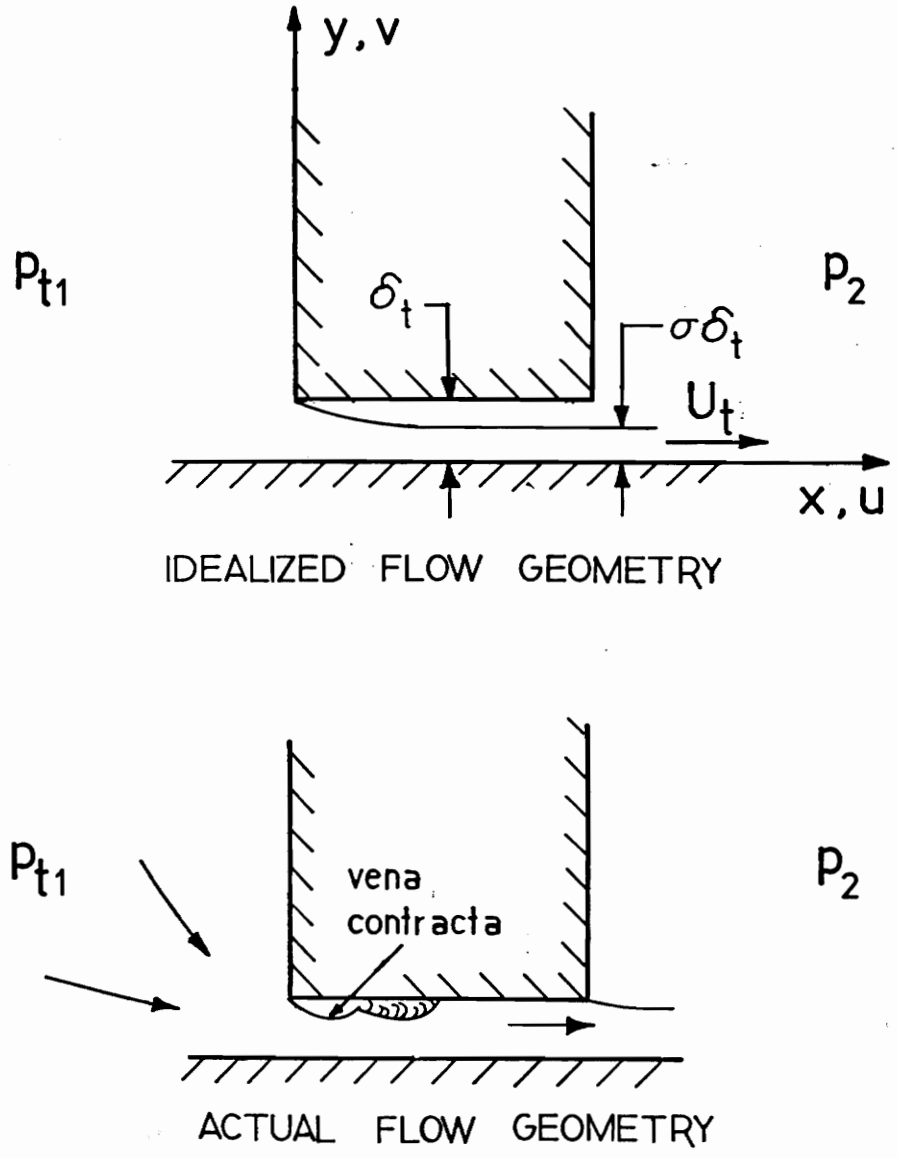

Figure 2. Tip Gap Flow Model

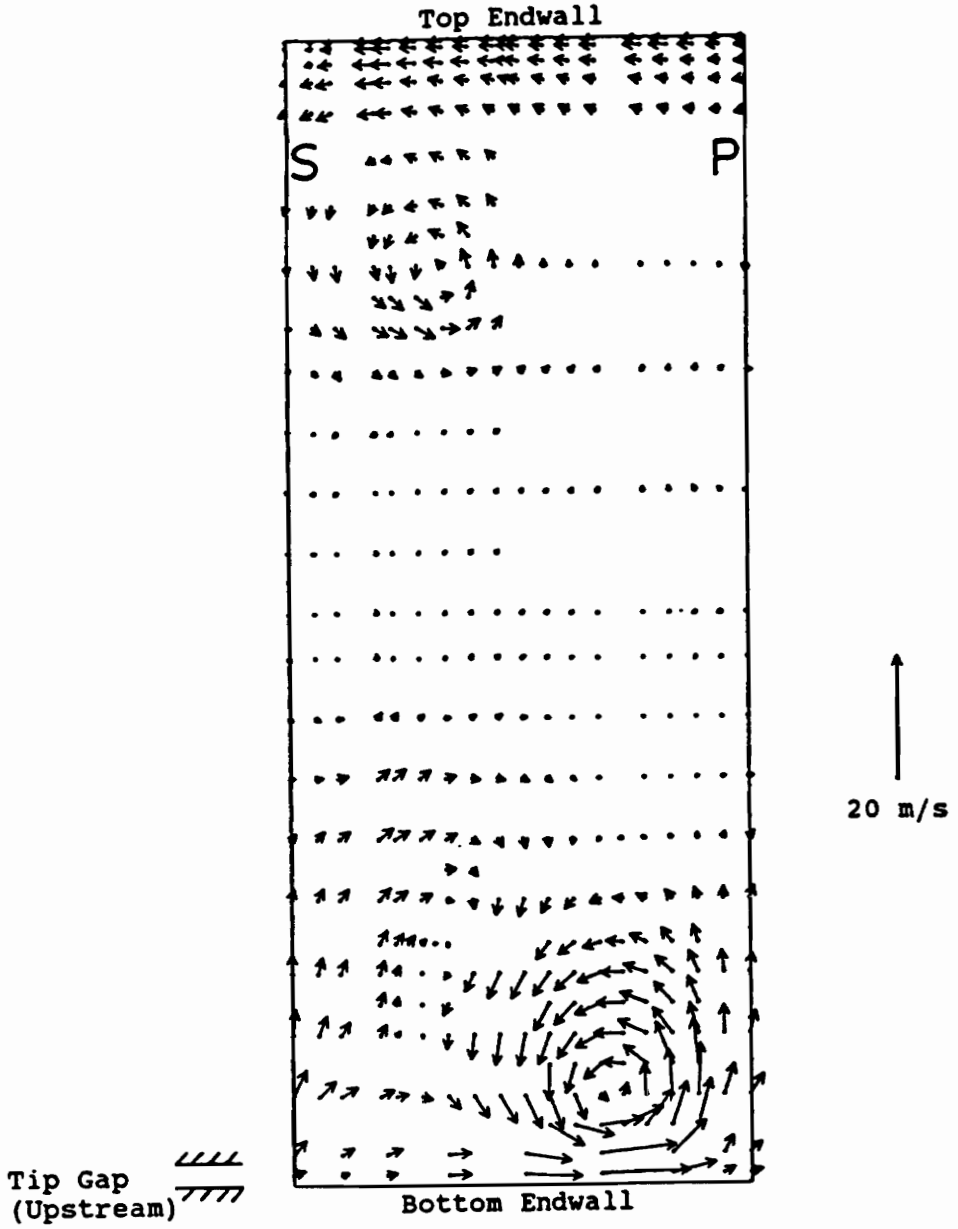

Figure 3. Secondary Velocity Vectors in the Cross Sectional Plane at X/c = 1.4

After Dishart [5]

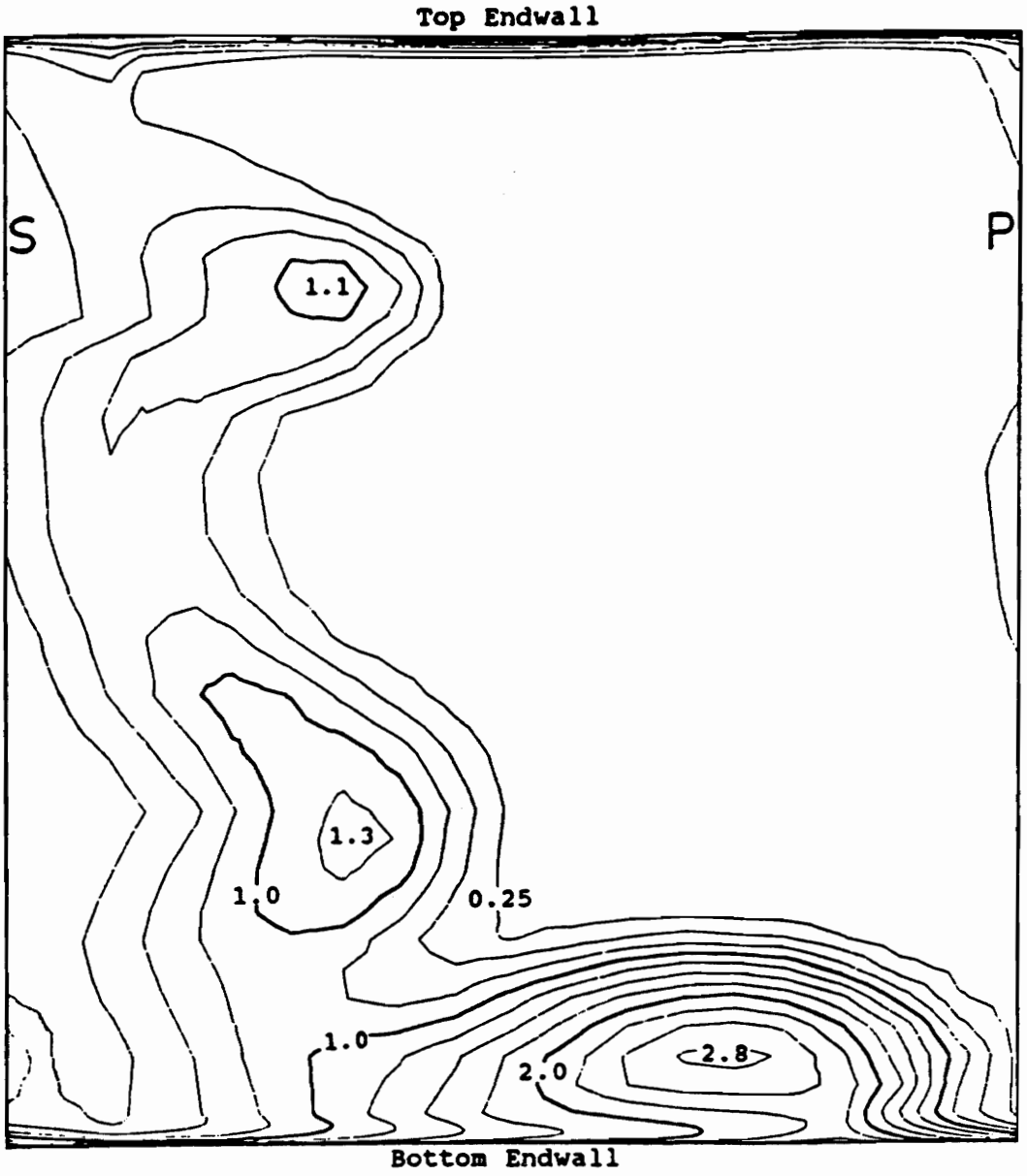

Figure 4. Contours of Total Pressure Loss Coefficient at X/c = 1.4

After Dishart [5]

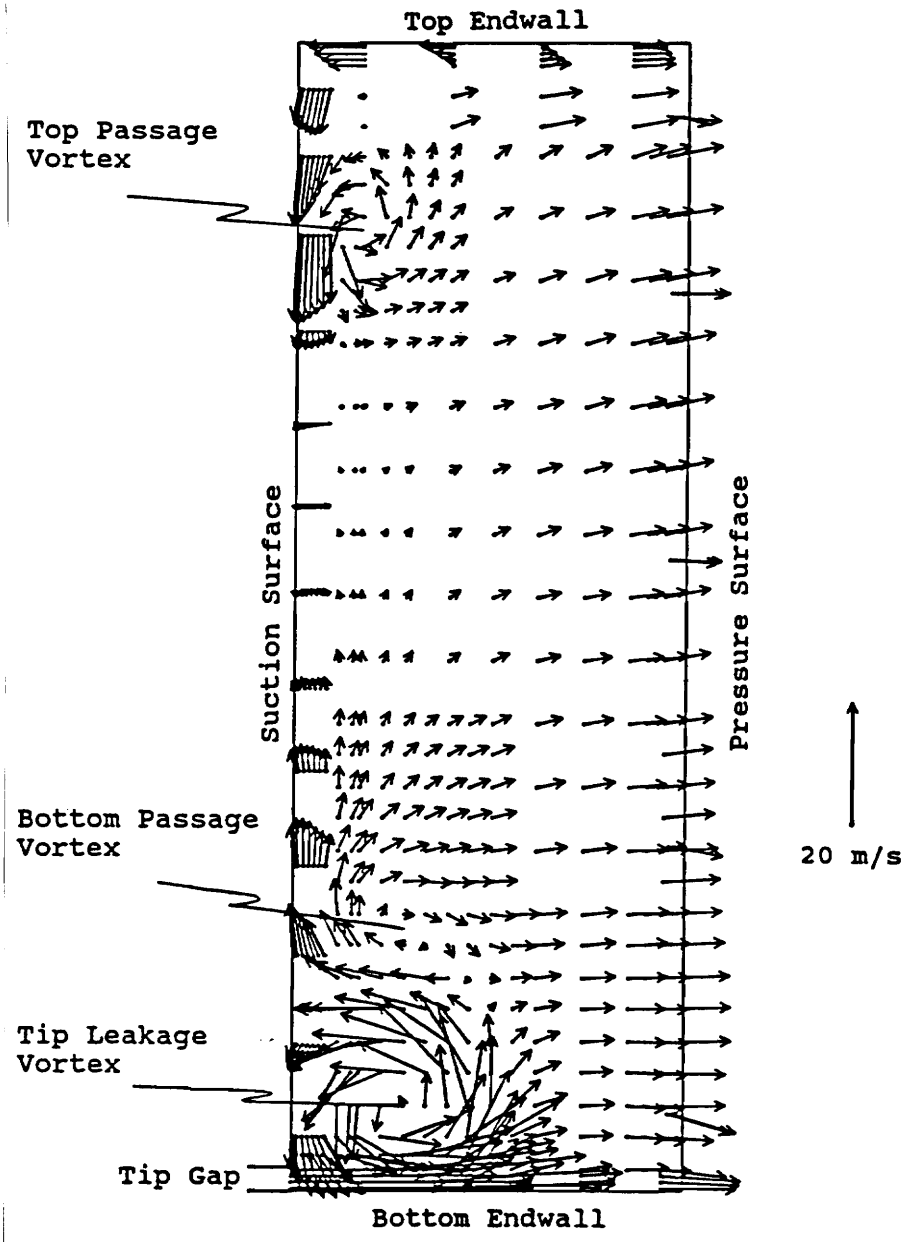

Figure 5. Secondary Velocity Vectors in the Cross Sectional Plane at X/c = 0.96

After Peters [6]

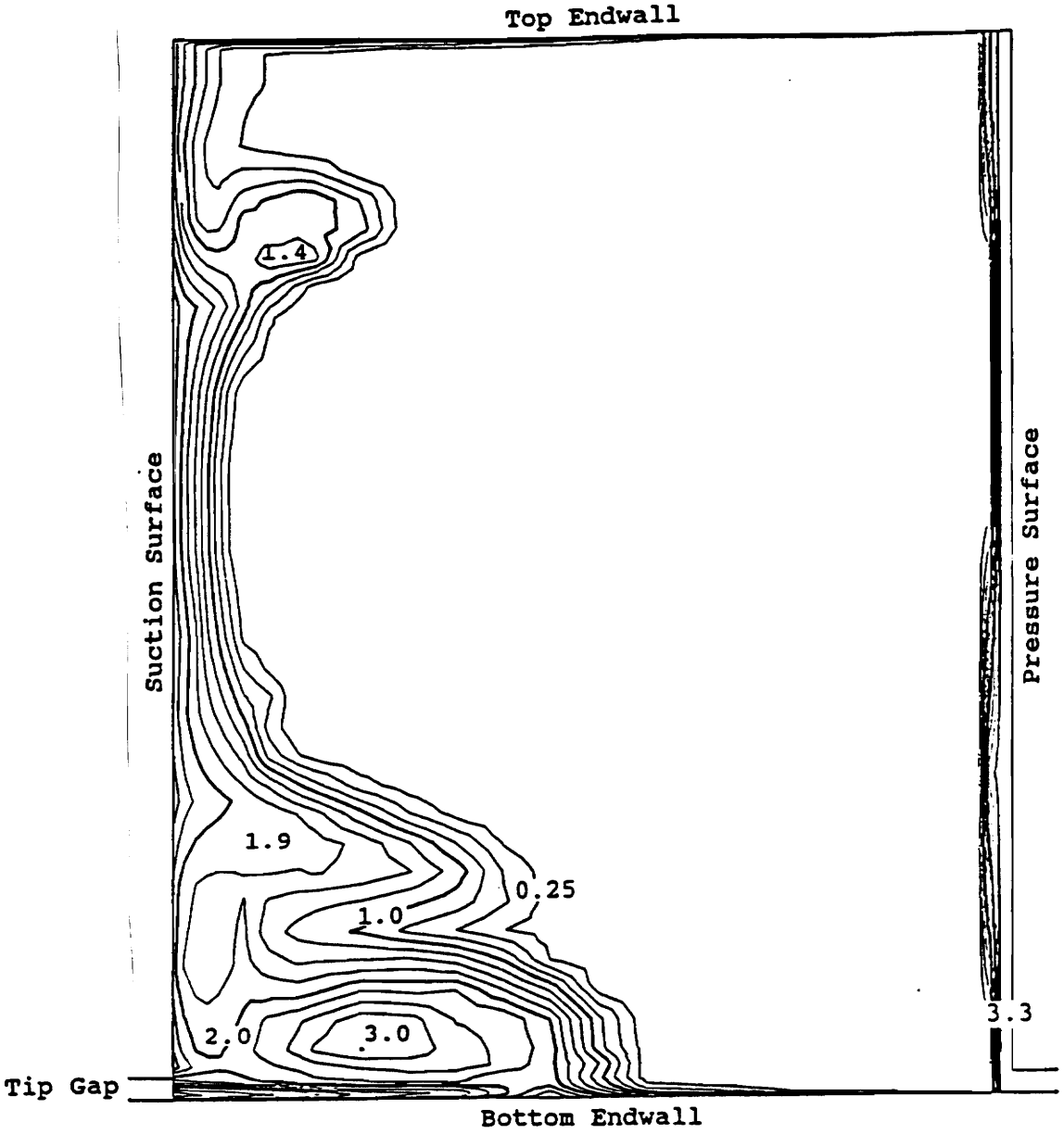

Figure 6. Contours of Total Pressure Loss Coefficient at X/c = 0.96

After Peters [6]

II.D. Hot Wire Technique

Hot wire anemometry is probably the most accurate method of measuring the turbulence quantities in a highly three-dimensional turbulent vortex. The technique used in the present investigation is the same as the one used by Shaffer[3].

Shaffer considered several alternative hot wire configurations. A single slantwire can measure all six components of the Reynolds stress tensor by rotating the probe through a minimum of six angular settings. At each angular setting, an equation relating the mean and fluctuating voltages to the six stresses is produced. This method was rejected by Shaffer due to the inability of several researchers to produce reliable results. The second method considered was the use of stationary x-array hot wire probes. A stationary x-wire probe placed into the flow with its sensors in a plane can determine two components of the normal stress and one shear stress component associated with that plane. A second probe must be used to determine the other component of the normal stress and one additional component of shear stress. The method produces errors when the flow has any component normal to the plane and so it is impractical in this study due to the inherent three dimensionality of the flow. Another problem is that the third component of shear stress cannot be determined with this method. The final method considered was the use of a three wire probe. Three orthogonal wires can be used to determine all six Reynolds stress components in a single measurement. Practical problems such as probe fabrication and cost as well as the cost and complexity of an extra channel of hot wire and data acquisition equipment make the three wire system less attractive. A complete justification for the use of the rotatable x-wire endflow probe rather than single slant wire, traditional x-array or triple wire systems is discussed by Shaffer. Other

accounts of the use of a rotatable x-wire probe as such are not known to exist at the present time.

A review of the basic technique used in this study follows. The analysis method is adopted from the method used by Gorton and Lakshminarayana [7] for a three wire probe and is detailed in Appendix D.

Consider an x-wire probe with two wires A and B. For wire A the instantaneous voltage (E+e) is related to the instantaneous absolute velocity (Q+q) by a response equation:

$$E_A^a = Q_0\left(\cos^2\Phi + k^2\sin^2\Phi\right) \tag{II8}$$

where a and k are calibration constants which can be determined experimentally, Q_0 is a reference absolute velocity and Φ is the angle between the wire normal and the absolute velocity vector. Expanding both sides and time averaging yields an equation relating the mean square of the fluctuating part of the wire voltage, $\overline{e_A^2}$, to a corresponding mean square of the fluctuating absolute velocity, $\overline{q_A^2}$. Relating the cooling velocity to the probe co-ordinate system, linearizing and time averaging then yields:

$$\overline{q_A^2} = A_1\overline{u^2} + A_2\overline{v^2} + A_3\overline{w^2} + A_4\overline{uv} + A_5\overline{uw} + A_6\overline{vw} \tag{II9}$$

where $A_1,\ldots,A_6$ are known functions of the mean velocities U, V and W. Using the rotatable x-wire probe, wire B is introduced and two more equations are created in a similar fashion for the mean square of the fluctuating voltage, $\overline{e_B^2}$ and the mean product of the fluctuating voltage from A and B, $\overline{e_A e_B}$. The mean product can be obtained directly through the use of digital sampling.

The resulting system of three equations and six unknowns can be solved by rotating the probe to an independent position where three more equations can be obtained, thus providing as many equations as unknowns.

Since it was desired in this current project to measure the turbulence quantities in a tip leakage flow which is of a smaller scale than the passage vortex studied by Shaffer, a probe with greater spatial resolution than the previously used probe was designed and fabricated. There are many subtleties in the design and manufacture of a new hot wire probe which needed to be considered at each step of this process. Lakshminarayana [8] lists the following sources in measurement error to be avoided for three-wire hot-wire probes which are equally valid for the rotatable x-wire probe:

1.) inclination of the wire to the flow (deviation from the cosine law);

2.) geometry of prongs and probe body;

3.) finite distances between wires;

4.) finite dimensions of individual wires;

5.) temporal resolution or thermal inertia of individual wires;

6.) aging, oxidation and contamination of the wires;

7.) ambient temperature drift;

8.) proximity of wire to the wall;

9.) probe body vibration due to rotation and flow induced excitation;

10.) spurious signals from the power line (60 Hz) and blade passing frequency;

11.) finite sampling time;

12.) measurements of wire angles with respect to the reference coordinate system;

13.) mis-alignment of the probe with respect to the reference axis.

Lakshminarayana suggests that 1,7 and 8 can be eliminated by using correction factors or temperature compensated anemometer systems and by calibrating for pitch and

yaw angle as well as wall vicinity effects. 2-5 can be eliminated by selecting proper probe, wire and support dimensions and by eliminating prong interference. 6 can be eliminated by using a low overheat ratio and cleaning the wire often. A suggested value of the ratio of wire length-diameter ratio is $\ell/d = 300$. 9, 10, 12 and 13 can be reduced by obvious means such as proper clamping, accurate wire and probe angle measurements and proper electrical grounding. Error source 11 is an inherent error that can only be reduced by increasing the sampling period for unsteady flows.

Another factor applicable to a rotatable endflow probe is the concentricity of the rotating probe about its axis. This can be overcome by ensuring that the probe holder is straight and the mounting of the holder is adequate.

II.E. Objectives of the Present Study

The results of the previous investigators yield several important questions which the present study will attempt to answer:

1.) What is the structure of the turbulence in the tip leakage vortex region?

2.) How high is the level of turbulence as the flow exits the tip gap?

3.) What are the mechanisms of dissipation of the mean kinetic energy?

4.) Of the losses measured by Peters at X/c = 0.96, how much of the loss is present as turbulence kinetic energy?

5.) Based on the observation of a low static pressure tip leakage vortex core, is there any apparently unusual turbulence structure contributing to this low static pressure?

Chapter III
Apparatus

III.A. Wind Tunnel and Cascade

III.A.1. Wind Tunnel

Measurements for this study were taken in a 20 KW open cycle wind tunnel shown in Figure 7. Upon exit from the blower the flow passes first through a diffuser and then through a plenum chamber containing honeycomb flow straighteners, screens and filters. The flow is then contracted in a diffuser to 0.91 m width and 0.3 m height. Immediately upstream from the cascade test section the endwall boundary layers are bled off in order to prevent thick boundary layers from producing secondary flows in the blade passages which could obscure the tip leakage effects. A 0.51 mm diameter trip wire was placed at the leading edges of the boundary layer bleeds in order to insure a turbulent endwall boundary layer is started.

III.A.2. VPI&SU Cascade

The VPI&SU cascade contains five large scale blades which were designed to be geometrically similar to those in cascade used by Langston. Figure 8 shows the blade row and the two adjustable end bleeds. The blades are in the shape of a reaction turbine

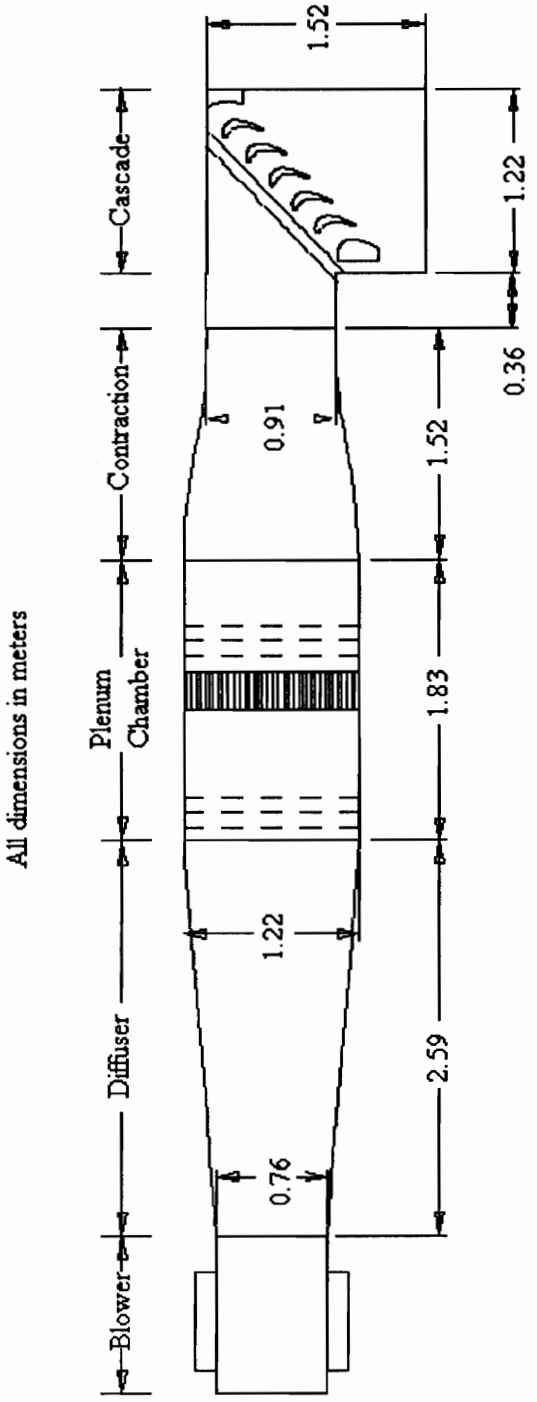

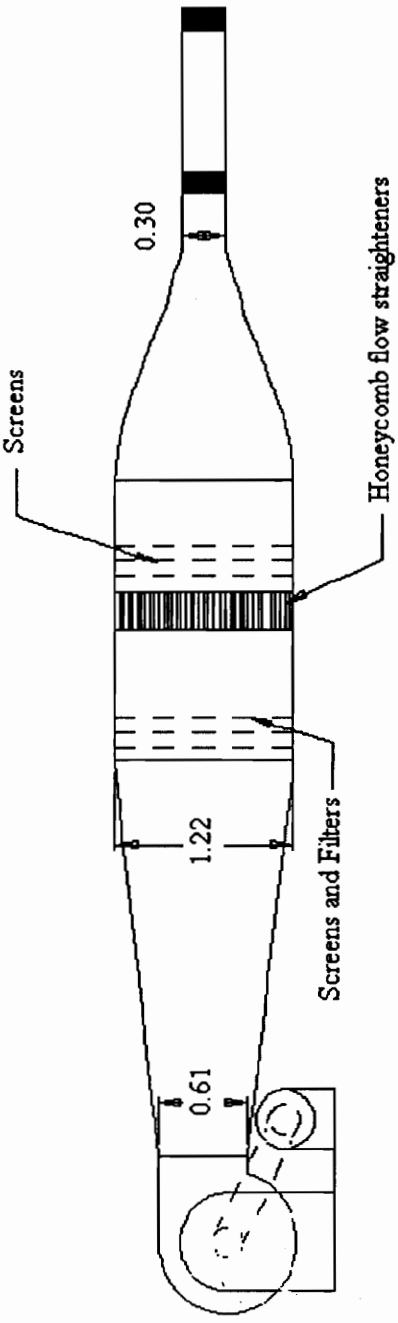

Figure 7. Wind Tunnel

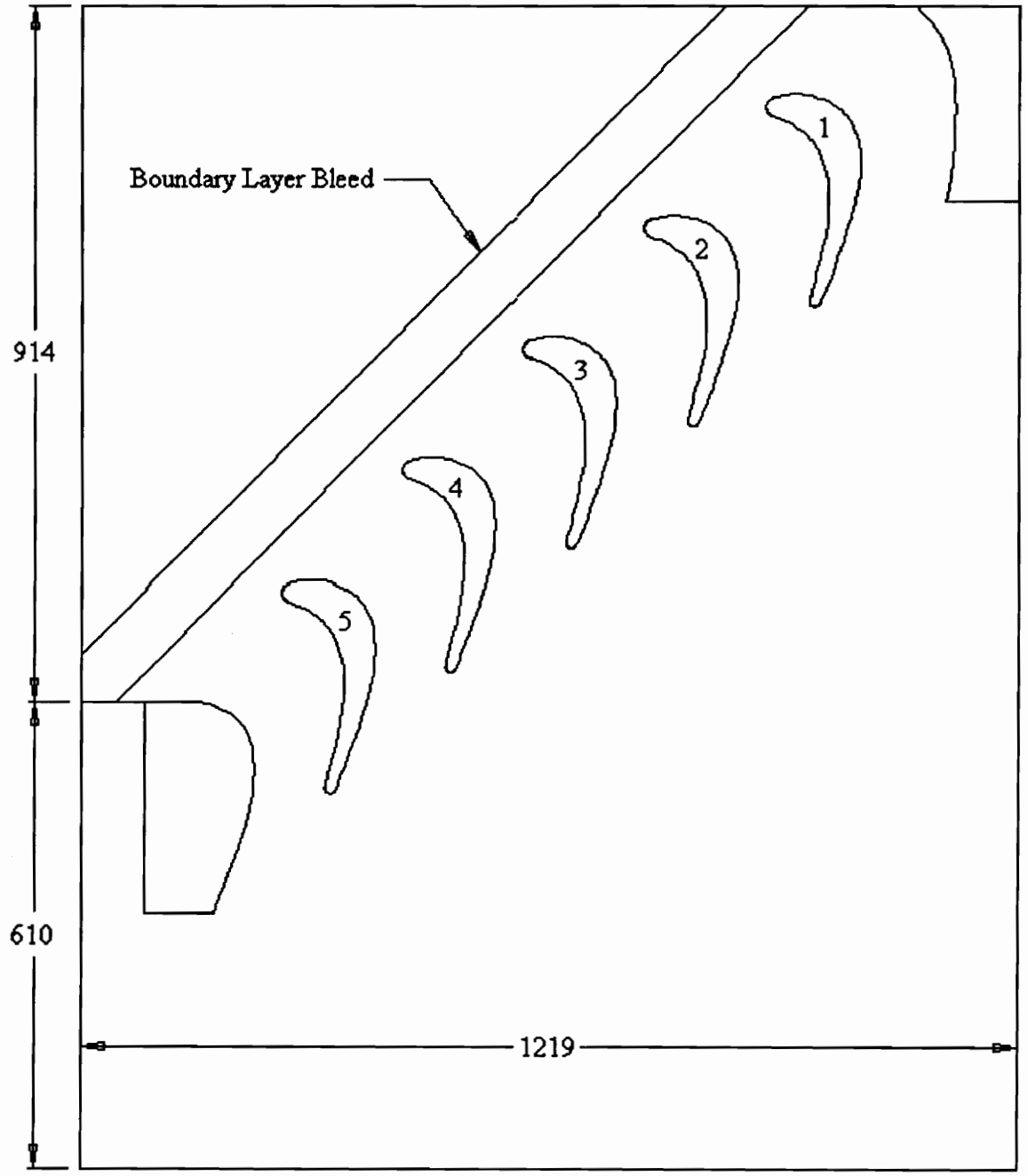

Figure 8. VPI&SU Turbine Cascade

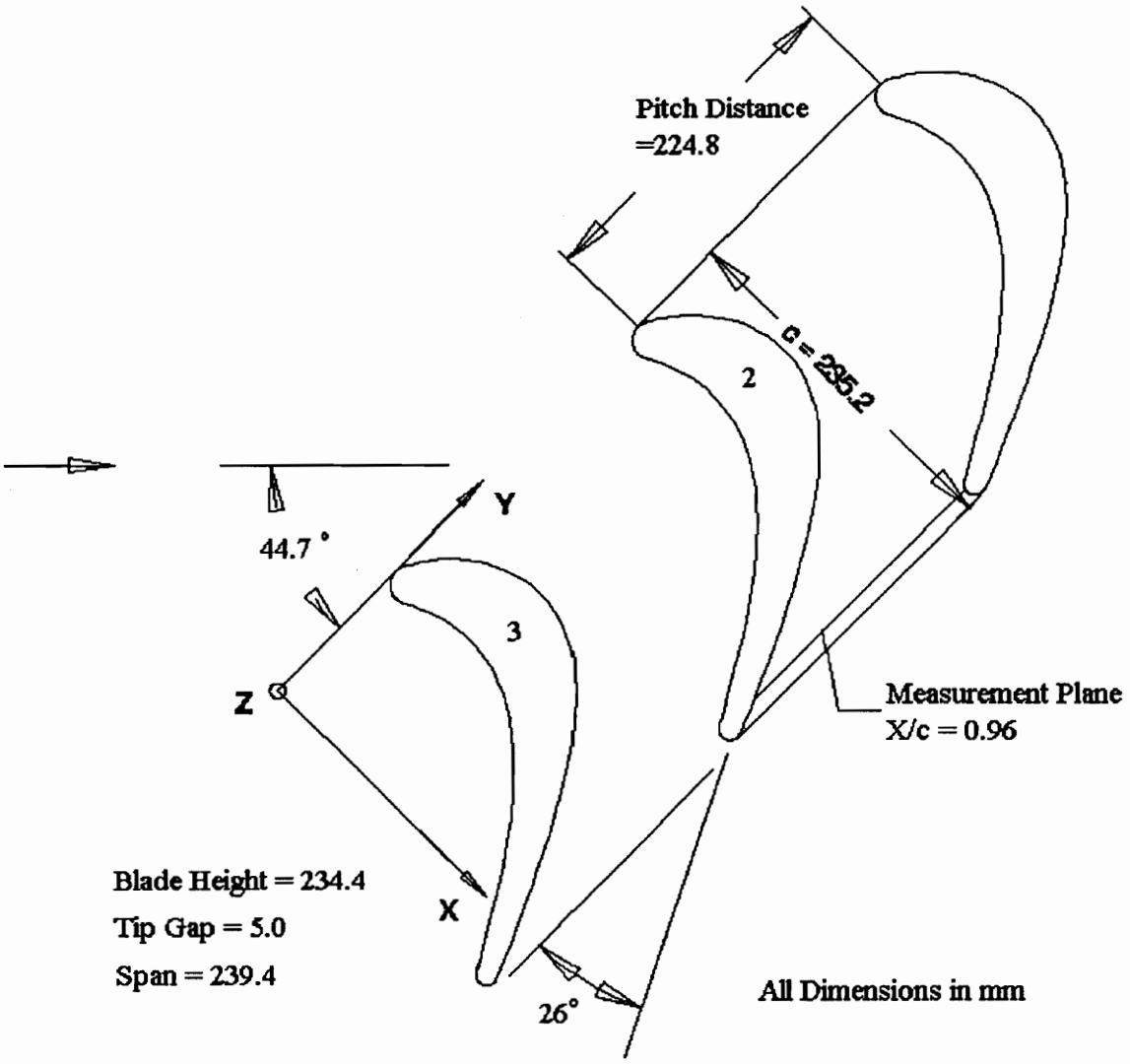

Figure 9. Cascade Blade Row Details

which turns the flow through an angle of 110° and produces a velocity ratio of 1.6. The Reynolds number based on the axial chord and an exit velocity of 32.8 m/s is approximately 4.5 x 10^5. Trip wires with a diameter of 0.51 mm are located near the leading edge of each blade in order to trip the profile boundary layers. The five blades are cantilevered from the top endwall, with a nominal tip gap of 5 mm which is 2.1% of the blade span, giving a passage height of 239.4 mm. The tip gap varied slightly in the blade row, but was never allowed to vary by more than ± 0.1% of the blade span. The tip gap was measured daily to ensure uniformity.

Figure 9 shows the three center blades along with dimensions. The cascade coordinate system used to identify location is shown with the directions (X, Y, Z) corresponding to the axial, pitchwise and spanwise directions respectively. The measuring planes used in this and previous studies are also shown as well as their locations downstream of the leading edge in distance over axial chord, X/c.

For turbulence measurements at X/c = 0.96 a probe coordinate system was used. The probe coordinate system is shown in figure 10. The direction of the primary flow (U+u) is defined as being in the direction of the camberline at the blade trailing edge. This is at an angle of 26° to the pitchwise direction. The velocity component (W+w) is defined in the spanwise direction. The lateral velocity component, (V+v), is then orthogonal to the (U+u) and (W+w) components.

The secondary flow, or cone angle, is defined as the angle between the total flow vector and the primary flow (U) vector:

$$\Phi_{cone} = \tan^{-1}\left(\frac{\sqrt{V^2 + W^2}}{U}\right). \qquad \text{(III1)}$$

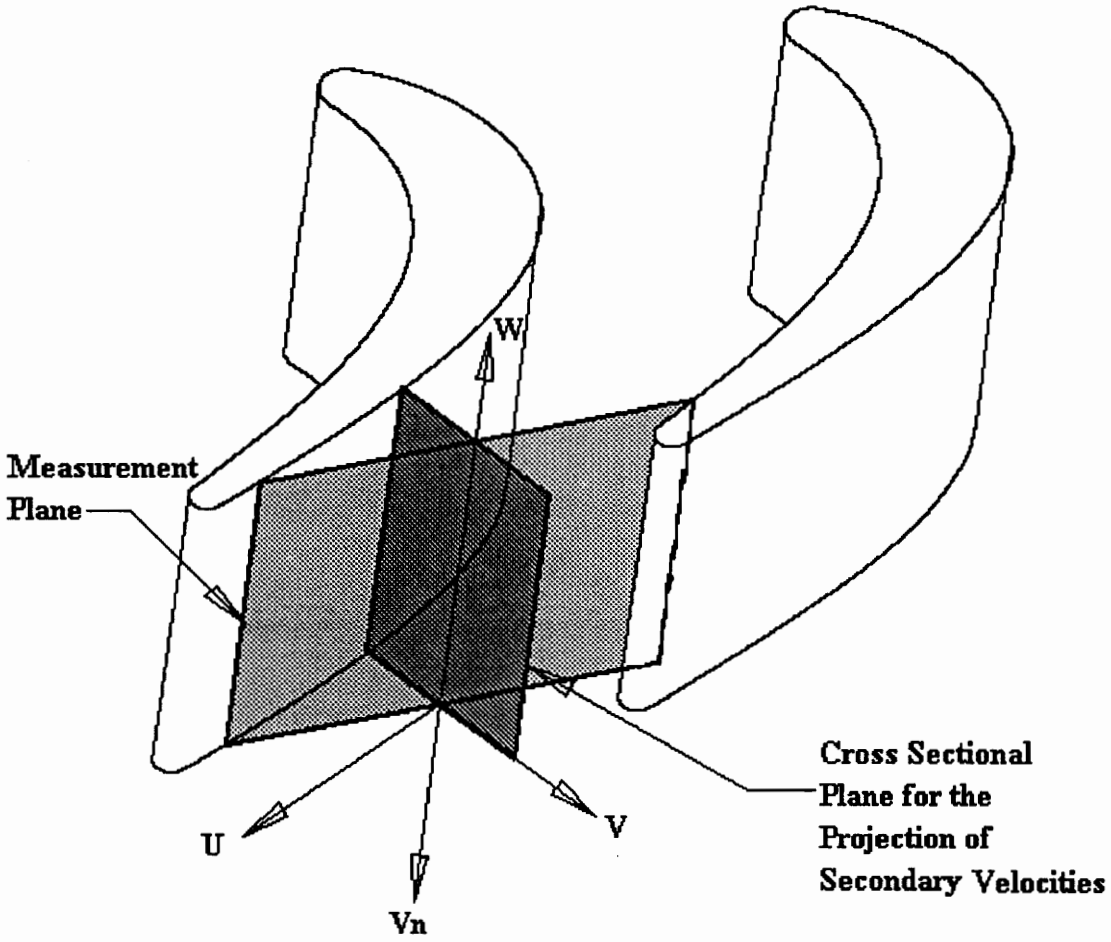

Figure 10. Probe Coordinate System and Location

of Plane for Projection of Secondary Velocities

In practical terms the cone angle is the angle between the total velocity vector and the hot wire probe axis since the probe was oriented in the primary flow direction (x in Fig. 11).

The secondary velocities were projected onto the cross sectional plane shown in Figures 10 and 11.

Table 1. VPI&SU Cascade Geometry

Blade Geometry	
Axial Chord	235.2 mm
Span	234.4 mm
Pitch	224.8 mm
Aspect Ratio	0.997
Airfoil Mean Camber Line Angles	
β_1	43.99°
β_2	25.98°
Inlet Flow	
Inlet flow angle β_1	44.7°
Inlet Velocity	20.5 m/s
Tip Gap	
Tip Gap	5 mm

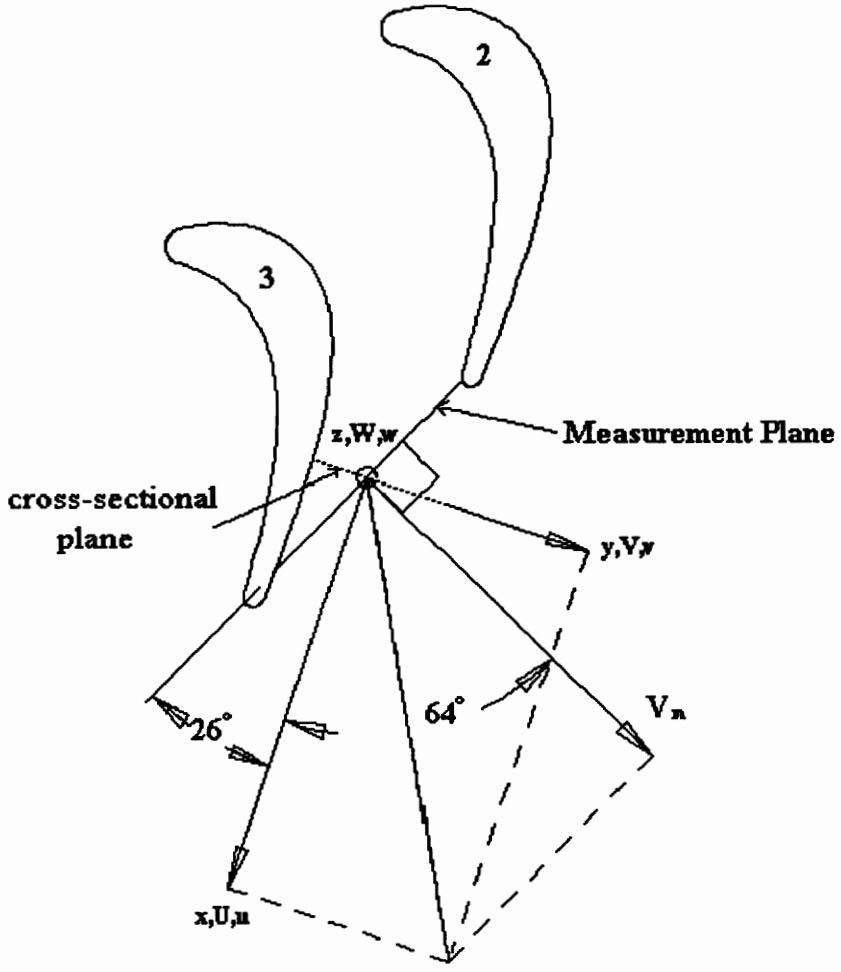

Figure 11. Velocity Components Relative to Measuring Plane and Flow Coordinates

The blade surfaces were made with 3.2 mm (1/8 in.) plexiglas . The leading edge was constructed from 25.4 mm (1.0 in.) diameter plexiglas tubing and the trailing edge from a 14.3 mm (9/16 in.) diameter aluminum rod.

The endwalls of the cascade test section were constructed with 19.1 mm (3/4 in.) plywood. Formica was bonded to the plywood on the inner surfaces to provide a smooth surface in order to minimize flow disturbances. A 230 x 15 mm slot was cut into the top endwall in order to insert the rotatable hot-wire probe mechanism. Other slots used in previous testing were covered with tape to reduce leakage.

III.B.) Calibration Pipe

III.B.1.) Calibration Pipe

A calibration pipe was used as a standard for hot wire calibration and was also used to measure turbulence quantities in fully developed turbulent flow. Figure 12 shows the calibration pipe details.

A centrifugal blower was used to supply air flow to the pipe. Immediately downstream from the blower, the flow was contracted from the blower exit diameter of 130.0 mm to the pipe inside diameter of 80.0 mm. A butterfly valve was used to control the pipe exit dynamic head from a maximum of 50.8 mm (2.0 in.) H_20 to a minimum of 12.5 mm (0.5 in.) H_20. Screens and filters were placed in the flow immediately downstream of the butterfly valve. A honeycomb flow straightener and screen were located 610 mm downstream of the butterfly valve. Following the flow straightener was an uninterrupted length of pipe 19.5 m (240 diameters) in length to the pipe exit.

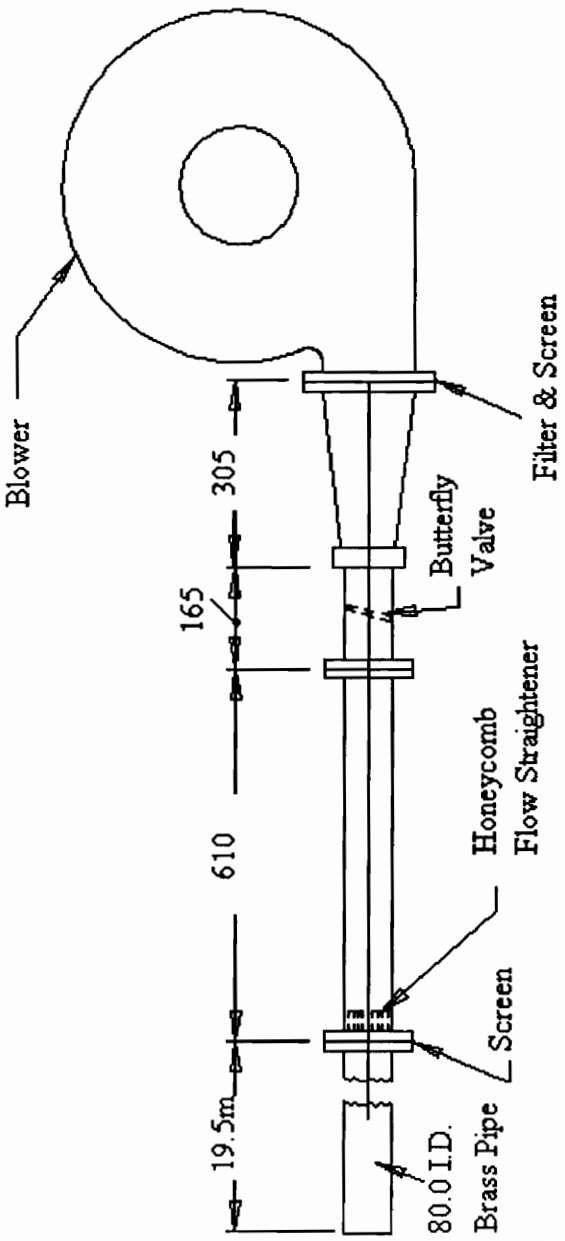

Figure 12. Calibration Pipe Details

The length to diameter ratio of 240 for the uninterrupted section of pipe downstream of the straightener assures fully developed turbulent flow. At the maximum dynamic head of 50.8 mm H_20, the exit velocity was 30.0 m/s. Using a 1/7 power law velocity profile, the average velocity is 82% of the maximum velocity or 24.6 m/s. The Reynolds number based on the maximum average velocity and the pipe inside diameter is then approximately 120,000, which is clearly in the turbulent flow regime.

Static pressure tappings were located 5.9 m upstream of the exit as well as near the pipe exit in order to measure the pressure gradient along the pipe.

III.B.2.) Probe Support Platform

A platform near the exit of the pipe supported the hot wire probe during calibration and fully developed pipe flow testing. Figure 13 shows details of the platform and probe support. The probe could be manually rotated about its axis by turning the dial located at the rear of the holder. The angular position could be measured to within 0.1° with the graduated scale on the dial. The probe yaw angle could be adjusted by swinging the entire holder about an anchor bolt located on the platform directly below the pipe exit centerline. Additionally the probe could be located at points in the flow that were not on the centerline by anchoring the holder at one of four holes off of the probe's vertical centerline. A scale was drawn on the support platform to measure the probe yaw angle.

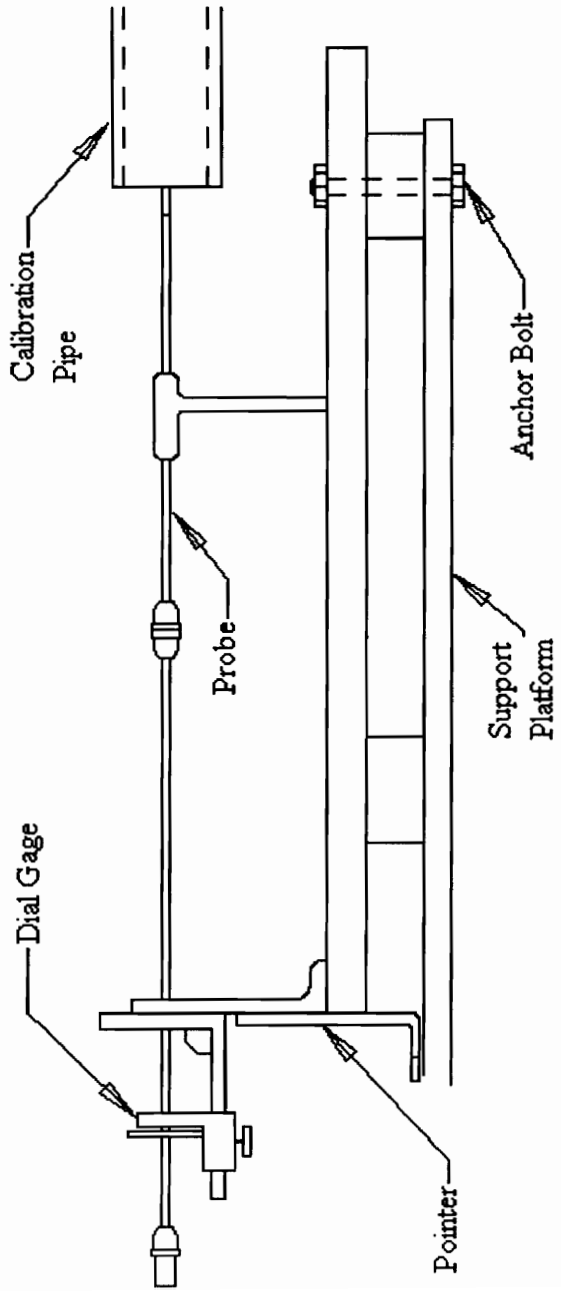

Figure 13. Probe Support Details

III.C. Hot Wire Probes

III.C.1. Rotatable X-Wire Probe

A rotatable x-wire end flow hot wire probe was designed and used for measurements at X/c =0.96. The probe was constructed by modifying a Thermo Systems Incorporated (TSI) model 1240C-20 hot film probe. The films were first removed and the prongs were bent to give geometric characteristics similar to the probe used in previous experimentation. The current probe is smaller than that used by Shaffer in order to improve the spatial resolution. This probe was plugged into a modified TSI 1155 probe support which was held by the probe yoke in cascade testing.

The basic elements of the probe can be seen in Figure 14, including:

1.) Four gold plated prongs of length 12.0 mm (0.47 in.) for the two long prongs and 9.0 mm (0.35 in.) for the two short prongs. These prongs had a base diameter of 1.4 mm (0.055 in.) tapering down to a tip diameter of 0.6 mm (0.024 in.). The prongs were tinned with solder prior to the application of wires. The wires are angularly spaced by 120° about the axis of the probe.

2.) Two hot wire sensors made from elemental tungsten wire of 0.0076 mm (0.0003 in.) diameter. These wires were copper electroplated to allow soldering of the tungsten wire to the support prongs and to control the effective length of exposed wire and thus the wire resistance. The overall wire length was 3.3 mm and the exposed length was 2.3 mm resulting in an ℓ/d ratio of about 300 which is consistent with the recommendations of Lakshminarayana (see section II.D.).

3.) Four gold plated prongs at the end opposite the sensors which plug into the probe support. Since the probe was removable two separate probe supports could be used for cascade testing and for probe calibration in the pipe. The probe could also be stored between tests in order to protect it.

An end view of the probe can be seen in Fig. 15. Long and short prongs are designated by L and S respectively and the corresponding wire A or B is also given. The prongs were spaced 120° apart about the probe axis. Figure 16 is a side view of the probe showing only two prongs in the same plane. The nominal wire angle, α_0 ,was 35.3°.

This probe can measure all six components of the Reynolds stress tensor by rotating it through a minimum of three angular settings spaced 120° apart. At each angular position the wires form two out of three axes in an orthogonal coordinate set. By rotating through three positions, the normal fluctuating velocity in each coordinate direction is measured twice and the product of fluctuations is measured once in each direction. More than three settings can be used to take redundant data for least squares fitting.

The design procedure for this probe consisted of a great deal of trial and error. It was desired to produce a wire resistance of approximately 5Ω in order to provide a power level that did not cause rapid wire burnout. The probe used by Shaffer utilized elemental tungsten wires of 0.0038 mm (0.00015 in.) diameter. During the design of the current probe, similar wires were put on the probe, however the resistance of these wires was not controllable. The wires were also very difficult to work with due to their small size. The final probe design used in the cascade experimentation used elemental tungsten wires with a 0.0076 mm (0.0003 in.) diameter. With this wire soldering the wires to the prongs was much easier and the resistance was readily controlled.

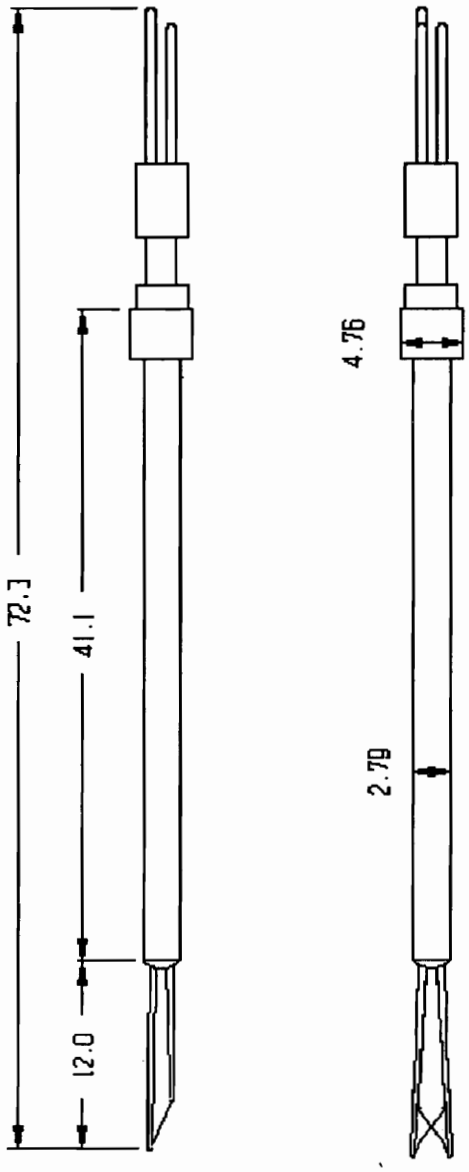

Figure 14. Rotatable X-wire Probe

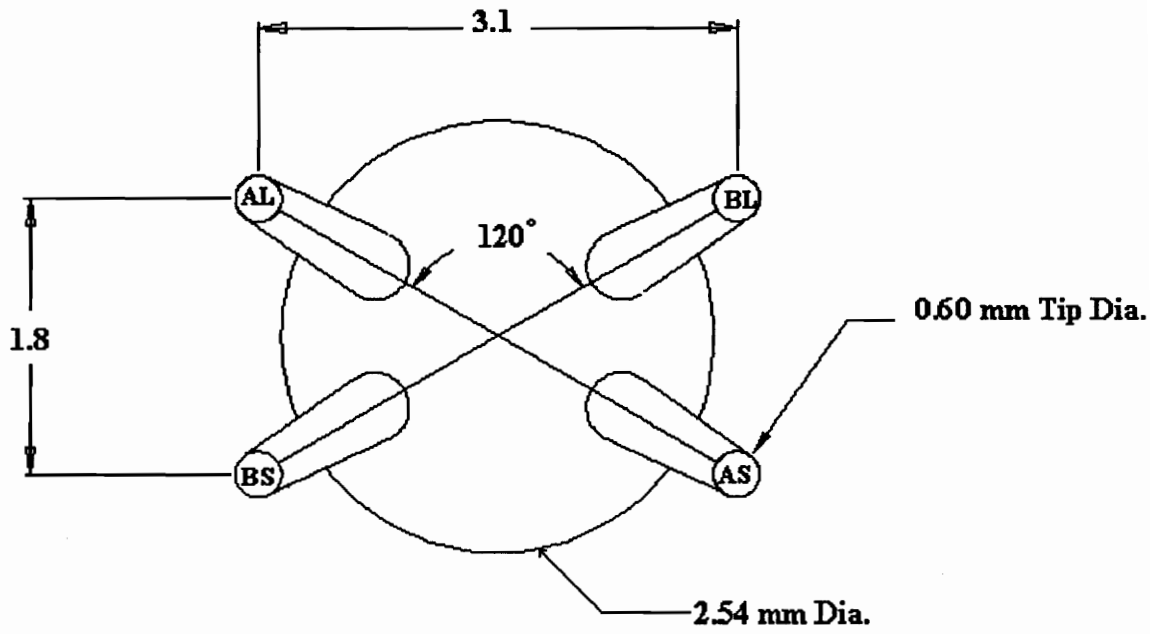

Figure 15. End View of Rotatable X-Wire Probe

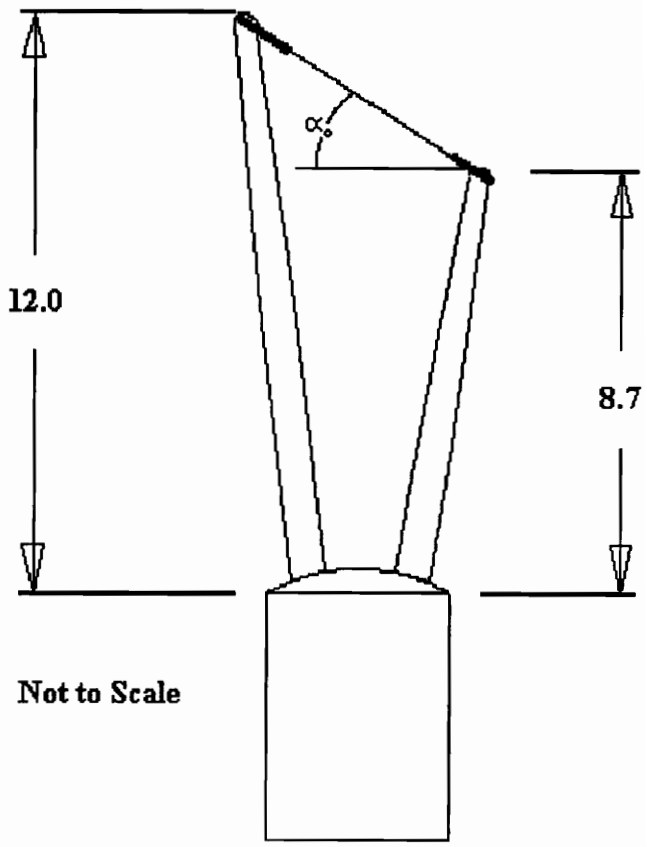

Figure 16. X-Wire Probe Tip With Prongs in Plane

III.C.2. Single Wire Endwall Probe

A single wire probe was used to measure the velocity and normal stress in a direction perpendicular to the blade surface at X/c = 0.96. This probe was used at three positions including a position at the exit of the tip gap. The probe (shown in Figure 17) was inserted through one of several holes drilled through the bottom endwall. A small traverse mechanism allowing steps of 0.0254 mm (1/1000 in.) was mounted underneath the cascade test section. The probe was constructed from 6 mm tubing, the two prongs were made from steel rod with a base diameter of 1.02 mm tapered to a point. The space between the prongs and the length of the elemental tungsten wire is 3.4 mm. This wire was coated with copper and soldered to the prongs the same way as the x-wires were.

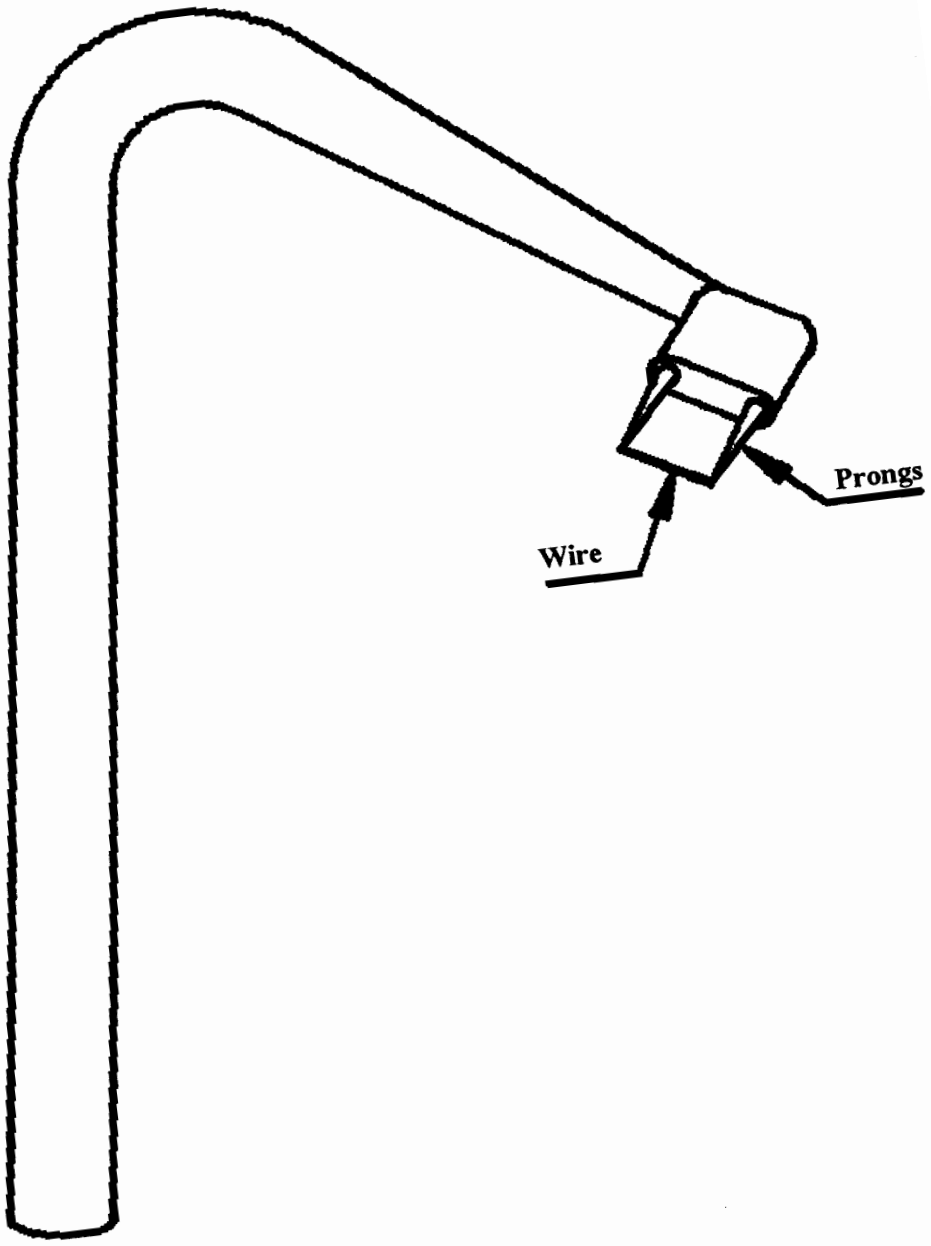

Figure 17. Single Wire Endwall Probe

III.D. Data Acquisition and Probe Motion Control

In all phases of experimentation, the test procedure was designed to be as automated as possible. This was done to eliminate human error, to speed up the entire experimentation process and to enable large amounts of data to be taken. The control system consisted of two major sub-systems, probe movement control and data acquisition. The probe movement control system was used to position and rotate the probe while the data acquisition system controlled the probe, digitally sampled the probe output and pre-processed the data prior to output to a floppy disk. A schematic of the components included in the control system is included in Fig. 18.

III.D.1.) Probe Movement Control

Movement of the probe was accomplished through the use of three stepper motors and a 16 bit generator card located within the PC. Probe movement within the cascade in the pitchwise and spanwise direction was driven by two stepper motors located on an x-y traverse. These motors had a sensitivity of 0.0016 mm in the pitchwise direction and 0.0013 mm in the spanwise direction. Mechanical counters were used in each direction to provide a reference. These had a sensitivity of 0.64 mm and 0.53 mm in the pitchwise and spanwise directions respectively. The generator card and x-y traverse operation are described at in detail by Peters[6]. The location of the probe in the cascade, with its end-flow orientation and zero yaw angle, is illustrated in Fig. 19.

The probe support mechanism (Fig. 20) was used to provide two degrees of freedom including rotation of the probe about its axis and yaw angle adjustment. To

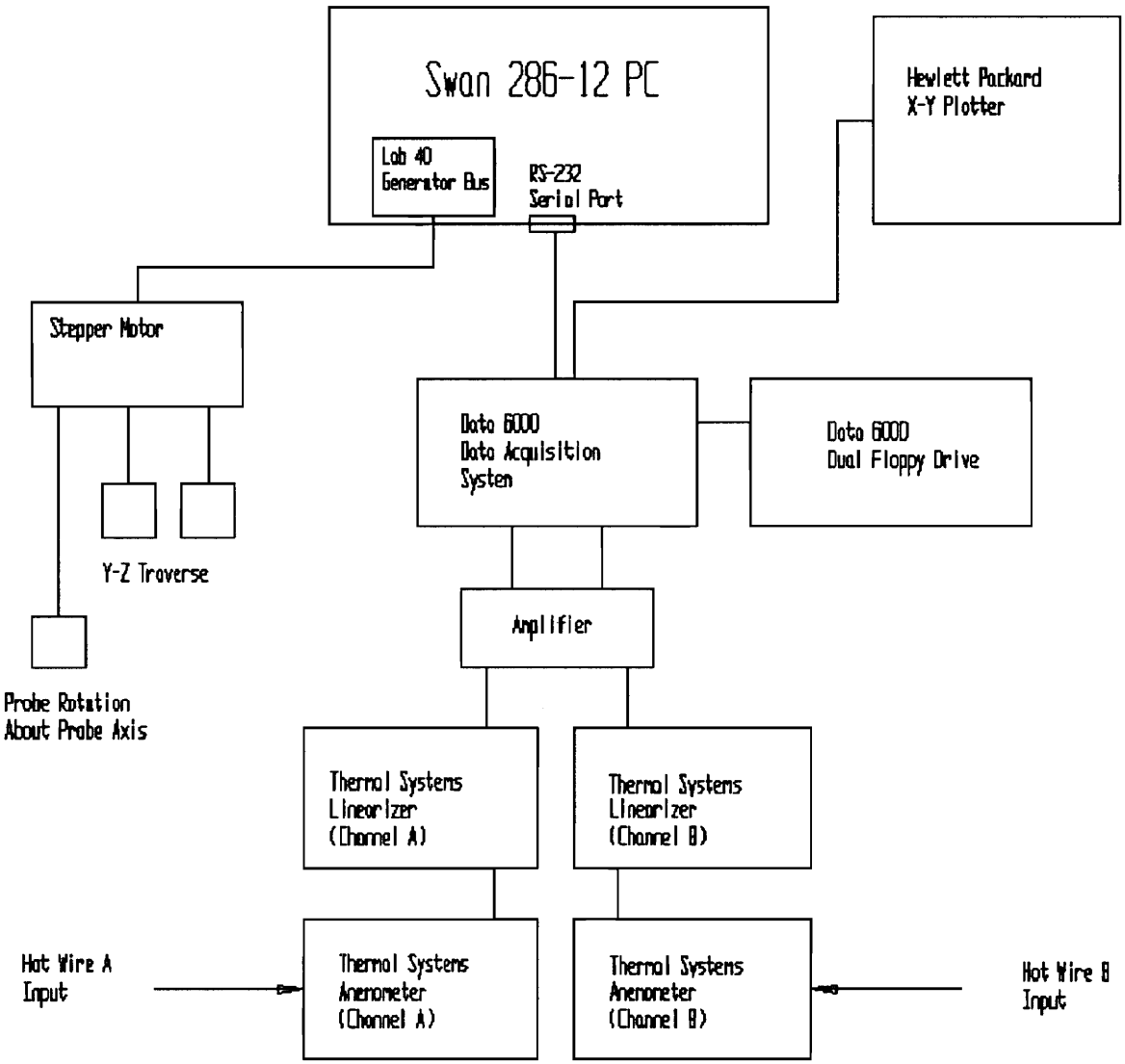

Figure 18. Schematic of Probe Control and

Data Acquisition System

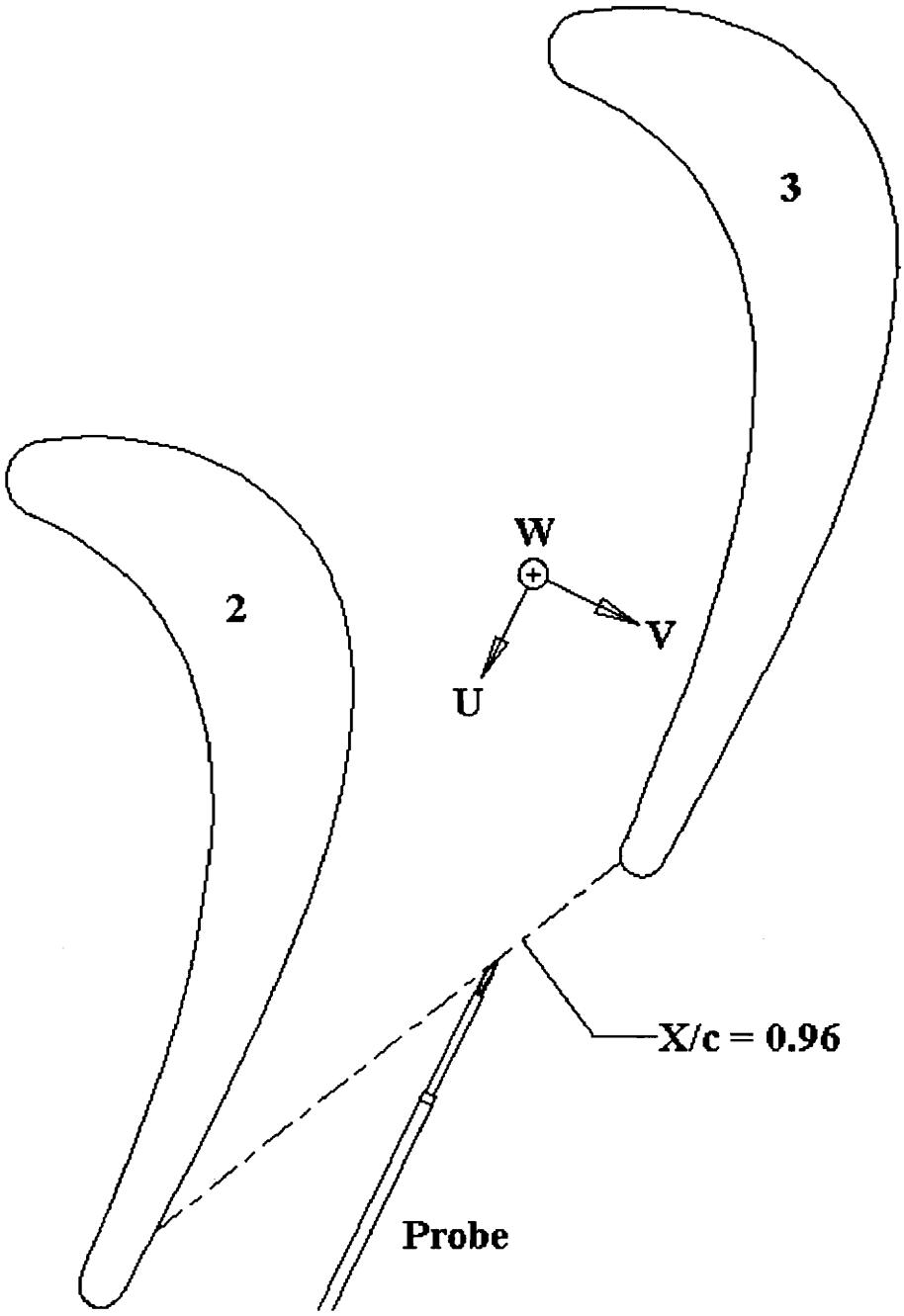

Figure 19. Location of Probe in Cascade (Zero Yaw)

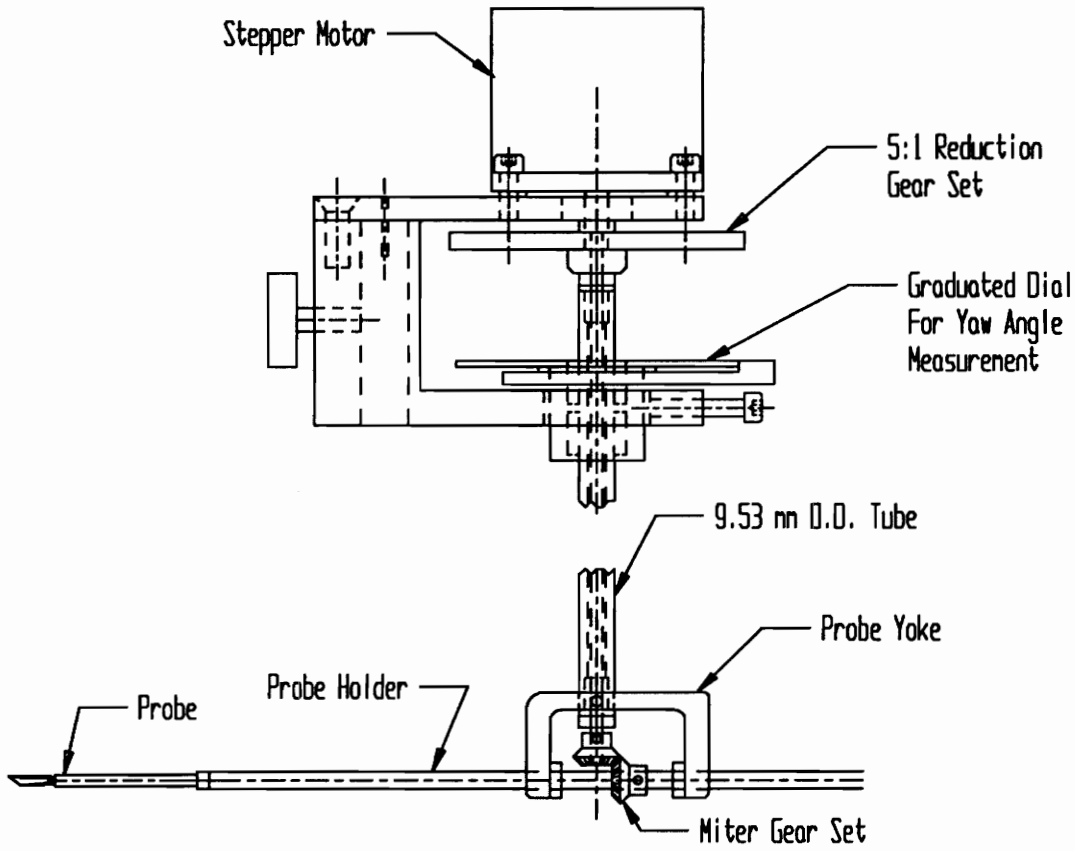

Figure 20. Probe Support and Rotation Mechanism

enable a high resolution rotation of the probe about its axis, a stepper motor with a 5:1 reduction gear set was mounted to the holder. The large reduction gear was directly coupled to a 6.35 mm (1/8 in) diameter shaft which ran through the inside of a 9.53 mm (3/8 in) o.d., 4.76 mm (3/16 in) i.d. shaft into the cascade test section, driving a 1:1 miter gear set which was directly connected to the probe holder. This provided an automated means of rotating the probe through any number of angular settings. Using the half-step mode (400 steps/revolution) of the stepper motor, the angular sensitivity was 0.18°. Adjustment of the probe yaw angle could be performed manually by loosening the screw on the graduated dial and turning the dial until the probe was at the desired yaw angle. Since this operation was rarely performed a manual adjustment procedure was adequate.

III.D.2. Data Acquisition System

The data acquisition system used in this experiment is illustrated in Fig. 18. Each hot wire was controlled with a constant temperature anemometer (TSI 1010A) operating with an overheat ratio of 1.5.

The outputs from the anemometers were fed into linearizers (TSI 1005B) which were used to linearize the signal. The following equation illustrates this process:

$$V_{out} = K_2\left(K_1 V_{in}^2 - c\right)^2 \qquad \text{(III2)}$$

Where V_{in} is the input voltage, V_{out} is the output voltage, K_1 and K_2 are the gains of squaring circuits 1 and 2 respectively and c is the additive constant in King's law. The linearizer used two independent squaring circuits for this squaring and had a zero suppression setting for subtracting the additive constant.

The linearizer outputs were fed into a correlator (TSI 1015C) which was used to vary the gain of the signal. This allowed attenuation and fine adjustment of the signal for setting reference voltages.

A Data 6000 Universal Waveform Analyzer was used to digitally sample and reconstruct the hot wire signals after attenuation and perform preprocessing operations. The Data 6000 used a model 610 data acquisition plug-in, a model 681 dual floppy disk drive and a Hewlett Packard model 7475A serial plotter. Manufacturer's specifications for the Data 6000 system are included in Table 2. The 681 dual floppy drive was able to store sampled arrays, command programs and control setup information in an ASCII format on IBM compatible 720 K double-density diskettes. The Hewlett Packard plotter could be used to plot the sampled arrays as they appeared on the Data 6000 screen. The Data 6000 system digitally sampled the hot wire signals at a frequency of 20 kHz, storing them in two 5120 point records. The Data 6000 then executed processing commands received over the serial port from the PC. These commands included first taking the mean values of both signals in order to calculate mean velocity components. Then the mean values of the signals were subtracted from their respective arrays in order to recover signals representing the fluctuating part of each hot wire signal and the rms of each of these new arrays was calculated. These signals were then multiplied together and the root mean square of the resulting signal was taken. These operations allowed the Data 6000 system to act in the place of a traditional analog correlator.

The Data 6000 as well as the stepper motor control system were controlled remotely by a Swan 286-12 personal computer. A single control program was written which coordinated the various parts of the experiment.

Manufacturer: Data Precision

16 Electronics Avenue

Danvers, Massachusetts 01923

Mainframe:

Model: Data 6000 Universal Waveform Analyzer
CPU: 16-bit - 10 MHz Motorola 68000
Memory: 96 K bytes ROM
56 K points RAM
Display: 9 in. CRT, X, Y, Z Type
Interfaces: Dual Floppy, IEEE 488, RS-232
Printer, Plotter, Terminal/Host
Scalar Operations: Period, frequency, cycle, rise time, fall time, delay, pulse width, overshoot, settling time, RMS, mean, area, energy, max, min, PP, local max, local min, maximum slope, positive crossing, negative crossing, any crossing
Record (Vector) Operations: Assign, delete, add, subtract, multiply, divide, spectrum magnitude plus phase for real or complex inputs, cross-correlation, auto-correlation, differentiation, integration, N point averaging

Data Acquisition Plug In:

Model: 610
Number of Channels: 2 independent
A/D Resolution: 14 bits
Input Isolation: Double guarded
Input Impedance: 1 MΩ, 20 pF
Input Coupling: dc, ac, gnd
Input Ranges: ±500 mV, ±5 V, ±50 V
Power Bandwidth (3dB): 100KHz (without filter)
Filter (switchable): 3-pole, 3dB @ 30 KHz
Maximum Sampling Rate: 100 Ksamples/second (1 channel operation)
50Ksamples/second (2 channel operation)

Table 2

Manufacturers Specifications for the Data 6000 Universal Waveform Analyzer

Chapter IV
Measurements and Procedure

IV.A Hot Wire Calibration Procedure

Probe calibration was performed in the calibration pipe described in section III.B. using the data acquisition system described in section III.D. The modified cosine law was used to model the hot wire response:

$$Q = Q_0 \sqrt{\cos^2 \Phi + k^2 \sin^2 \Phi} \qquad \text{(IV1)}$$

where Q is the effective cooling velocity, Q_0 is the magnitude of the flow velocity, Φ is the wire yaw angle, and $\mathbf{k^2}$ is the angular calibration constant (determined experimentally). The calibration of the hot wire also requires a constant to provide a linear response equation. Following the power law:

$$Q = E^a \qquad \text{(IV2)}$$

where E is the wire voltage and **a** is the experimentally determined linearity constant.

Prior to wire calibration, the wire signals were checked on both the Data 6000 Universal Waveform Analyzer and an oscilloscope for spurious signals resulting from a poor bridge balance. These signals were obvious when present, appearing as a periodic disturbance superimposed on the typical hot wire signal. The bridge balance on the anemometer was adjusted until no such spurious signals were present.

The linearity constant, **a**, was determined by positioning each wire perpendicular to the flow in the center of the calibration pipe and varying the flow velocity. The angular constant , $\mathbf{k^2}$,was determined by placing each wire in the center of the pipe, at the maximum pipe flow rate, in a horizontal position and varying the probe yaw angle. Typical values for the calibration constants were $\mathbf{k^2} = 0.0265$, $\mathbf{a} = 1.009$. Further details of the calibration procedure are given in Appendix B.

IV.B. Measurement Procedure

The hot wire measurements were done in both the calibration pipe and the cascade test section following a standard procedure employing the Data 6000 Universal Waveform Analyzer.

IV.B.1. Setting Zero and Reference Voltages

In both the calibration pipe and the cascade, the zero suppression and a reference voltage had to be set. In both cases the zero suppression was set by operating the probe with zero flow rate. The linearizer output was then zeroed using a digital multimeter by adjusting the level of zero suppression on the linearizer. The reference voltage was set in

the calibration pipe by placing each wire normal to the flow, at the flow rate to be tested, and adjusting the gain on the correlator so that the output was 1.0 V. The velocity at the centerline could be determined from a correlation that was found between the upstream static pressure and the exit velocity. In the cascade the reference was set by positioning the probe normal to the flow in a relatively undisturbed part of the flow and adjusting the correlator output to a voltage corresponding to the calibrated voltage for a pipe yaw angle equal to the wire angle α_0. The yaw angle was adjusted slightly (by $\tan^{-1}(V/U)$) to ensure that the wire yaw angle was the wire angle α_0 . The velocity at this reference point was obtained from the measurements of Peters[6] with a five hole probe. The reference flow velocity, Q_{ref}, was then the total velocity at this point as measured by Peters. The reference point was located at $Y/\Delta Y = 0.124$, $Z/\Delta Z = 0.55$ (point R in Fig. 18); the velocity components at this point were, U = 35.8 m/s,V = 0.9 m/s and W = 0.1 m/s yielding a cone angle of 1.3°. After each series of tests, the probe was returned to the reference point and the mean voltages were checked to insure consistency. After setting the reference voltage, the probe was returned to the zero yaw angle position.

IV.B.2. Experimental Data Grid at X/c = 0.96

Turbulence measurements were performed using both the rotatable x-wire probe and the single wire probe at the plane X/c = 0.96. Figure 21 shows the measurement plane with the grid of experimental data points. In the spanwise direction a total of 17 rows of data were taken from a spanwise height of 3.3% to 55%, in the pitchwise direction a total of 14 columns of data were taken from a pitchwise distance of 10.2% to 77%. The grid is the finest near the bottom endwall and near the suction side of the blade since the primary concern in this study was the tip leakage vortex region. The x-wire

probe was traversed to 7.9 mm (3.3% of span) from the bottom endwall which was near the point where the probe yoke contacted the endwall. The probe was traversed to 22.9 mm (10.2% pitch distance, 10.0 mm normal distance) from the blade suction side which was the point where the probe stem contacted a channel iron wind tunnel support.

In the region between the bottom endwall and the 3.3% span row of x-wire data, the single wire probe was traversed at three locations in the pitchwise direction. These traverse locations are marked in Fig. 21 with dotted lines. The first of these traverse locations was located at the exit of the tip gap where a total of 200 data points were taken in equally spaced intervals of 0.0254 mm (1/1000 inch) from the bottom endwall to a spanwise height of 5.08 mm (0.2 inches) which was slightly higher than the tip gap. At two other positions the probe was used to fill in the data for the distribution of $\overline{q^2}/U_o^2$.

IV.B.3. Rotatable X-Wire Measurements

The rotatable x-wire probe was used to measure all six components of Reynolds stress and the three components of mean velocity at all of the grid points marked by a point in Fig. 21. Prior to each run the zero suppression and reference voltages were set. The control program prompted for y and z counter values of the grid points to be used. The probe then traversed to the data point nearest the reference point to begin measurement. When the probe reached the data point the data acquisition program began measurements by turning the probe through six equally spaced angular positions. When all grid point measurements were completed the program wrote the results to a file and returned the probe to the reference position to check for any voltage drift. Voltage drift was consistently less than 1%.

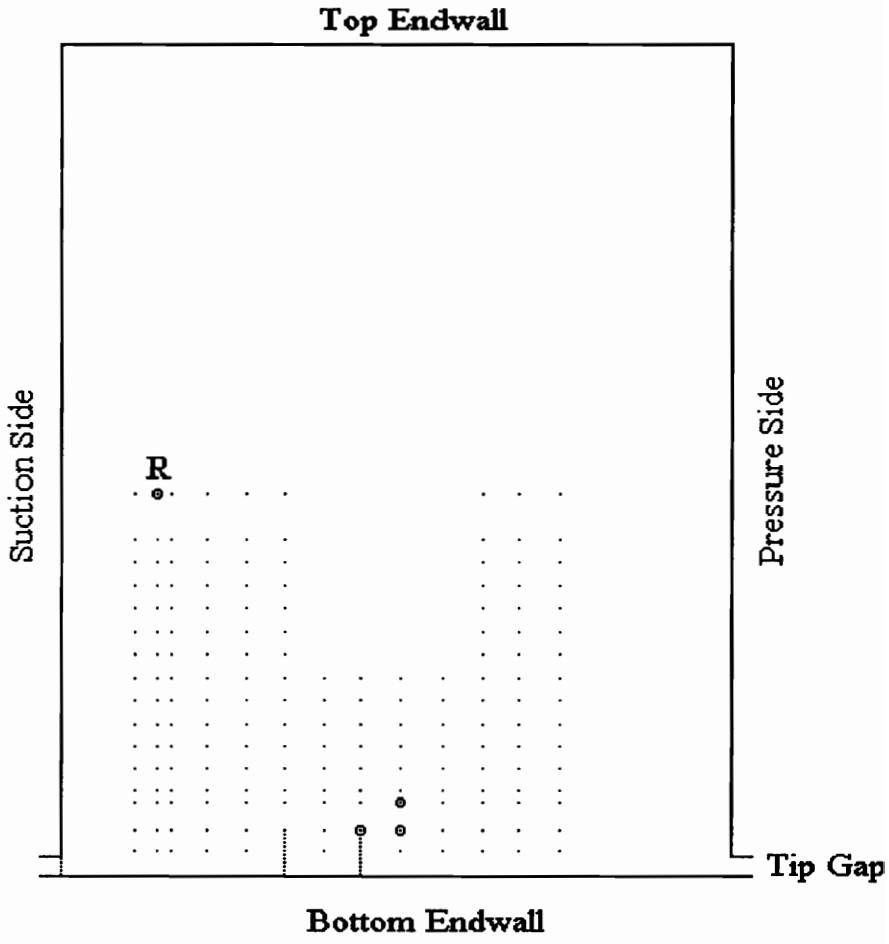

Figure 21. Measurement Plane Grid at X/c = 0.96

The typical test run consisted of about 20 data points. Each data point measurement took about one minute including traversing time. Extra time was added to the procedure depending on the distance from the reference point to the first data point. In most regions of the flow, particularly in the tip leakage vortex region, data points were taken more than once to ensure consistency. After a total of about 40 data points were taken, the probe was cleaned with acetone and recalibrated in the calibration pipe to avoid errors due to a buildup of dirt or oxidation.

In the first row of data points near the bottom endwall, large velocities in the tip leakage jet required that the probe yaw angle be set to 45 degrees. Typical cone angles in this region were from 30 to 75° due to large V components of velocity with small W components so that changing the yaw angle allowed the probe to operate with a new cone angle of $\leq 30°$.

At three data points in the region where the tip leakage jet separates and turns up, large W components of velocity caused the cone angle to fall outside of the 30° envelope which produces good results. These points are marked in Fig. 21 with a circle around a point. Since an adjustment of pitch angle was not possible with the current apparatus a new measurement scheme was devised. Initially the number of angular settings was increased from six to twelve since the accuracy increases with redundant data. While using twelve angular settings produced results closer to those expected by observing the data from other local points, the measured values still did not appear to be totally consistent. It was suspected that there were several positions where prong interference effects were very large. By eliminating the angular positions where either of the long prongs was below the corresponding short prongs, the results converged to values which were consistent with neighboring points. Out of twelve positions, three met the criteria for prong interference, giving enough positions to solve for all six components of

Reynolds stress. This method was tested in the calibration pipe at a yaw angle of 40° with good agreement with the results from using six angular settings with zero probe yaw angle (see Table 3 below).

	0°	40° 3 Pos.	40° 6X60°	Laufer	Lawn
U	0.911	0.910	0.909	0.915	0.915
V	0.036	0.030	0.021	N.A.	N.A.
W	-0.003	-0.003	-0.002	N.A.	N.A.
$\sqrt{\overline{u^2}}/U_\tau$	1.27	1.31	1.01	1.24	1.43
$\sqrt{\overline{v^2}}/U_\tau$	0.98	0.97	1.01	0.88	0.946
$\sqrt{\overline{w^2}}/U_\tau$	0.98	0.99	0.874	1.06	1.06
$\overline{uv}/U_\tau^2$	0.404	0.394	0.292	0.500	0.480
$\overline{q^2}/U_\tau^2$	3.54	3.64	4.01	3.43	4.06

Table 3
Results of Pipe Test of 3 Position Method

Chapter V
Results, Analysis and Discussion

V.A. Pipe Flow Testing

V.A.1. Measurement of Reynolds Stresses

In order to confirm the accuracy and repeatability of the data acquisition system, the anemometers, the test overall procedure and the hot wire configuration, the Reynolds stresses and turbulence kinetic energy were measured with a simple horizontal traverse in the calibration pipe. The results from these measurements were then compared to the results of Laufer [9], Shaffer [3] and Lawn [10].

Tests were done in fully developed, turbulent pipe flow since this is a simple flow which can easily be produced. The same pipe and probe holder used to calibrate the probe was used in this test. The calibration pipe was traversed with the x-wire hot wire probe using six equally spaced angular settings at five points along the centerline as shown in Fig. 22. The tests were run at the maximum pipe flow rate, yielding a Reynolds number of about 120,000. The sampling rate of the analog-digital converter was 20,000 Hertz .

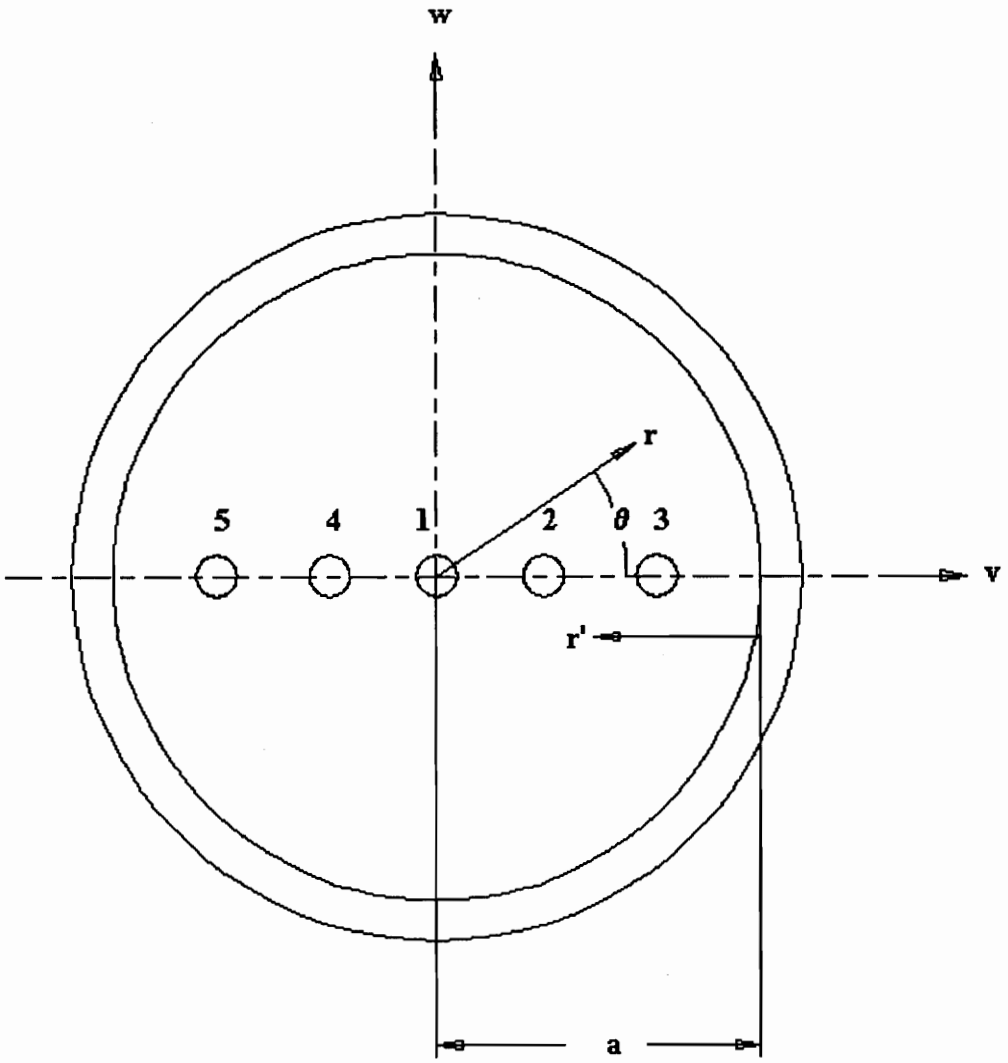

Point 1	r'/a = 1.00
Point 2	r'/a = 0.67
Point 3	r'/a = 0.32
Point 4	r'/a = 0.62
Point 5	r'/a = 0.26

Figure 22. Location of Pipe Traverse Measurement Points

The results of this test were plotted against the results obtained by Laufer and Lawn in Figs. 23, 24, 25, 26, 27, 28 and 29. These plots show Lawn's results at a Reynolds number of 164,000, the results from this test and a linear interpolation of Laufer's results between Reynolds numbers of 50,000 and 500,000 to a Reynolds number of 120,000. All of the turbulence quantities were normalized by the shear velocity, U_τ, which was calculated from the pressure drop along the last 5.9 m of the pipe (see Appendix A.1.). The axial velocity was normalized by the maximum velocity, i.e., the pipe centerline velocity. Some of the turbulence results of Laufer were disputed by Lawn, however, they are included here to enable comparison.

The axial velocity distribution, Fig. 23, is in close agreement to the results of Laufer. The magnitude of the difference compared to Laufer's results averages 1.4%. The measured flow angles range from maxima of 0.85° and 0.75° to minima of 0.24° and -0.74° for yaw and pitch angles, α_r and α_p, respectively.

The normal stresses are shown in Figs. 24, 25 and 26. The axial normal stresses, $\sqrt{\overline{u^2}} / U_\tau$, are shown in Fig. 24. The magnitude of the difference compared to Laufer's results averages 11.1%, and -4.5% compared to Lawn's results. The radial normal stresses, $\sqrt{\overline{v^2}} / U_\tau$, shown in Fig. 25, vary from Laufer's results by an average of 14.4%, and 6.7% compared to Lawn's results. The circumferential normal stresses, $\sqrt{\overline{w^2}} / U_\tau$, are shown in Fig. 26. The magnitude of the difference compared to Laufer's results averages 6.4% and 6.3% compared to Lawn's results.

The turbulence kinetic energy, $\overline{q^2} / U_\tau^2$, distribution is plotted in Fig. 27. The test results vary from those of Laufer by an average of 18.1% and 0.4% compared to Lawn's results.

The primary shear stress, $\overline{uv} / U_\tau^2$ is similarly plotted in Fig. 28. The theoretical distribution of the primary shear stress decreases linearly from 1.0 at r'/a = 0 to 0.0 at r'/a = 1. All of the measured values were lower than those found by Laufer. The results varied from Laufer's results by an average of -12%. The agreement with Lawn's results are better, -7.1%, however Lawn's results were systematically low, apparently because of flow asymmetry in his pipe. The shear stress at the center of the pipe was very small (0.021) which was expected since the shear stress at the center of a pipe should theoretically be zero. The measured distribution also shows the expected linear variation across the pipe.

Figure 29 is a plot of the correlation coefficient, $\frac{\overline{uv}}{\sqrt{u^2}\sqrt{v^2}}$ compared to Laufer's results. The results vary from Laufer's by a maximum of 14%, averaging 11% difference.

Table 4 summarizes the differences in magnitude of all measured quantities from the interpolated values obtained from Laufer, and from the data of Lawn. Included is the maximum, minimum and average magnitude differences. The differences from Lawn are given in parenthesis.

	Average % Difference	Maximum % Difference	Minimum % Difference
Velocity	1.4% (1.4%)	2.6% (2.6%)	-0.8% (-0.8%)
$\sqrt{\overline{u^2}} / U_\tau$	11.1% (-4.5%)	14.2% (-2.7%)	3.3% (-7.5%)
$\sqrt{\overline{v^2}} / U_\tau$	14.4% (6.7%)	20.7% (12.3%)	8.7% (1.7%)
$\sqrt{\overline{w^2}} / U_\tau$	6.4% (6.3%)	8.0% (8.8%)	5.1% (1.5%)
$\overline{uv} / U_\tau^2$	-12.3% (-7.1%)	-5.7% (1.0%)	-19.6% (16.0%)
$\overline{q^2} / U_\tau^2$	18.1% (0.4%)	25.5% (3.5%)	10.4% (-2.7%)

Table 4. Comparison of Pipe Traverse Results To

Data Given By Laufer[9] and (Lawn)[10]

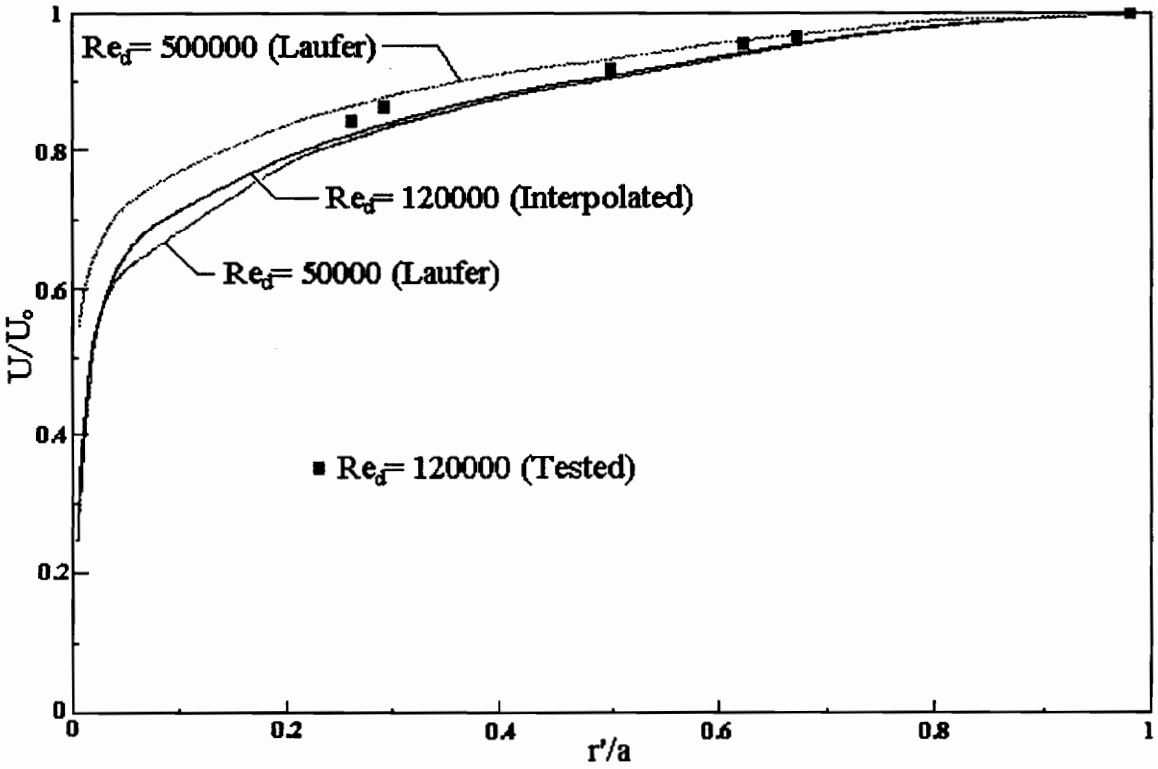

Figure 23. Comparison of Axial Velocity Measured in Calibration Pipe with the Results of Laufer

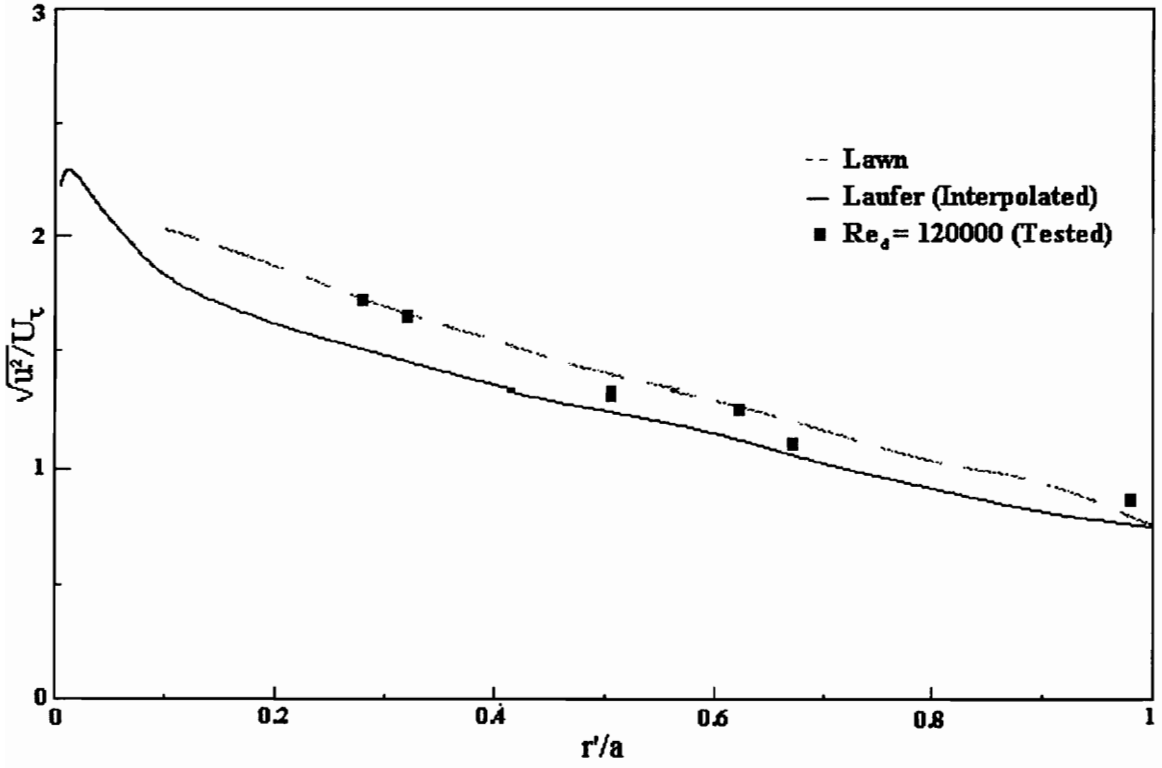

Figure 24. Comparison of Normal Stress, $\frac{\sqrt{u^2}}{U_\tau}$,

Measured in Calibration Pipe With the Results of Laufer and Lawn

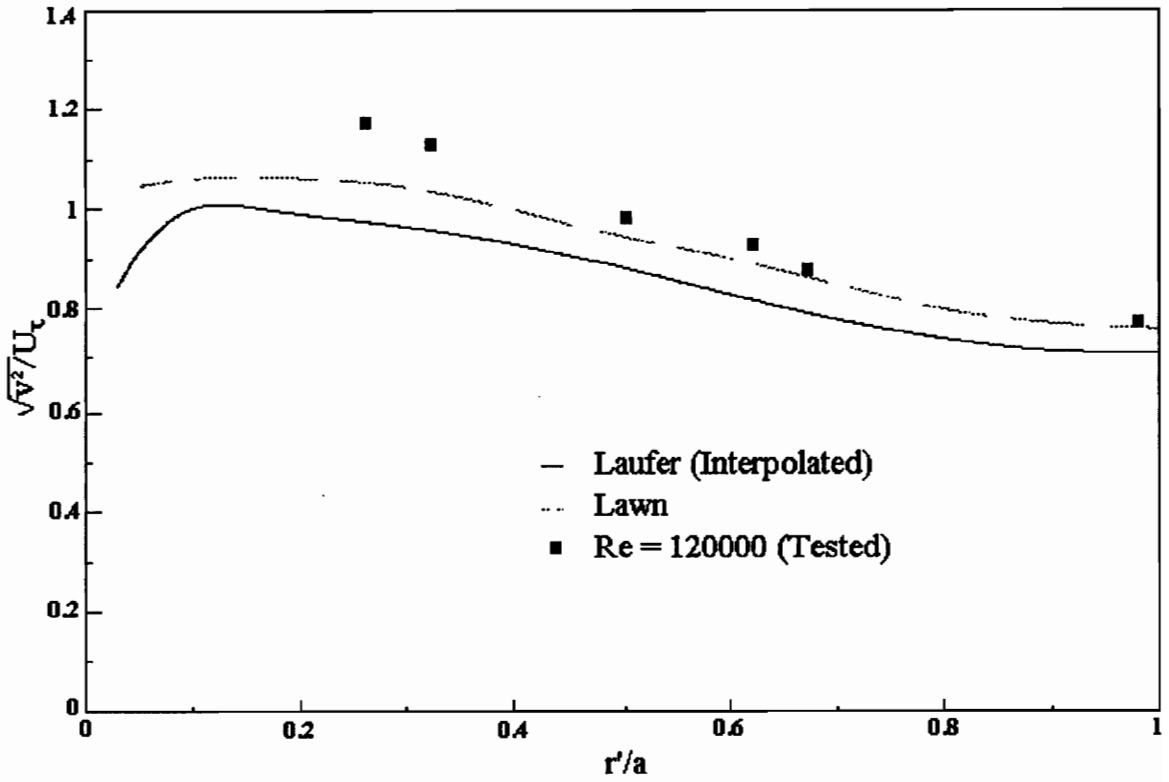

Figure 25. Comparison of Normal Stress, $\frac{\sqrt{v^2}}{U_\tau}$,

Measured in Calibration Pipe With the Results of Laufer and Lawn

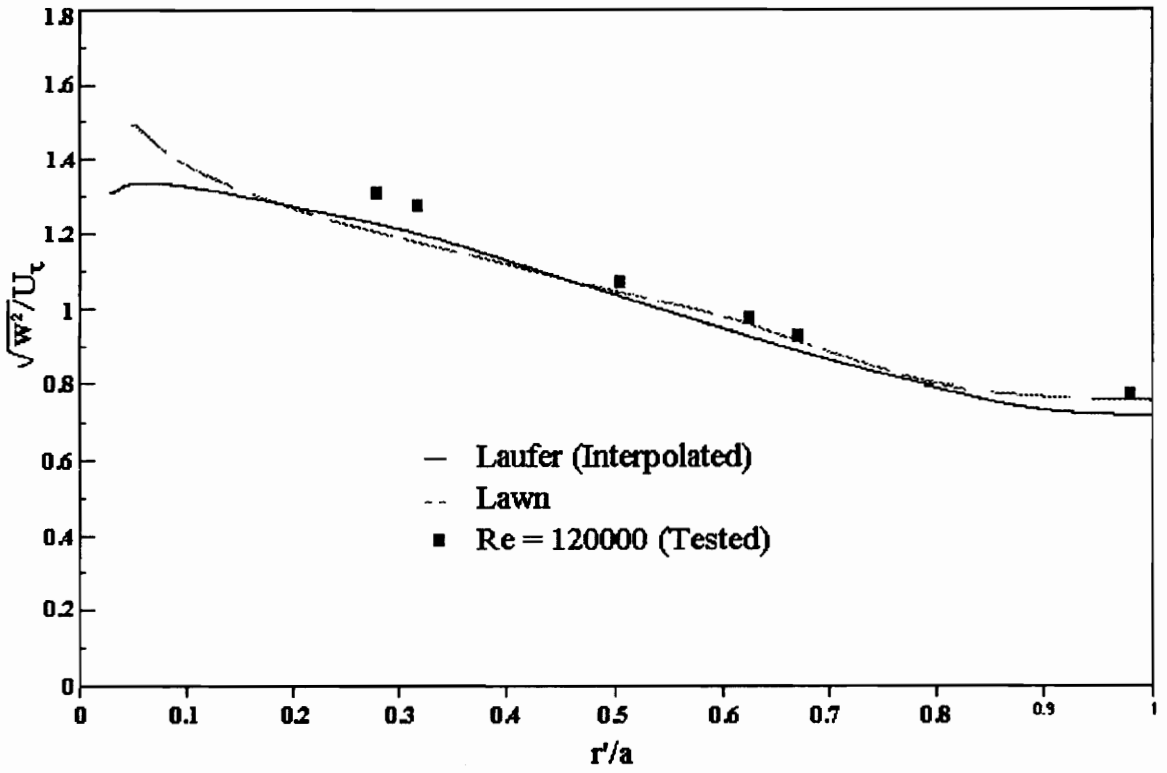

Figure 26. Comparison of Normal Stress, $\frac{\sqrt{w^2}}{U_\tau}$

Measured in Calibration Pipe With the Results of Laufer and Lawn

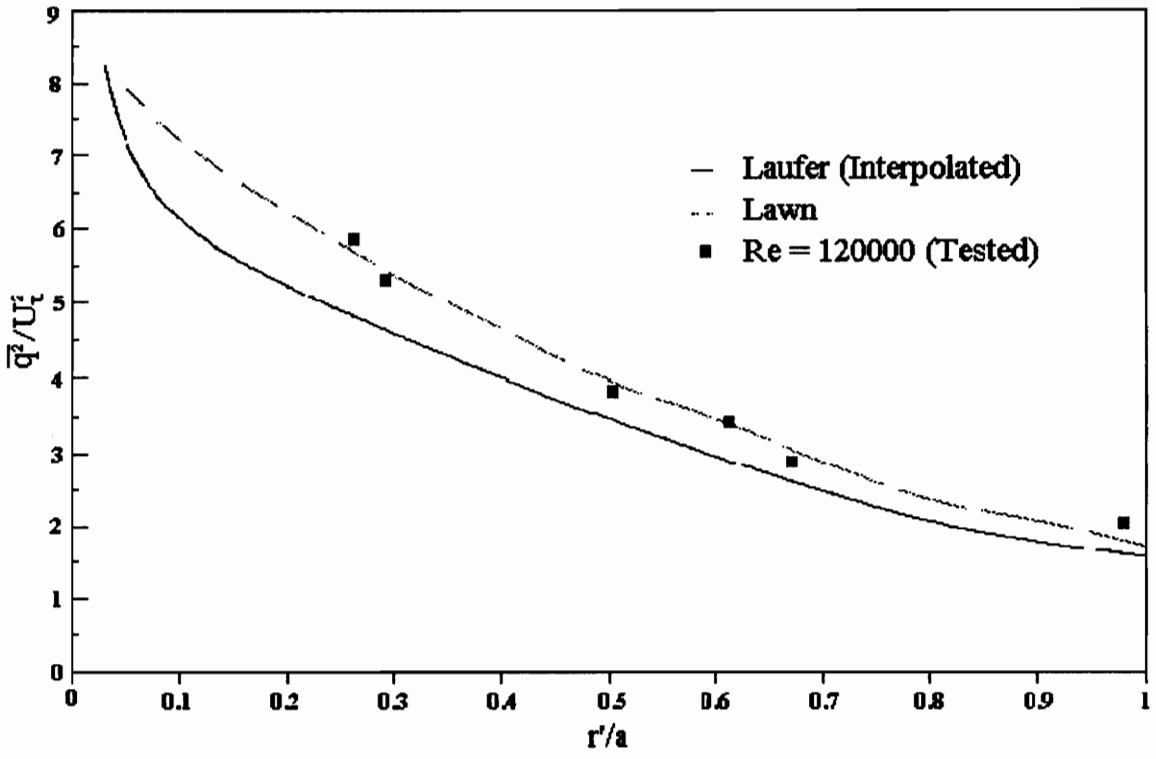

Figure 27. Comparison of Turbulence Kinetic Energy, $\frac{\overline{q^2}}{U_\tau^2}$

Measured in Calibration Pipe With the Results of Laufer and Lawn

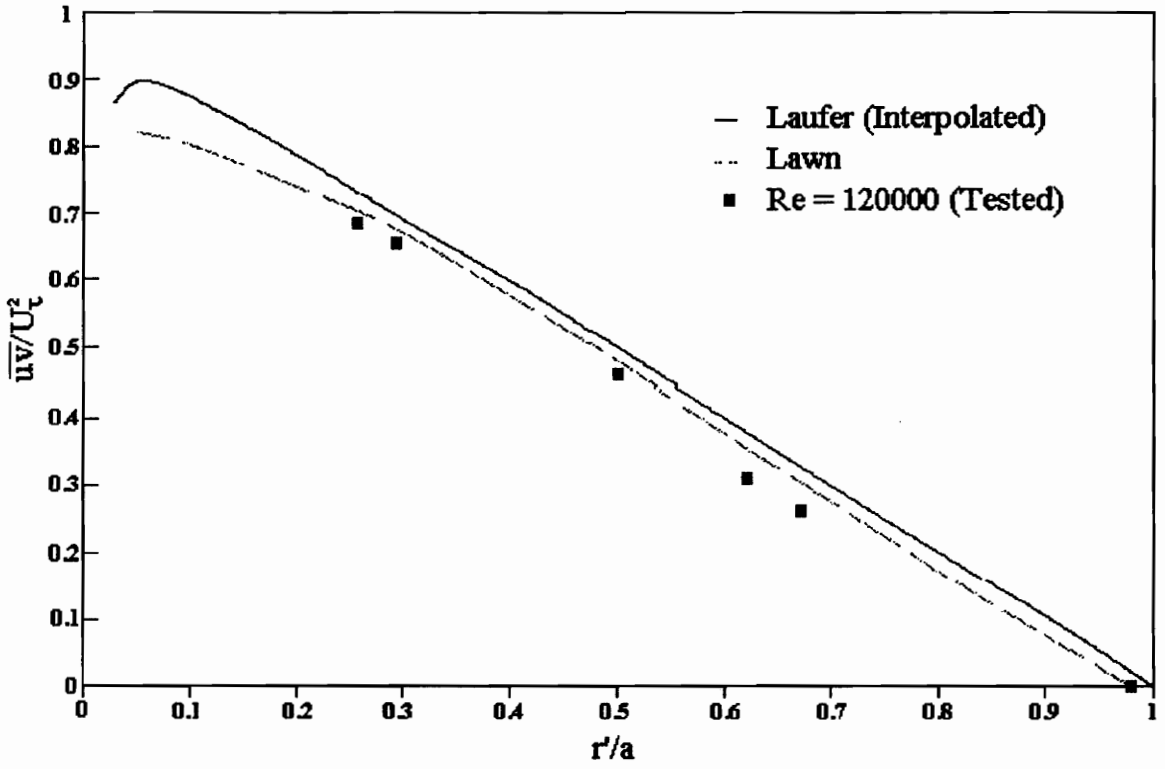

Figure 28. Comparison of Shear Stress, $\frac{\overline{uv}}{U_\tau^2}$,

Measured in Calibration Pipe With the Results of Laufer and Lawn

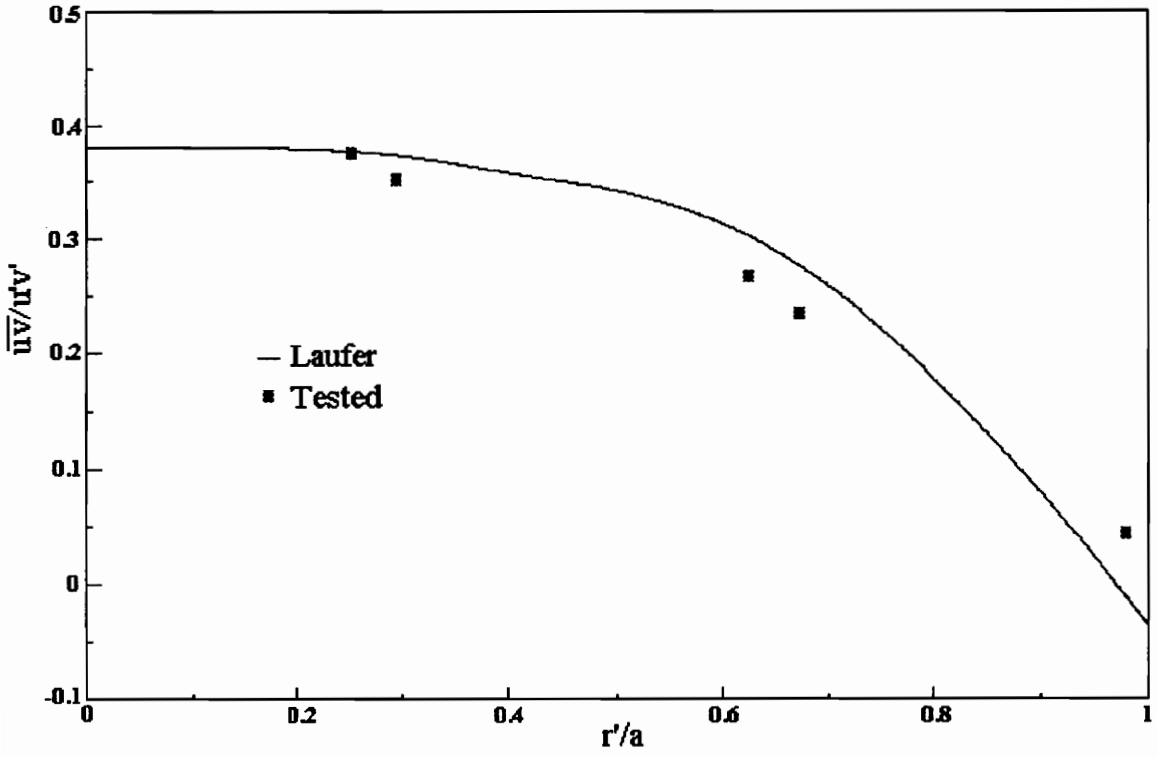

Figure 29. Comparison of Correlation Coefficient, $\frac{\overline{uv}}{\sqrt{u^2}\sqrt{v^2}}$

Measured in Calibration Pipe With the Results of Laufer

V.A.2. Digital Sampling

The sampling rate and population settings of the Data 6000 Universal Waveform Analyzer were intended to provide a sample which was characteristic of the flow. The Data 6000 was set at a sampling rate of 20,000 Hertz and a population of 5120 points for both the pipe flow testing and the cascade testing. With a sampling rate of 20,000 Hertz and a population of 5120 points the length of time per set of data taken was 0.256 seconds. For a maximum flow rate of 30.0 m/s in the calibration pipe, this amounts to a set of data in which 7.68 m of the flow passes the probe. If a typical large eddy size is 0.05 m the set of data will contain 153 large eddies. This means that about 33 samples will be taken for each large eddy. A typical hot wire signal taken under these conditions in the calibration pipe is shown in Fig. 30a. Both wires A and B are sampled simultaneously.

A test was performed to establish the repeatability of the experimental system. The procedure to accomplish this consisted of placing the probe in the pipe at r'/a = 0.5 with a zero yaw angle and measuring the Reynolds stresses at various sampling rates. Six equally spaced angular positions were used.

The sampling rates used were 1000 , 2000, 5000 , 10000 and 20000 Hertz. Table 5 shows the results including mean velocities and turbulence quantities. The maximum flow angles in magnitude were 2.5° and -0.5° for α_T and α_p respectively. The axial velocity varied little, with a maximum deviation from the mean of 2.1%. This was not expected to vary appreciably since the velocity is calculated from the mean voltages which should be relatively constant.

The largest deviations from the mean for the normal stresses were 5.3% for $\sqrt{\overline{u^2}}/U_\tau$, -2.0% for $\sqrt{\overline{v^2}}/U_\tau$, and 3.8% for $\sqrt{\overline{w^2}}/U_\tau$. The shear stress, $\overline{uv}/U_\tau^2$, had a maximum deviation from the mean of 6.8%. This could be an indication of the difficulty of accurately measuring the shear stress components. The turbulence kinetic energy, $\overline{q^2}/U_\tau^2$, had a maximum deviation from the mean of 3.3%. The results of this test are summarized in Table 5.

Freq. Hz	1000	2000	5000	10000	20000	Laufer	Lawn
U	0.924	0.930	0.928	0.931	0.911	0.915	0.915
V	0.006	0.010	0.009	0.009	0.036	N.A.	N.A.
W	-0.005	-0.007	-0.007	-0.008	-0.003	N.A.	N.A.
$\sqrt{\overline{u^2}}/U_\tau$	1.33	1.34	1.34	1.31	1.27	1.24	1.43
$\sqrt{\overline{v^2}}/U_\tau$	0.98	0.96	0.98	0.98	0.98	0.88	0.946
$\sqrt{\overline{w^2}}/U_\tau$	1.05	1.06	1.03	1.04	1.07	1.06	1.06
$\overline{uv}/U_\tau^2$	0.437	0.468	0.447	0.463	0.464	0.500	0.480
$\overline{q^2}/U_\tau^2$	3.838	3.848	3.836	3.761	3.72	3.43	4.06

Table 5
Results of sampling rate testing

A typical hot wire signal taken in the turbine cascade is shown in Fig. 30b. This was taken using the single wire probe in the region where the tip leakage flow separated from the bottom endwall.

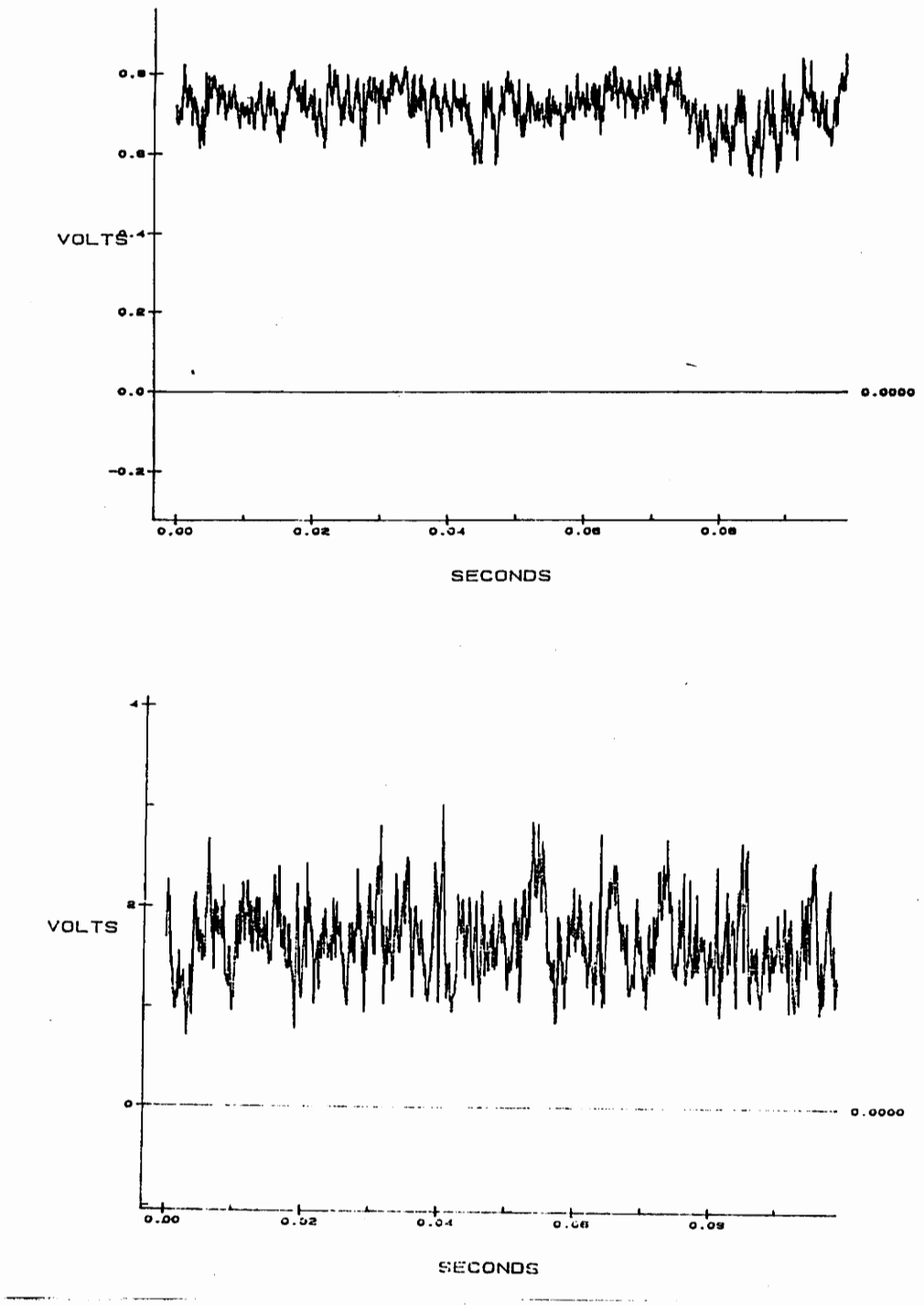

Figure 30. Typical Hot Wire Signals:

a) from the calibration pipe; b) from the turbine cascade

V.A.3. Effects of Varying Probe Yaw Angle

The flow in the calibration pipe was used to determine the hot wire probe's ability to measure Reynolds stresses and mean velocities at varying yaw angles.

Measurements were taken in the pipe along the horizontal centerline at r'/a = 0.5 while the probe yaw angle was varied through 0°, 10°, 20°, 30° and 40°. Six equally spaced angular probe settings were used and the frequency of digital sampling was 20,000 Hertz.

Table 6 shows the results of this test and compares these data to the results of Laufer. The mean axial velocities were found to be within 0.6% of Laufer's and Lawn's data for all flow angles, with an average magnitude difference of 0.5%. The maximum flow angles were 2.3° and -2.1° for α_r and α_p respectively. The radial and circumferential velocity components were found to be less than 4.0% of the axial velocity in all cases. The normal stresses are in general agreement within 11.2% of Lawn's data for yaw angles of 0°, 10°and 20° with the greatest discrepancies for $\sqrt{\overline{u^2}} / U_\tau$ at a yaw angle of 40° (29%). The shear stress, $\overline{uv} / U_\tau^2$, is also in general agreement with theoretical values for probe yaw angles of 0°, 10°, 20° and 30° (within 21%) with a maximum deviation of 29.6% at a yaw angle of 40°. Lawn's measurement technique also gave errors in the shear stresses, up to -9% at r'/a = 0.5. Values of turbulence kinetic energy agree for yaw angles of 0°, 10°, 20°, 30° and 40° with an average deviation from Lawn's data of 6.8%.

	0°	10°	20°	30°	40°	Laufer	Lawn
U	0.911	0.910	0.911	0.911	0.909	0.915	0.915
V	0.036	0.003	0.014	0.017	0.021	N.A.	N.A.
W	-0.003	-0.026	-0.033	-0.022	-0.002	N.A.	N.A.
$\sqrt{\overline{u^2}}/U_\tau$	1.27	1.31	1.35	1.45	1.01	1.24	1.43
$\sqrt{\overline{v^2}}/U_\tau$	0.98	0.97	0.96	0.91	1.01	0.88	0.946
$\sqrt{\overline{w^2}}/U_\tau$	1.07	1.02	1.02	0.97	0.874	1.06	1.06
$\overline{uv}/U_\tau^2$	0.464	0.434	0.395	0.479	0.352	0.500	0.480
$\overline{q^2}/U_\tau^2$	3.72	3.70	3.78	3.70	4.01	3.43	4.06

Table 6
Results of Yaw Angle Variation Test

V.B. Cascade Testing

V.B.1. Mean Velocity Distribution

The velocity distribution was calculated from the mean voltages of the hot wires in order to allow comparisons with the results of Peters[6]. The primary velocity, U, distribution is very close to Peters' results with results in agreement within 3 m/s. The calculated secondary velocities are shown as a vector plot in Fig. 31. The secondary velocity components V and W were consistently somewhat lower than Peters' measurements with V agreeing within 4 m/s and W agreeing within 5 m/s. The maximum secondary velocity found was 20.1 m/s located in the bottom row of

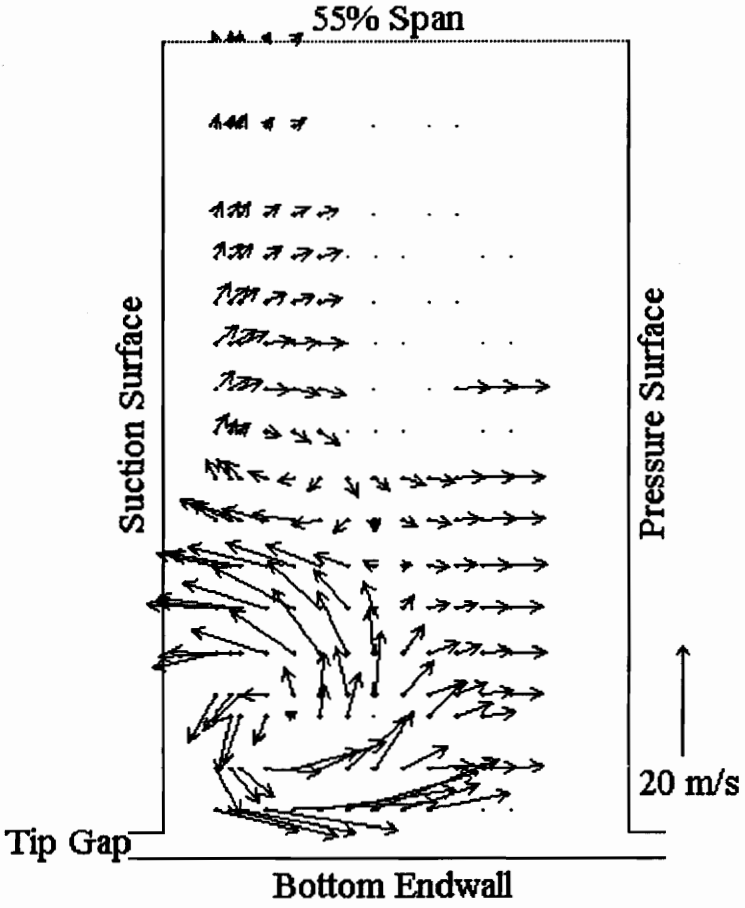

Figure 31. Secondary Velocity Vectors Projected into the Cross Sectional Plane at X/c = 0.96

measurements immediately below the center of the tip leakage vortex. The core of the tip leakage vortex, as defined by a zero secondary velocity at a grid point was found at $Y/\Delta Y = 0.28$ and $Z/\Delta Z = 0.095$ this is slightly higher than the point that Peters found, $Z/\Delta Z = 0.067$.

Besides a direct velocity magnitude comparison a convenient means of comparing velocity measurements is by comparing the cone angle (Eq. III1). Figure 32 shows contours of cone angle as measured with the rotatable x-wire probe. Comparing Fig. 32 with the cone angle plot calculated from Peters' [6] data in Fig. 33 it can be seen that the results are in close agreement with the exception of a few points in the region where the vortex turns up from the endwall region. It is in this region that the W component of velocity becomes large enough to cause the cone angle to be greater than 30°. Here the technique for large pitch angles was used to minimize the error (see section IV.C.3). In the plane at 3.3% spanwise height, the cone angles were in the 35-55° range caused by a large V component of velocity. For measurements at that height, the probe was set to a yaw angle of 45° in order to reduce this large cone angle.

V.B.2. Cascade Turbulence Measurements

V.B.2.i. Tip Gap Exit Measurements

A traverse was taken at the exit plane of the tip gap with the single wire probe in order to quantify the level of turbulence exiting the tip gap. Measurements were taken from the bottom endwall to a distance of 5.08 mm (0.20 in.) in increments of 0.0254 mm (1/1000 in.). The single wire probe was positioned normal to the flow based on the mean of the flow angle measurements taken with a three hole probe at the tip gap exit by

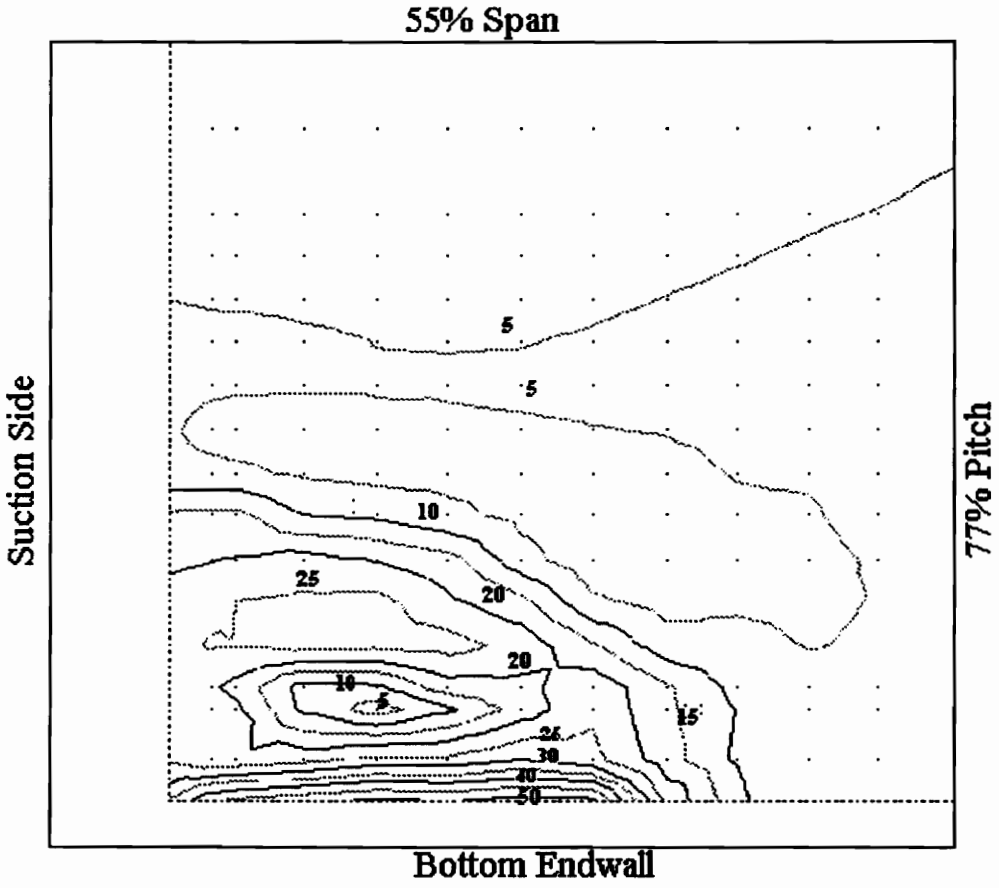

Figure 32. Contours of Cone Angle

Measurement Plane at X/c = 0.96

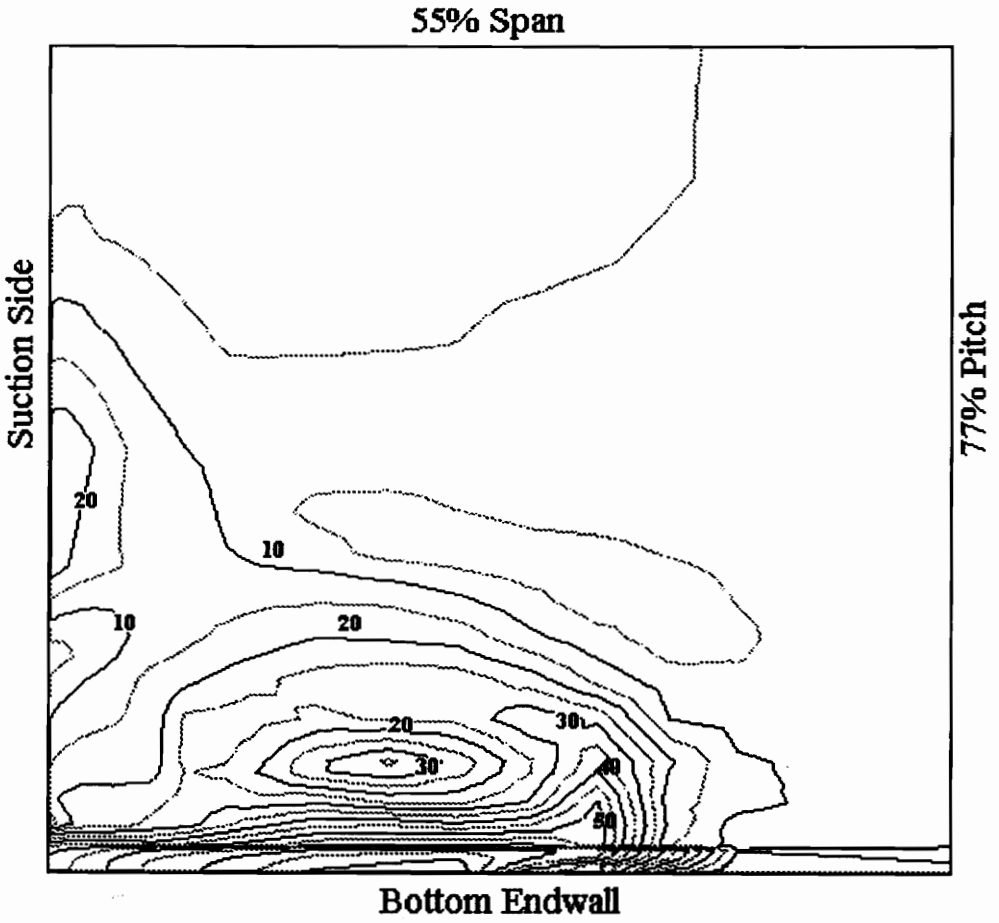

Figure 33. Contours of Cone Angle Calculated

From the Data of Peters at X/c = 0.96

Dishart. The turbulence kinetic energy was calculated by assuming isotropic turbulence at the tip gap exit.

A plot of the mean velocity distribution plotted against the percentage of the tip gap height is given in Figure 34. The distribution closely agrees with Dishart's measurements at the tip gap exit at X/c = 0.965. Near the bottom endwall the velocity profile appears the same as a typical turbulent boundary layer. The freestream flow which is unaffected by the separation from the blade at the tip gap entrance (see Fig. 2) can be seen above this boundary layer. At points above this is a region of mixing caused by the large separation at the entrance.

A plot of the measured turbulence kinetic energy distribution is given in Fig. 35. The distribution agrees with the description in Tilton's [4] model. The turbulence near the bottom endwall is the same distribution as that found in a turbulent boundary layer with a peak value of $\overline{q^2}/U_0^2 = 0.46$ (rms turbulence intensity = 40%). The turbulence in the freestream flow is somewhat lower with typical values of $\overline{q^2}/U_0^2 = 0.26$ (rms turbulence intensity = 30%). In the mixing region the turbulence is again quite high with values of $\overline{q^2}/U_0^2 = 0.44$ (rms turbulence intensity = 38%). The turbulence level then decreases to the wall as the flow becomes more orderly.

V.B.2.ii. Turbulence Kinetic Energy at X/c = 0.96

The turbulence kinetic energy was measured at all x-wire grid points as well as several points in the region very close to the bottom endwall. The x-wire values were calculated in the traditional way while the single wire values had to be calculated by assuming isotropic turbulence . Contours of the resulting turbulence kinetic energy distribution are plotted in Fig. 36. Maximum values of $\overline{q^2}/U_0^2$ are found in the tip gap jet

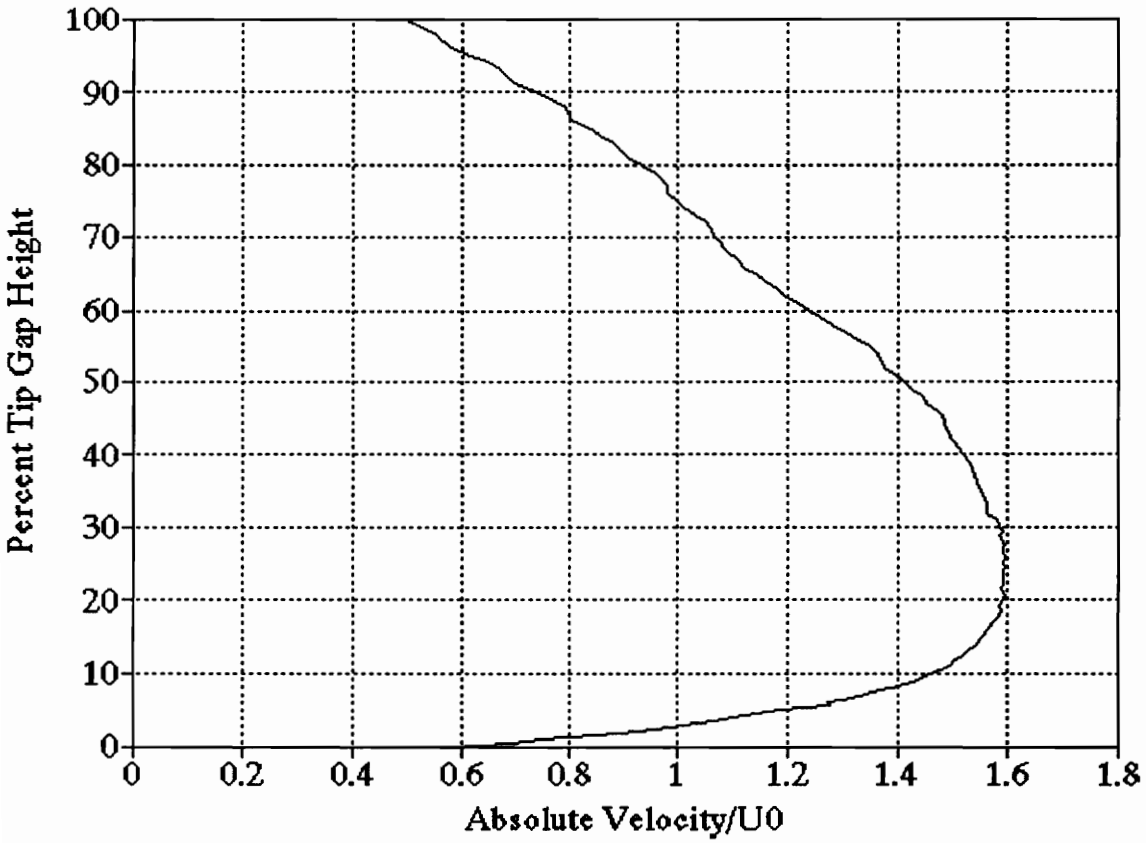

Figure 34. Absolute Velocity Measurements at Tip Gap Exit,

X/c = 0.96, Taken with single wire probe

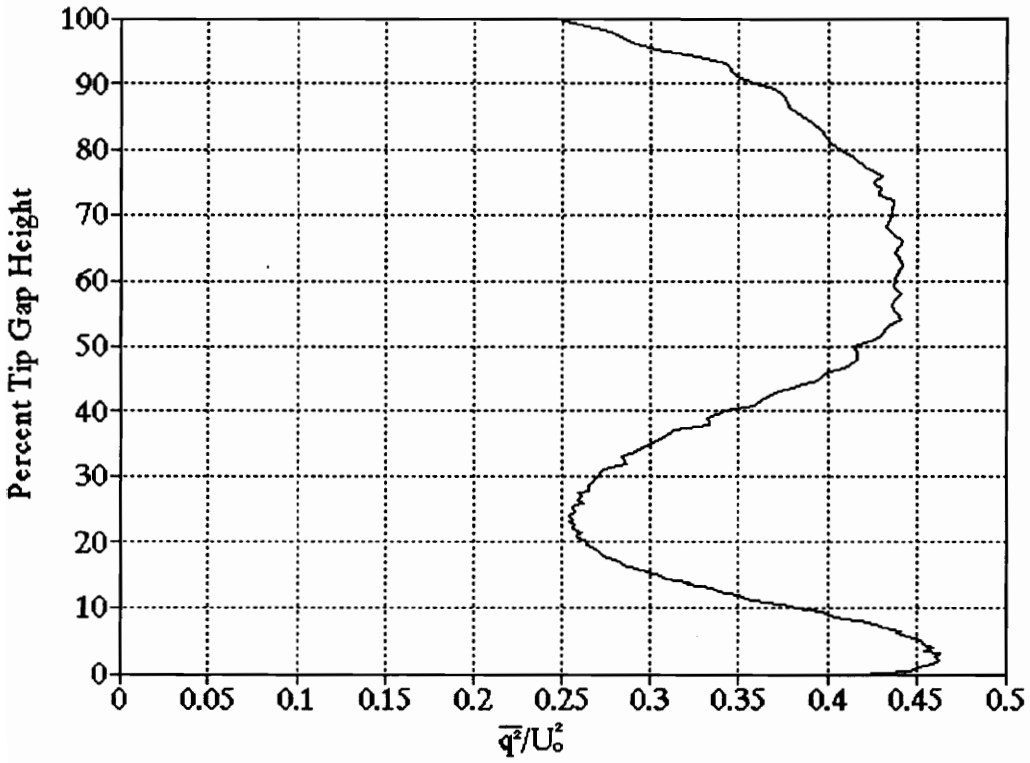

Figure 35. Turbulence Kinetic Energy Measurements , $\overline{q^2}/U_0^2$,

at Tip Gap Exit ,X/c = 0.96, Taken With Single Wire Probe

region near the bottom endwall. The maximum value of $\overline{q^2}/U_0^2$ observed was about 1.2 (rms turbulence intensity of $\approx$ 63%) in the area where the flow separates from the bottom endwall and turns up. This high turbulence then is convected around the tip leakage vortex, continuously dissipating to a value of about $\overline{q^2}/U_0^2 \approx 0.6$ near the suction surface. A region of moderate turbulence ($\overline{q^2}/U_0^2 \approx 0.6$) is present in the shear layer where the passage vortex meets the tip leakage vortex. The turbulence kinetic energy away from the passage and tip leakage vortices is generally characterized by low values in the range of 0.001 to 0.002 (1.8 % to 2.6% rms) with a minimum of 0.0002 (0.8% rms) at 55% span. It is worth noting that the region near the suction side of the blade was not included in this study and it is expected that turbulence is higher than these values due to the boundary layer.

The core of the tip leakage vortex has much lower turbulence than the outside of the vortex, $\overline{q^2}/U_0^2 \approx 0.12$, 20% rms. The turbulence in the tip leakage vortex core may appear to be low compared to other regions of the flow, however in the study of Shaffer, the maximum value of turbulence kinetic energy of 0.2 was found in the blade wake downstream of the trailing edge at 20% span. This suggests that the core turbulence is not insignificant, and that neglecting this turbulence in a 3-D viscous calculation is probably not reasonable.

The locally high values in the region where the tip leakage jet separates from the bottom endwall and turns upward indicate a generation of turbulence at the separation. This is physically easy to visualize since the turning of this high energy fluid requires large amounts of stress on a given element and thus a higher level of turbulence kinetic energy. The turbulence eventually begins to dissipate as it is convected around the outside of the vortex.

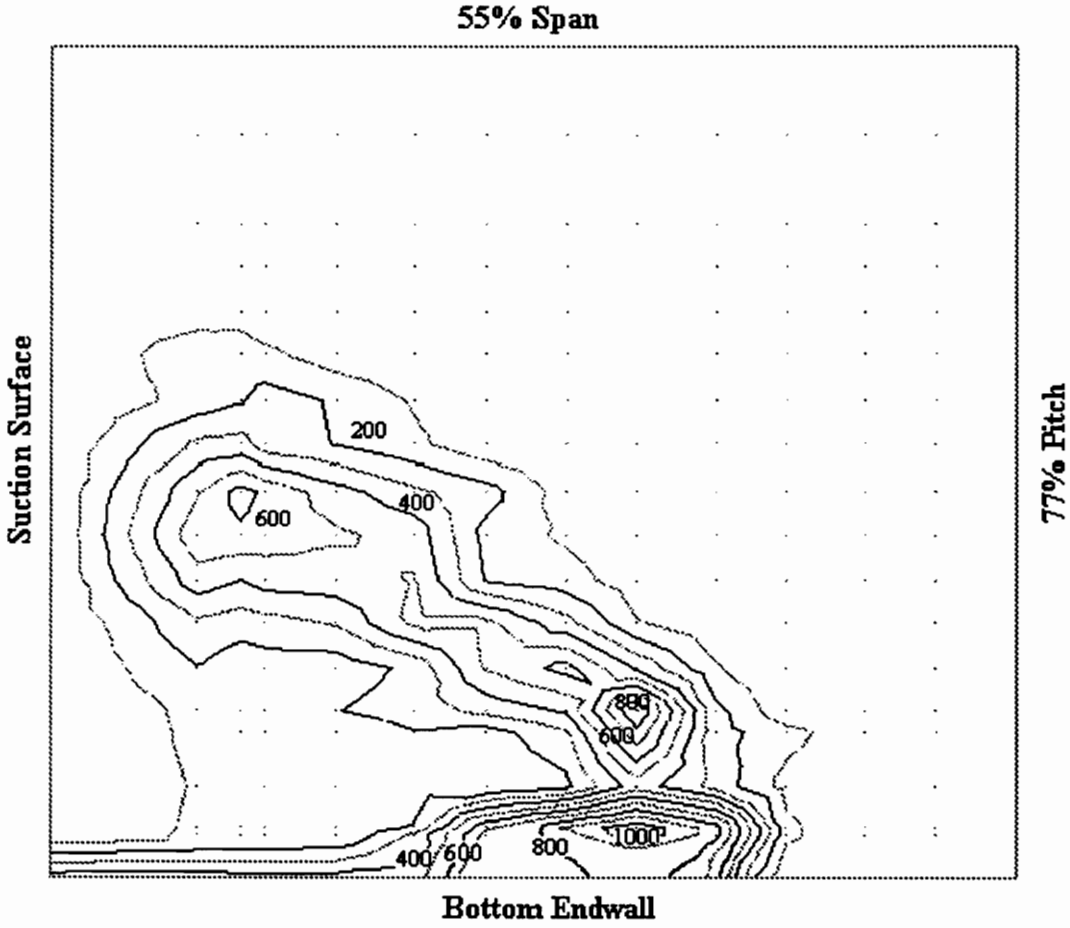

Figure 36. Contours of Turbulence Kinetic Energy, $\frac{\overline{q^2}}{U_0^2} * 1000$

Measurement Plane at X/c = 0.96

V.B.2.iii. Mass Averaged Turbulence Kinetic Energy

A mass average of the kinetic energy is defined by:

$$\frac{\overline{\overline{q^2}}}{U_0^2} = \frac{\int_{.102\Delta Y}^{.77\Delta Y}\int_{0}^{.5\Delta Z}\left(u^2+v^2+w^2\right)\rho V_n dz dy}{\int_{.102\Delta Y}^{.77\Delta Y}\int_{0}^{.5\Delta Z}\rho V_n U_0^2 dz dy} \qquad \text{(V1)}$$

or in finite difference form:

$$\frac{\overline{\overline{q^2}}}{U_0^2} \cong \frac{\sum_{.102\Delta Y}^{.77\Delta Y}\sum_{0}^{.5\Delta Z}\rho V_n\left(u^2+v^2+w^2\right)\Delta z \Delta y}{\sum_{.102\Delta Y}^{.77\Delta Y}\sum_{0}^{.5\Delta Z}\rho V_n U_0^2 \Delta z \Delta y} \qquad \text{(V2)}$$

where ΔZ is the blade span, ΔY is the blade pitch distance and Vn is the normal velocity as defined in Fig. 11. The density terms cancel due to an assumption of incompressible flow. Property values were calculated using a four point average.

The calculation produced a result of $\overline{\overline{q^2}}/U_0^2 = 0.137$ which can be compared to the value of $\overline{\overline{C_{pt}}} = 0.386$ calculated for the bottom half of the passage at X/c = 0.96 by Peters [6]. This result implies that 36% of the total pressure loss produced by X/c = 0.96 appears as turbulence kinetic energy (here it is assumed that the turbulence does not influence the measurement of total pressure loss). The isotropic assumption used for the

turbulence kinetic energy measured by the single wire probe had little effect on the overall calculation due to the small normal velocities found in the tip leakage jet.

V.B.3. Normal Stress Distributions

Figures 37, 38 and 39 show contour plots of the turbulent normal stresses $\overline{u^2}$, $\overline{v^2}$ and $\overline{w^2}$, respectively, normalized by U_0^2. These contours can be thought of as distributions of the turbulence energy in the coordinate directions since the sum of the three normal stresses is equal to $\overline{q^2}/U_0^2$.

The distribution of $\overline{u^2}/U_0^2$ shows a peak of about 0.35 in the region where the tip leakage jet separates from the bottom endwall and levels in the area of 0.15 - 0.25 around the vortex. This normal stress is about 0.05 at the core of the tip leakage vortex.

Lower levels of the normal stress $\overline{v^2}/U_0^2$ were found, with a peak value in the tip leakage jet separation region of about 0.37 and levels from 0.05 - 0.12 around the outside of the vortex. These values decay as the fluid proceeds around the vortex. This stress is also about 0.05 at the core of the tip leakage vortex.

Levels of the normal stress $\overline{w^2}/U_0^2$ were found to be significantly higher than the other two components in the entire tip leakage vortex region of the flow. Three large peak values were found. In the region where the tip leakage jet separates from the bottom endwall a peak value of about 0.41 was found. The highest value of 0.46 was found at a point just above the separation region. Another peak of about 0.43 was found at the top of the vortex in the region where the tip leakage vortex begins to interact with the passage vortex. These results indicate that significant energy is contained in the fluctuation in the Z direction. In the region where the tip leakage jet separates, this result is physically easy to visualize since the flow is changing direction sharply from a flow in the Y direction to a

flow in the X and Z directions. In the region across the top of the tip leakage vortex there is a varying degree of interaction with the passage vortex. The high values of normal stress in the Z direction can be visualized as stress generated as the flow tries to push upward (in the Z direction). Nearest the passage vortex the stresses become particularly large as if due to an increased resistance.

Around the tip leakage vortex, the levels of normal stress in the three coordinate directions are of quite different magnitude, thus it appears that the turbulence in the vortex is non-isotropic. In the region where the tip leakage vortex separates from the bottom endwall, values of the three normal stresses are of very similar magnitude. With this in mind as well as the fact that the measurements of turbulence kinetic energy with the single wire probe (based on an isotropic assumption) appear continuous with the x-wire probe measurements in the separation region, it appears that the tip leakage jet up to the point of separation could satisfy an isotropic assumption.

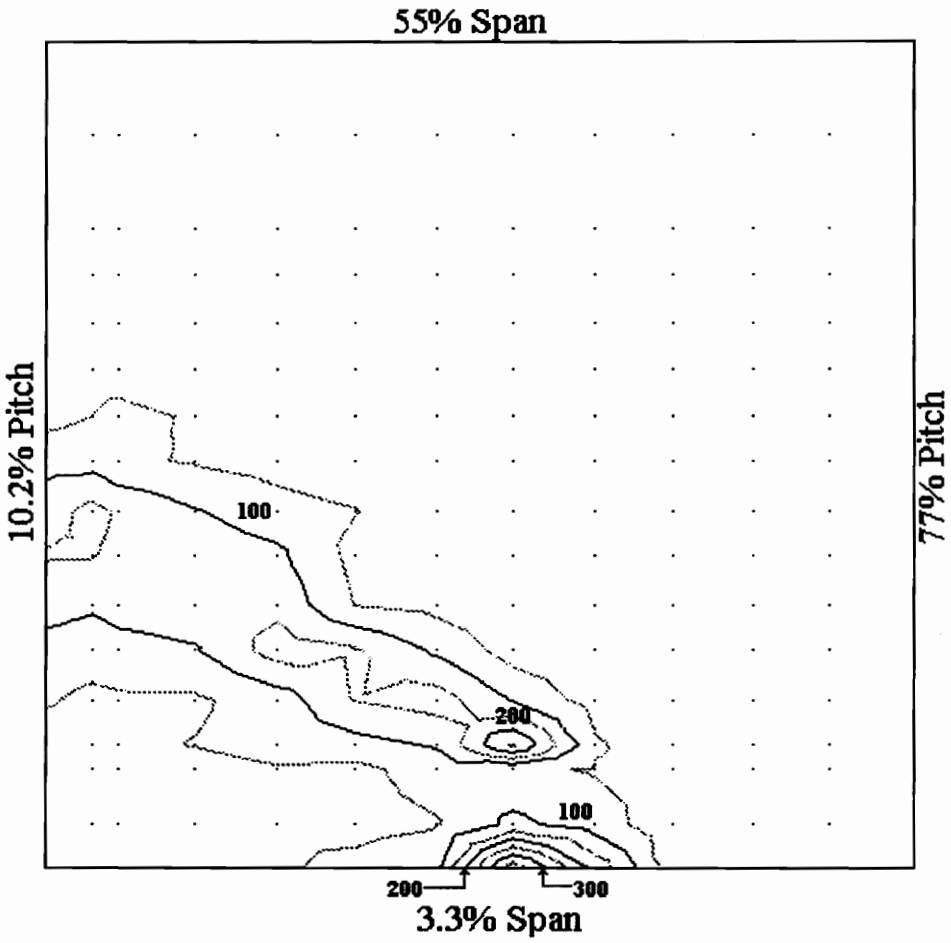

Figure 37. Contours of Normal Stress, $\frac{\overline{u^2}}{U_0^2}$*1000

Measurement Plane at X/c = 0.96

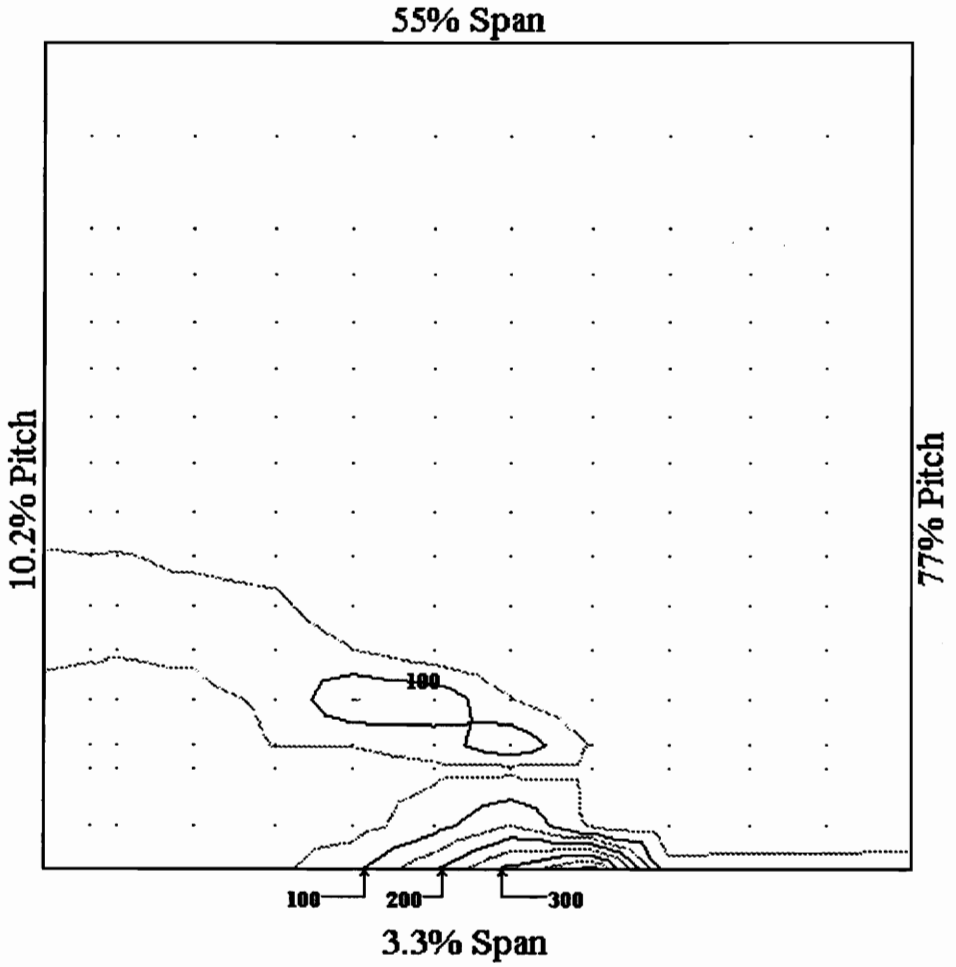

Figure 38. Contours of Normal Stress, $\frac{\overline{v^2}}{U_0^2} * 1000$

Measurement Plane at X/c = 0.96

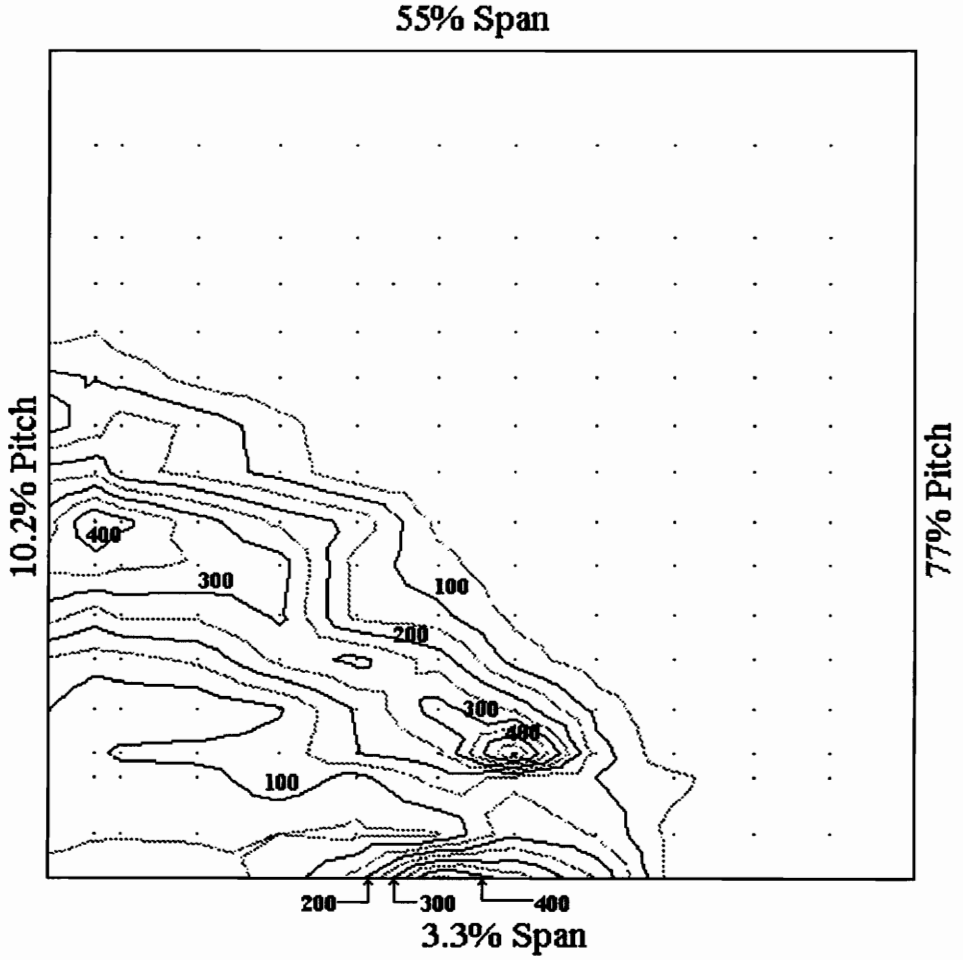

Figure 39. Contours of Normal Stress, $\frac{\overline{w^2}}{U_0^2} * 1000$

Measurement Plane at X/c = 0.96

V.B.4. Shear Stress Distributions

Contour plots of the turbulent shear stresses $\overline{uv}$, $\overline{uw}$ and $\overline{vw}$ non-dimensionalized by U_0^2 are given in Figures 40, 41 and 42 respectively.

The contours of $\overline{uv}/U_0^2$ show a peak value near the tip leakage jet separation of about 0.23. The distribution across the top of the vortex is positive with typical values in the 0.05 - 0.10 range. Values in the vortex core are generally less than 0.01.

The peak value of the shear stress $\overline{uw}/U_0^2$ is also found near the separation of the tip leakage jet and has a value of about -0.42. The distribution across the top of the tip leakage vortex is negative with typical magnitudes of -0.16 to -0.20. In the core of the vortex the magnitude is about -0.05.

The shear stress $\overline{vw}/U_0^2$ also has a peak value near the separation with a magnitude of about -0.40. Typical values across the top of the vortex are negative with a relatively small magnitude, typically -0.05 to -0.11. Near the core of the vortex the magnitude is less than -0.01.

The turbulent shear stress distributions again indicate larger stresses in the spanwise direction. This is consistent with the normal stress distributions. The $\overline{uw}/U_0^2$ shear stress is significantly larger than the other shear stresses in the region above the tip leakage vortex.

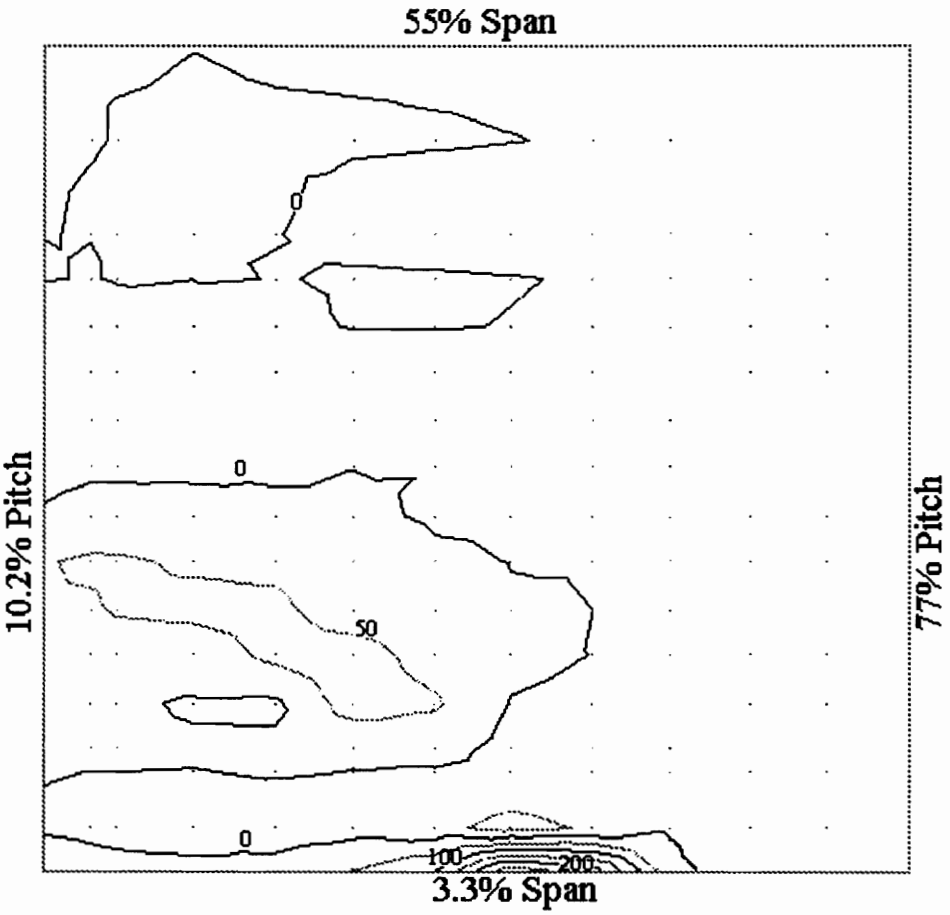

Figure 40. Contours of $\frac{\overline{uv}}{U_0^2} * 1000$

Measurement Plane at X/c = 0.96

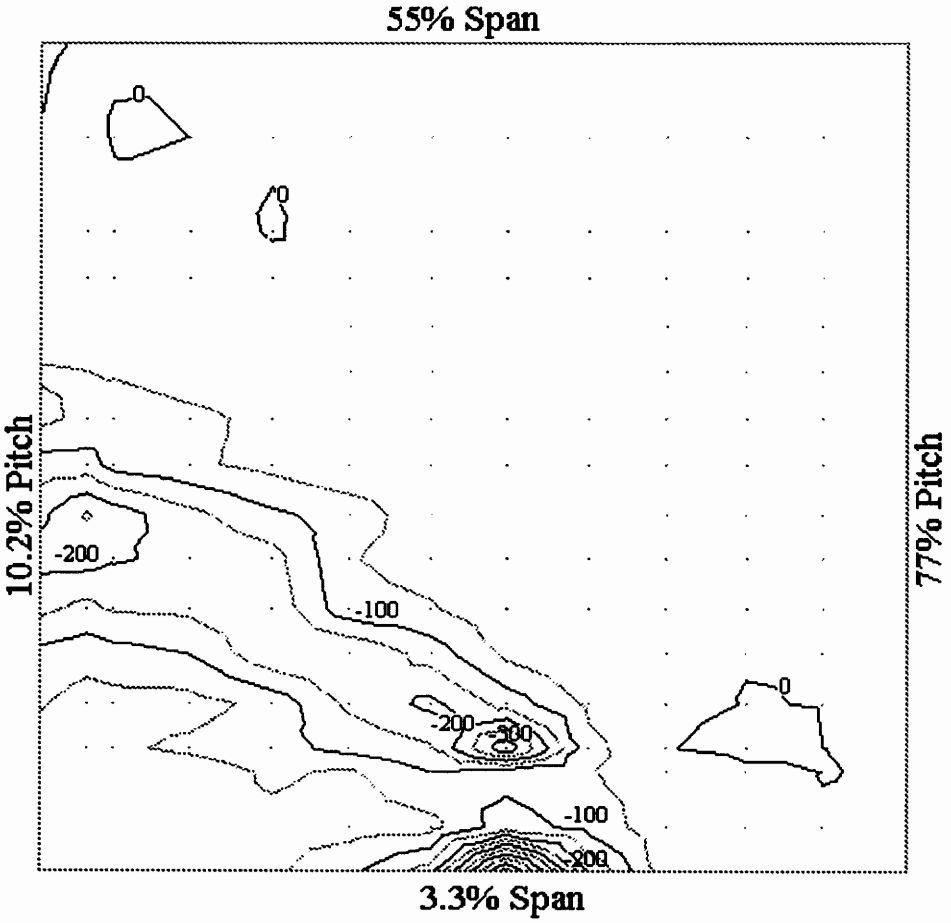

Figure 41. Contours of $\frac{\overline{uw}}{U_0^2} * 1000$

Measurement Plane at X/c = 0.96

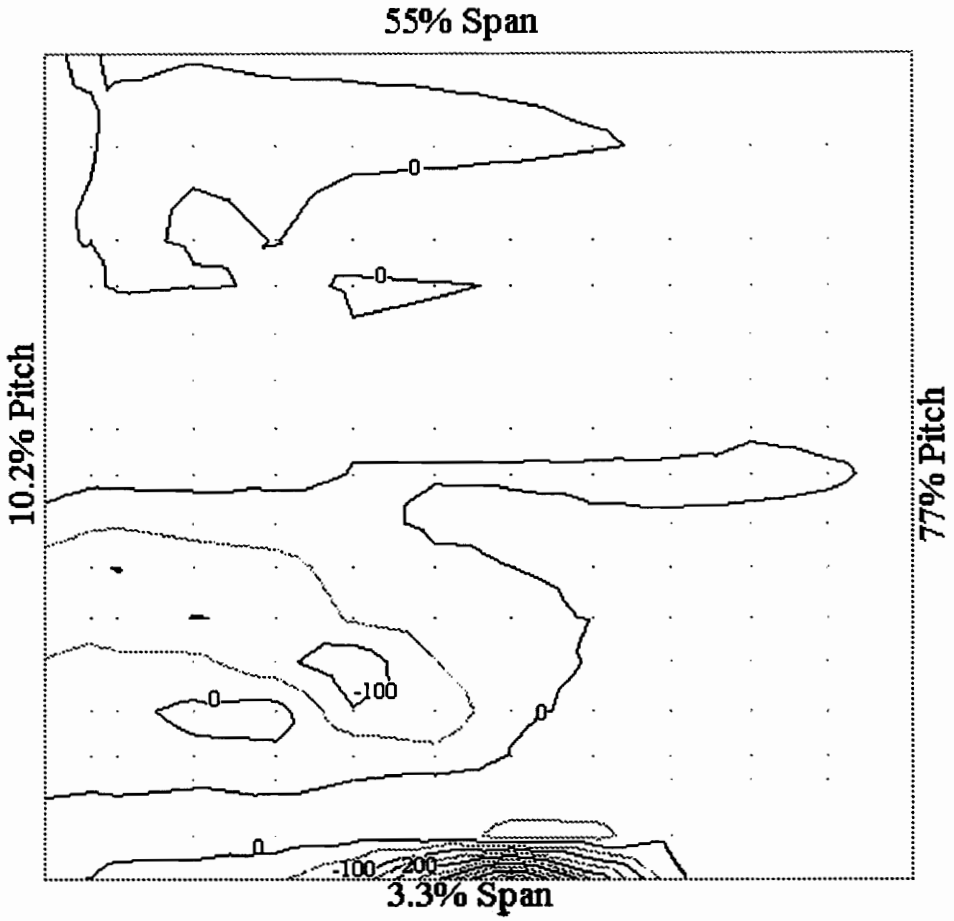

Figure 42. Contours of $\frac{\overline{vw}}{U_0^2} * 1000$

Measurement Plane at X/c = 0.96

V.B.5. Turbulent Deformation Work

Having distributions of all six components of the Reynolds stresses, as well as mean velocities U(Y,Z), V(Y,Z) and W(Y,Z) and knowing from continuity that:

$$\frac{\partial U}{\partial x} = -\frac{\partial V}{\partial y} - \frac{\partial W}{\partial z}$$

(V3)

the stresses can be combined with the velocity gradients to calculate a turbulence production or work-deformation term which can be directly related to total pressure losses. From Moore, Shaffer and Moore [1] in Cartesian tensor notation:

$$-\frac{\partial}{\partial\left(\frac{X}{c}\right)}\left(\overline{\overline{C_{Pt}}}\right) \cong N\iint_A \rho\,\overline{u_i u_j}\frac{\partial U_i}{\partial x_j}dA + N\iint_A -\mu\left(\frac{\partial U_i}{\partial x_j}+\frac{\partial U_j}{\partial x_i}\right)\frac{\partial U_i}{\partial x_j}dA \qquad \text{(V4)}$$

where:

X/c = the distance downstream of the blade leading edge divided by the chord length

$\overline{\overline{C_{Pt}}}$ = The mass averaged total pressure loss coefficient

N = non-dimensionalization factor: $N = \frac{c}{\frac{1}{2}\overline{V_n} A \rho U_0^2}$ where $\overline{V_n}$ is the area averaged normal velocity.

A= Flow Area, from 3.3% to 50% span in the Z-direction and from 10.2% to 77% pitch in the Y-direction

Here the first term on the right represents the turbulent contributions to the deformation work and the second term on the right represents the laminar contributions. With the data from this experiment seven terms of the turbulent deformation work can be calculated. These are: $\frac{\overline{uv}}{U_0^2}*\frac{\partial(U/U_0)}{\partial(x/c)}$, $\frac{\overline{uv}}{U_0^2}*\frac{\partial(U/U_0)}{\partial(y/c)}$, $\frac{\overline{v^2}}{U_0^2}*\frac{\partial(V/U_0)}{\partial(y/c)}$, $\frac{\overline{vw}}{U_0^2}*\frac{\partial(W/U_0)}{\partial(y/c)}$, $\frac{\overline{uw}}{U_0^2}*\frac{\partial(U/U_0)}{\partial(z/c)}$, $\frac{\overline{vw}}{U_0^2}*\frac{\partial(V/U_0)}{\partial(z/c)}$ and $\frac{\overline{w^2}}{U_0^2}*\frac{\partial(W/U_0)}{\partial(z/c)}$. These terms were calculated for the measurement plane at X/c = 0.96 and are contour plotted in figures 43 to 49.

When examining these plots it is important to remember that a negative sign indicates a contribution to the total pressure loss while a positive sign indicates a contribution to the total pressure gain. The $\overline{u_i v}\frac{\partial(U_i/U_0)}{\partial(y/c)}$ terms are all of very small magnitude except at the point where the tip leakage jet separates from the bottom endwall. The $\overline{u_i w}\frac{\partial(U_i/U_o)}{\partial(z/c)}$ are significantly larger with $\frac{\overline{uw}}{U_0^2}*\frac{\partial(U/U_0)}{\partial(z/c)}$ appearing to be the largest source of loss followed by $\frac{\overline{w^2}}{U_0^2}*\frac{\partial(W/U_0)}{\partial(z/c)}$ and $\frac{\overline{vw}}{U_0^2}*\frac{\partial(V/U_0)}{\partial(z/c)}$. These losses are located around the top of the vortex as well as a high concentration near the tip leakage jet separation which is as expected. The $\frac{\overline{vw}}{U_0^2}*\frac{\partial(V/U_0)}{\partial(z/c)}$ term seems evenly distributed between positive and negative. The $\frac{\overline{uv}}{U_0^2}*\frac{\partial(U/U_0)}{\partial(y/c)}$ is also significant in the endwall separation

region. Evaluating the area integral of the right side of equation (V4) including the laminar terms yielded the results summarized in Table 7.

Quantity	Calculated Value	Percentage of total integral
Total Laminar Terms	-0.001	0.03
$\frac{\overline{u^2}}{U_0^2} * \frac{\partial U}{\partial x}$	0.046	-13
$\frac{\overline{uv}}{U_0^2} * \frac{\partial U}{\partial y}$	0.0001	-.04
$\frac{\overline{v^2}}{U_0^2} * \frac{\partial V}{\partial y}$	-0.0016	0.44
$\frac{\overline{vw}}{U_0^2} * \frac{\partial W}{\partial y}$	-0.0008	0.23
$\frac{\overline{uw}}{U_0^2} * \frac{\partial U}{\partial z}$	-0.33	93
$\frac{\overline{vw}}{U_0^2} * \frac{\partial V}{\partial z}$	0.049	-14
$\frac{\overline{w^2}}{U_0^2} * \frac{\partial W}{\partial z}$	-0.12	33
Total Turbulent Terms	-0.357	99
Total	-0.36	100.00

Table 7. Contributions of Individual terms

to the Area Integral of Deformation Work

These results confirm that the main mechanism of loss in the tip leakage vortex is the conversion of mean kinetic energy into turbulence kinetic energy since the laminar terms only contribute about 0.03%. By far the largest contribution is due to the dissipation through the shear stress in the spanwise direction, $\frac{\overline{uw}}{U_0^2} * \frac{\partial (U/U_0)}{\partial (z/c)}$. The spanwise normal stress deformation work term $\frac{\overline{w^2}}{U_0^2} * \frac{\partial (W/U_0)}{\partial (z/c)}$ is also significant. The term $\frac{\overline{u^2}}{U_0^2} * \frac{\partial (U/U_0)}{\partial (x/c)}$, having a positive sign is a possible indication of the conversion of turbulence kinetic energy to primary mean kinetic energy. The $\frac{\overline{vw}}{U_0^2} * \frac{\partial (V/U_0)}{\partial (z/c)}$ also having positive sign suggests another possible mechanism for the conversion of energy from spanwise turbulence kinetic energy into mean kinetic energy.

Figure 50 shows contours of the sum of all the turbulent terms. The highest overall turbulent deformation losses can be found along the top of the tip leakage vortex with typical values of -0.06. Another region of high loss is at the separation near the bottom endwall. A small region of gains is found between the endwall separation and the top of the tip leakage vortex. In the vortex core there is little loss production.

The left hand side of Eq. V4 can be approximated by using the values of $\overline{\overline{C_{Pt}}}$ calculated by Peters at X/c = 0.96 and Dishart at X/c = 1.4 based on the bottom half flow area:

$$-\frac{\partial}{\partial\left(\frac{X}{c}\right)}\left(\overline{\overline{C_{Pt}}}\right) \cong -\frac{\overline{\overline{C_{Pt,1.40}}} - \overline{\overline{C_{Pt,0.96}}}}{1.40 - 0.96} = -\frac{0.558 - 0.386}{0.44} = -0.391 \qquad \text{(V5)}$$

By comparing the result calculated from an area integral of the right hand side of Eq. V4 to the value above, it can be seen that the right hand side is 91% of the value from Eq. V5. This is in very good agreement considering the approximation used in Eq. V5.

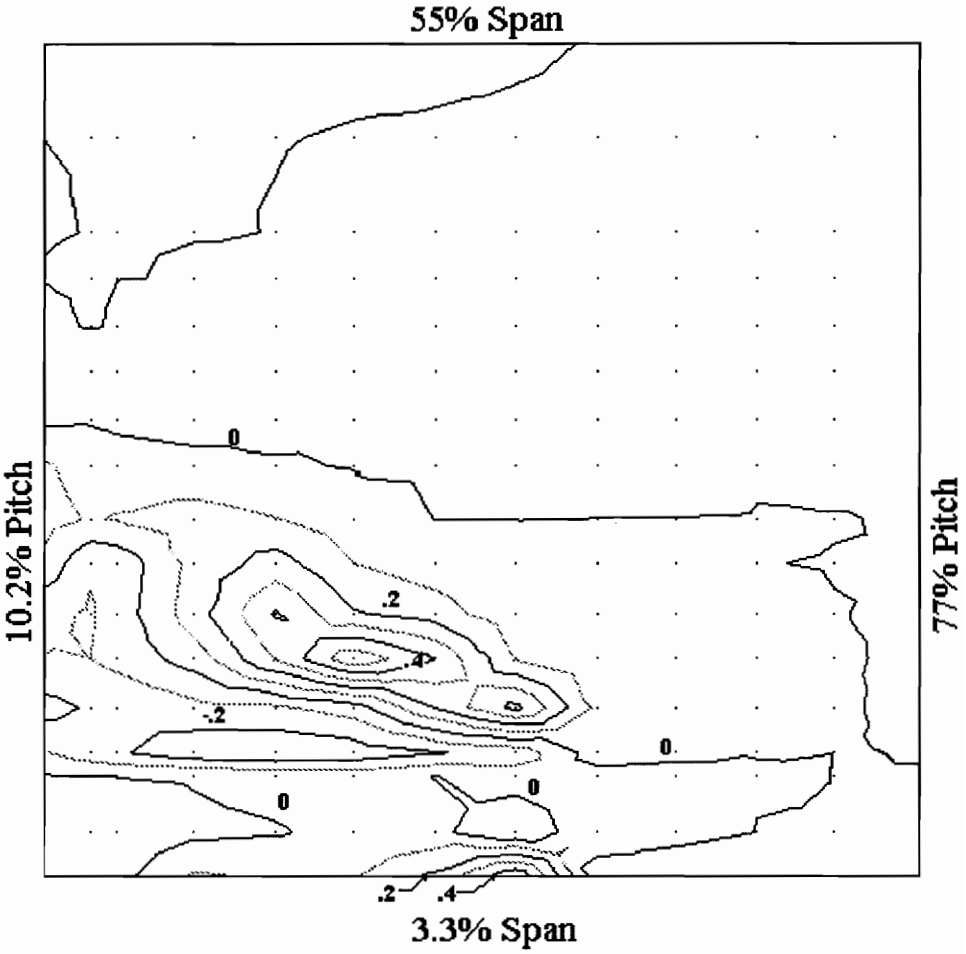

Figure 43. Contours of $\frac{\overline{u^2}}{U_0^2} * \frac{\partial(U/U_0)}{\partial(X/c)}$

Measurement Plane at X/c = 0.96

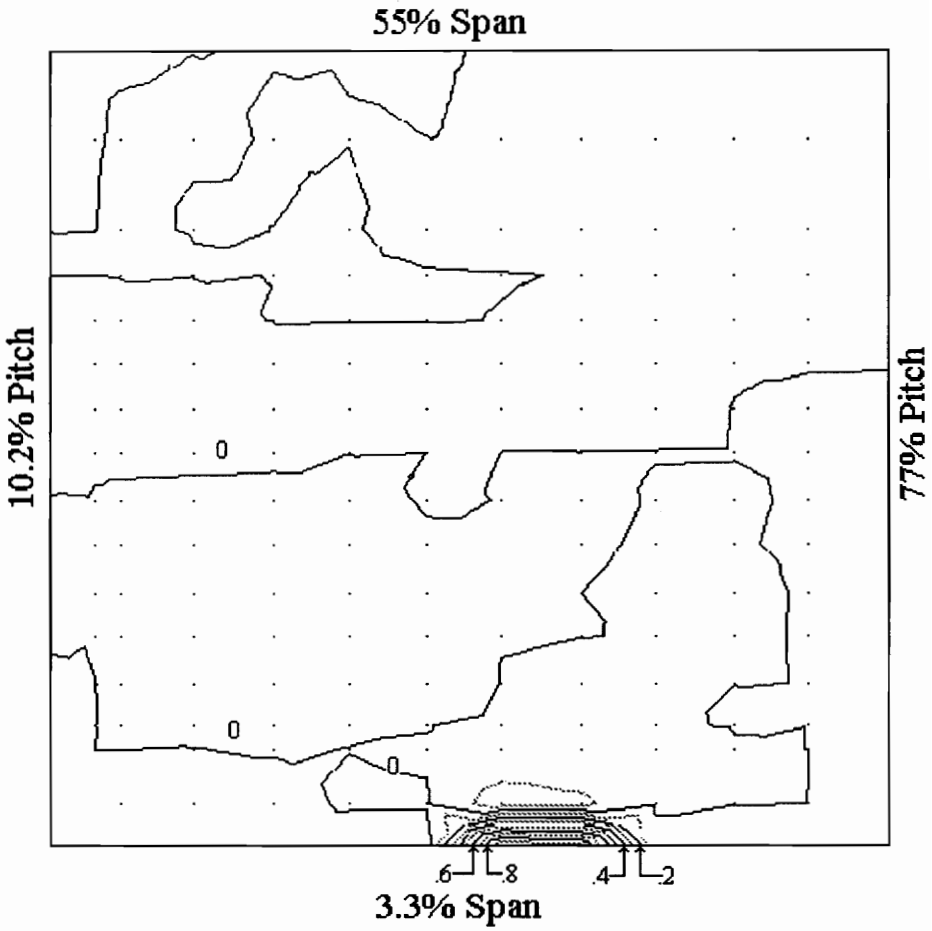

Figure 44. Contours of $\frac{\overline{uv}}{U_0^2} * \frac{\partial\left(U/U_0\right)}{\partial\left(y/c\right)}$

Measurement Plane at X/c = 0.96

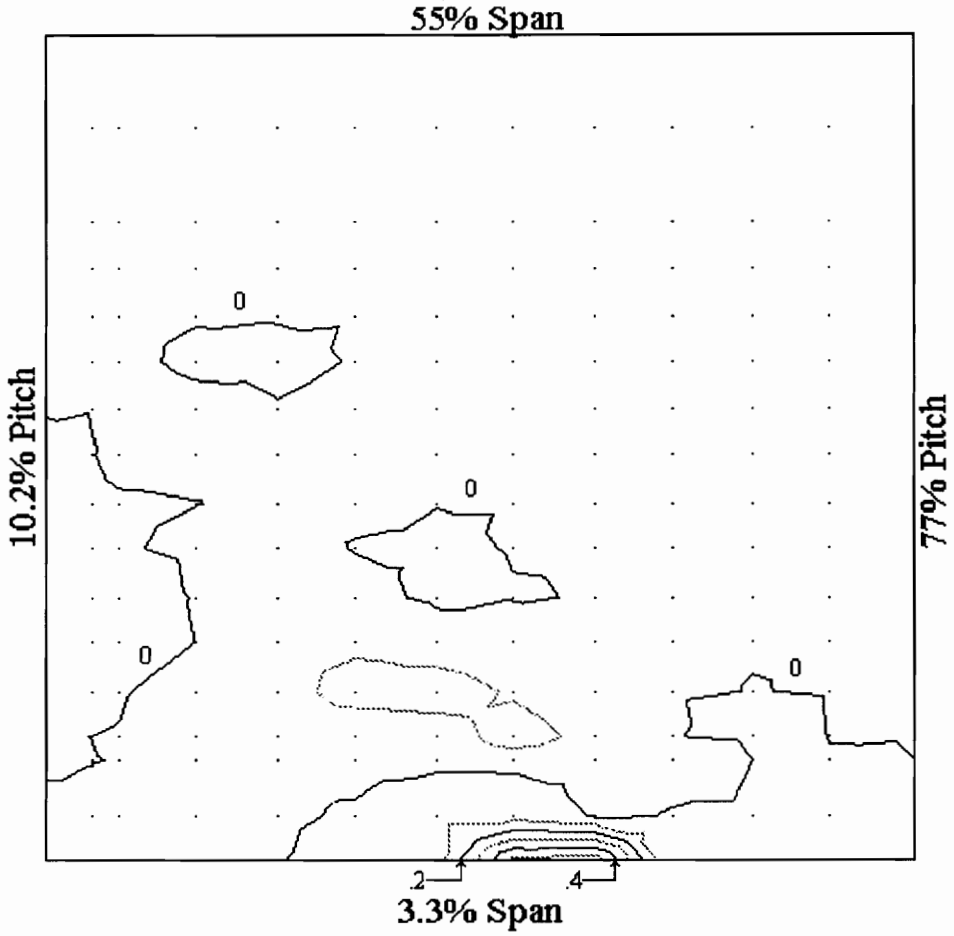

Figure 45. Contours of $\frac{\overline{v^2}}{U_0^2} * \frac{\partial\left(V/U_0\right)}{\partial\left(y/c\right)}$

Measurement Plane at X/c = 0.96

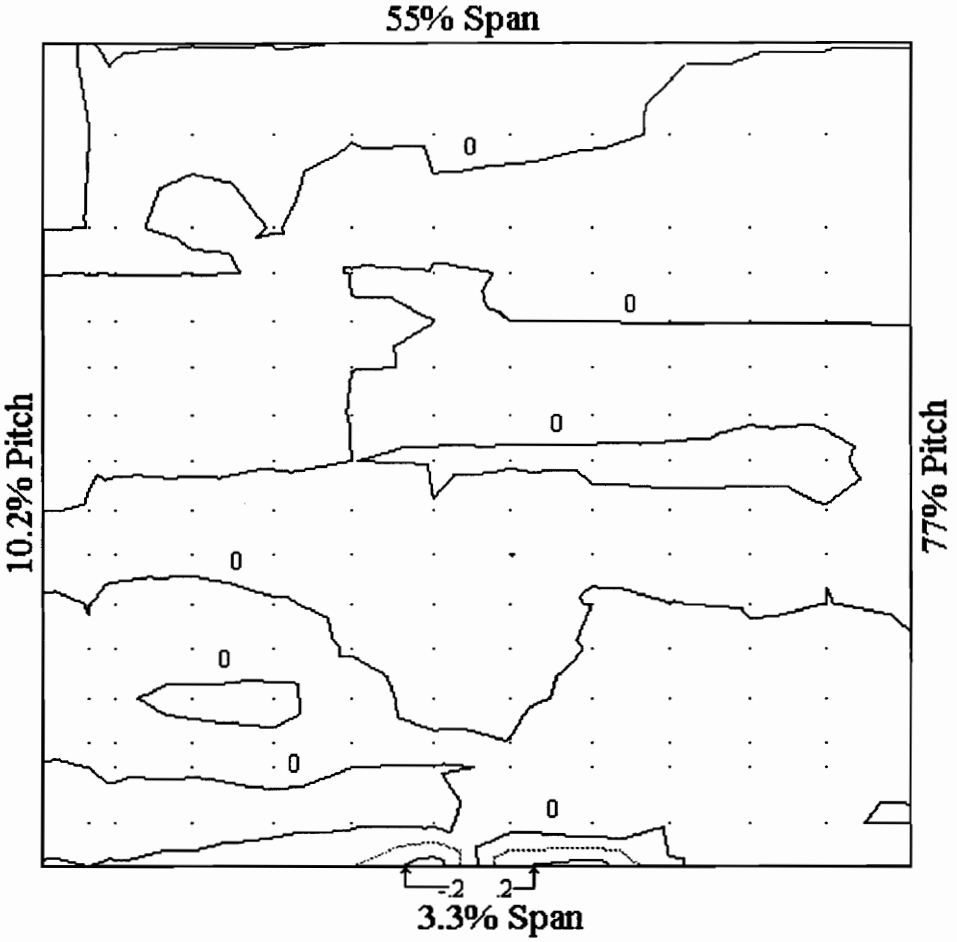

Figure 46. Contours of $\frac{\overline{vw}}{U_0^2} * \frac{\partial\left(W/U_0\right)}{\partial\left(y/c\right)}$

Measurement Plane at X/c = 0.96

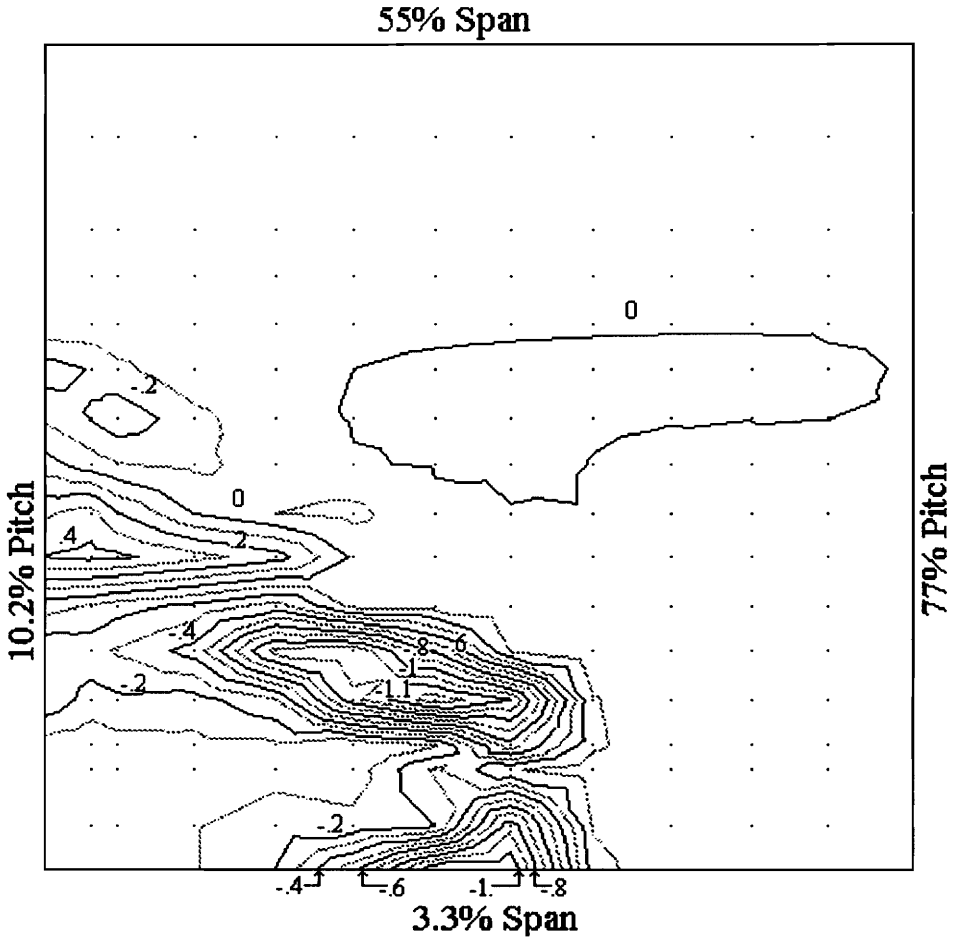

Figure 47. Contours of $\frac{\overline{uw}}{U_0^2} * \frac{\partial\left(U/U_0\right)}{\partial\left(z/c\right)}$

Measurement Plane at X/c = 0.96

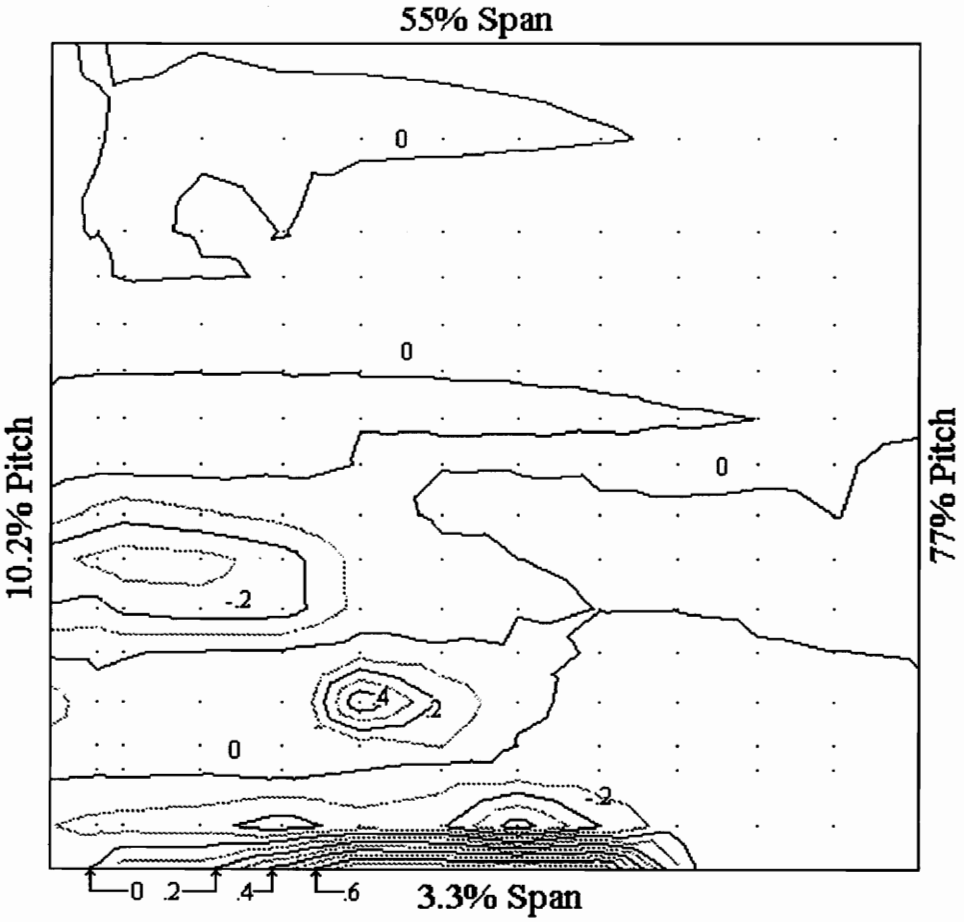

Figure 48. Contours of $\frac{\overline{vw}}{U_0^2} * \frac{\partial\left(V/U_0\right)}{\partial\left(z/c\right)}$

Measurement Plane at X/c = 0.96

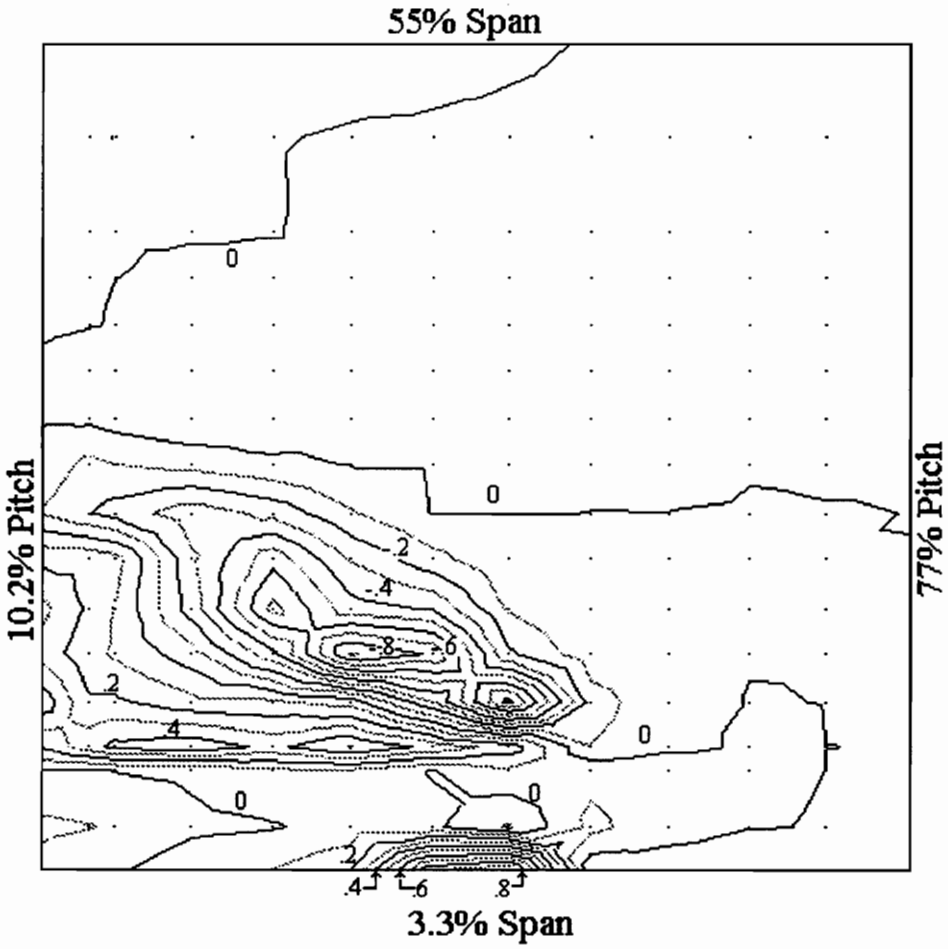

Figure 49. Contours of $\frac{\overline{w^2}}{U_0^2} * \frac{\partial\left(W/U_0\right)}{\partial\left(z/c\right)}$

Measurement Plane at X/c = 0.96

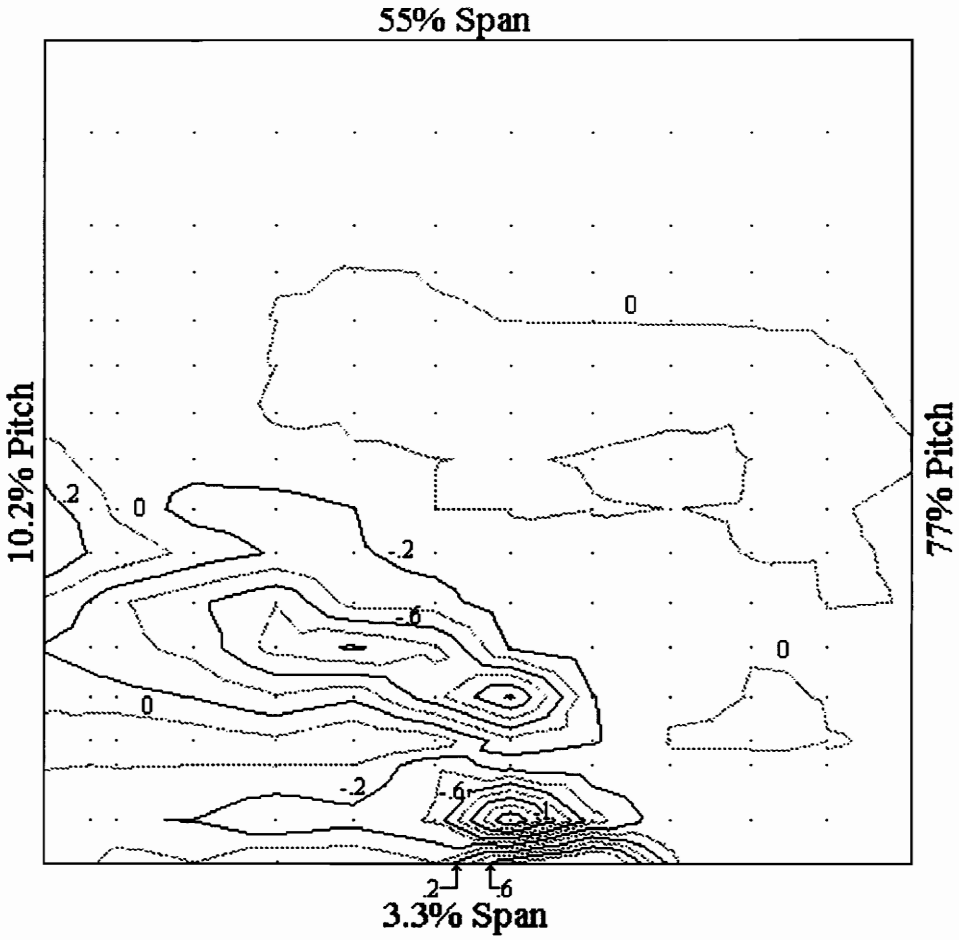

Figure 50. Contours of Total Turbulent Deformation Work

Chapter VI
Conclusions

A rotatable x-wire hot wire probe was developed and used to measure turbulent (Reynolds) stresses in a linear turbine cascade with a tip gap of 2.1% of the blade span. Measurements were performed in the tip leakage vortex at a plane located 0.96 axial chord lengths downstream of the blade leading edge in order to study the contribution of turbulence to the losses in the blade row.

The rotatable x-wire probe was developed to measure all of the components of the turbulent stresses and the mean velocity components. This probe was rotated about its axis to six angular settings allowing redundant data to be taken for least squares fitting. This probe was smaller than the probe used by previous investigators allowing greater spatial resolution.

A data acquisition and probe movement control system was constructed to enable a large amount of data to be taken accurately and in a relatively short time. The hot wire signals were digitally sampled, eliminating the need for an analog correlator. The probe movement control system automated movement of the probe from grid point to grid point as well as rotating the probe about its axis at each grid point. The combination of these two systems allowed fully automated experimentation which minimized the possibility of human error.

VI.A. Verification in Fully Developed Pipe Flow

In order to verify that the probe, data aquisition system and analysis software was able to produce reliable turbulent stress measurements, verification tests were performed at the exit of a pipe at a Reynolds number of 120,000. The pipe had a length of 240 pipe diameters to insure fully developed flow. The results were compared with those of Laufer [9], Lawn[10] and Shaffer [3].

VI.A.1. Zero Probe Yaw Angle

1.) Using a sampling rate of 20,000 Hz and six angular settings 60° apart, the mean velocity distribution across the pipe was within 2.6% of Laufer's results. The maximum flow angle that was measured was 0.85°. This flow angle should be zero since the pipe flow is purely axial.

2.) The turbulent normal stress distribution was measured to within 7.5%, 12.3% and 8.8% of Lawn's results for $\sqrt{\overline{u^2}}\,/\,U_\tau$, $\sqrt{\overline{v^2}}\,/\,U_\tau$ *and* $\sqrt{\overline{w^2}}\,/\,U_\tau$ respectively. The resulting turbulence kinetic energy distribution had an average difference of 0.4%. The turbulent shear stress, $\overline{uv}/U_\tau^2$, was measured to within 19.6% of Laufer's results. These results are very close to those obtained by Shaffer [3].

VI.A.2. Varying Probe Yaw Angle

The probe was also tested in pipe flow at various yaw angles with six equally spaced angular settings to determine the useful range of the probe.

1.) At yaw angles of 0, 10, 20 and 30 degrees the mean velocity was found to be within 0.5% of Laufer's data. The turbulent normal stresses were within 11.2% and the turbulence kinetic energy was within 8.9% of Lawn's data. The turbulent shear stresses were within 21% of Laufer's theoretical curve. At a yaw angle of 40 degrees the discrepancies between the measured results and Laufer's and Lawn's results became much greater, indicating a cone of probe usefulness of 30 degrees.

2.) A technique which discarded settings where prong interference became evident was tested for flow angles up to 45 degrees, with results comparable to the zero incidence angle results.

VI.B. Tip Leakage Vortex Measurements

Turbulence measurements were performed in a large scale linear turbine cascade geometrically similar to that used by Langston, et al. [2]. The flow is dominated by the presence of a tip leakage vortex. The data grid used for this study concentrated on the area in and around the tip leakage vortex.

1.) The mean velocity distribution agreed with that measured by Peters [6] with a five hole probe to within 3%. Secondary velocities agreed to within 8%. Velocities were accurately measured for cone angles up to 45 degrees.

2.) The tip leakage vortex core was found to be centered at $Y/\Delta Y = 0.28$, $Z/\Delta Z = 0.095$ which is slightly higher than the results of Peters.

3.) Turbulence intensities were found to be very high in the tip gap and in the tip leakage jet, with a peak RMS turbulence intensity of approximately 63% in the region where the tip leakage jet separates from the bottom endwall.

4.) The high turbulence flow issuing from the tip gap convects around the outside of the tip leakage vortex. The turbulence intensity in the core of the tip leakage vortex is relatively low with typical RMS turbulence intensities of about 20%.

5.) Low turbulence intensities were found in regions away from the blades, the endwalls and the tip leakage and passage vortices with typical RMS turbulence intensities of 1.8 to 2.6%.

6.) Turbulent normal stress distributions showed a large $\overline{w^2}/U_o^2$ component, which was greater than the other two components by a factor of 2-3. All three components were of the same magnitude in the region where the tip leakage jet separated from the bottom endwall. This indicates a non-isotropic turbulence around the tip leakage vortex and an isotropic region in the tip leakage jet.

7.) Shear stress distributions showed a large $\overline{uw}/U_o^2$ component, about 2 - 4 times as large as the other two components except in the region where the tip leakage vortex separated, where all three components were of the same order.

8.) The turbulent stresses were generally consistent in sign with the local velocity gradients.

VI.B.1 Mass Averaged Turbulence Kinetic Energy

A mass average was performed over the flow area where measurements were taken. This included the tip leakage and passage vortices as well as most of the plane from the bottom endwall to midspan at X/c = 0.96.

1.) The mass averaged value of turbulence kinetic energy was $\overline{\overline{q^2}}/U_o^2 = 0.14$. This accounts for 36% of the total pressure loss in the bottom half of the cascade at X/c = 0.96.

2.) The isotropic assumption made for the single wire measurements near the bottom endwall had little effect since the normal velocities were small in this region.

3.) These results seem to indicate that a major mechanism in the generation of total pressure losses in the tip leakage vortex region is the viscous dissipation of a high level of turbulence.

VI.B.2 Turbulent Deformation Work

The principal mechanism for the generation of total pressure losses is the work of deformation of the mean flow by the turbulent stresses. The area integral of these work deformation terms was evaluated over the flow area paying particular attention to the individual components.

1.) The total area integral of the deformation work (both laminar and turbulent components) was calculated to be -0.357 compared to a value estimated from Dishart's and Peters' data of -0.391.

2.) The turbulent components of deformation work were the dominant contributors with the laminar terms contributing less than 0.1%.

3.) The $\frac{\overline{uw}}{U_o^2}\cdot\frac{\partial U}{\partial z}$ term contributed 93% of the total and the $\frac{\overline{w^2}}{U_o^2}\cdot\frac{\partial W}{\partial z}$ term contributed 33% indicating strong dissipation due to veloctiy gradients in the z direction. This is consistent with the large z-oriented turbulent stresses.

4.) The $\frac{\overline{u^2}}{U_o^2}\cdot\frac{\partial U}{\partial x}$ term contributed -13% and the $\frac{\overline{vw}}{U_o^2}\cdot\frac{\partial V}{\partial z}$ term contributed -14% of the area integral of the deformation work. The negative sign signifies a gain in the mean kinetic energy of the fluid.

VI.C. Tip Gap Exit Measurements

A traverse was made at the exit plane of the tip gap with the single wire endwall probe. Calculations of turbulence kinetic energy were made assuming isotropic turbulence.

1.) The measured normal velocity distribution at X/c = 0.96 was consistent with that measured by Dishart [5].

2.) The turbulence kinetic energy distribution confirms the tip gap flow model of Tilton [4]. The turbulence distribution near the bottom endwall resembles that of a turbulent boundary layer on a flat plate. About one-third of the way across the tip gap, locally low values of turbulence kinetic energy were found. This is consistent with Tilton's model where this region would contain free stream flow. From a height of about one-half of the tip gap to the blade tip a region of high turbulence was found. This is consistent with Tilton's model since this region should be flow which separated at the inlet of the tip gap.

References

1) Moore, J., Shaffer, D.M., and Moore, J.G., "Reynolds Stresses and Dissipation Mechanisms Downstream of a Turbine Cascade," Trans. ASME, Journal of Turbomachinery, Vol. 109, pp. 258-267, April 1987.

2) Langston, L.S., Nice, M.L., and Hooper, R.M., "Three Dimensional Flow Within a Turbine Cascade Passage", Trans. ASME, Journal of Engineering for Power, Vol. 99, pp. 21-28, January 1977.

3) Shaffer, D.M., "Reynolds Stress Measurements Downstream of a Turbine Cascade", M.S. Thesis, Virginia Polytechnic Institute and State University, August 1985.

4) Moore, J., and Tilton, J.S., "Tip Leakage Flow in a Linear Turbine Cascade," Trans. ASME, Journal of Turbomachinery, Vol. 110, pp. 18-26, January 1988.

5) Dishart, P.T., and Moore, J., "Tip Leakage Losses in a Linear Turbine Cascade," Trans. ASME, Journal of Turbomachinery, Vol. 112, No. 4, pp. 559-608, Oct. 1990.

6) Peters, D.W., "Tip Leakage Loss Developement in a Linear Turbine Cascade", M.S. Thesis, Virginia Polytechnic Institute and State University, January 1992.

7) Gorton, C.A. and Lakshminarayana, B., "Analytical and Experimental of Mean Flow and Turbulence Characteristics Inside the Passages of an Axial Flow Inducer," NASA Contractor Report 3333, November 1980.

8) Lakshminarayana, B., "Three Sensor Hot Wire/Film Technique for Three Dimensional Mean and Turbulence Flow Field Measurement," TSI Quarterly, Volume VIII, Issue 1, pp 3-13, Jan-Mar 1982.

9) Laufer, J., "The Structure of Turbulence in Fully Developed Pipe Flow," NACA Report No. 1174, 1954.

10) Lawn, C.J., "The Determination of the Rate of Dissipation in Turbulent Pipe Flow," Journal of Fluid Mechanics, Vol. 48, part 3, pp 477-505, 1971.

Appendix A

Shear Stress In Fully Developed Pipe Flow

A.1. Calculation of Shear Velocity

For fully developed ,steady, incompressible flow in a pipe, with no radial pressure gradient, a control volume can be drawn as shown in Figure A1. Assuming that the axial pressure gradient and shear stress at the wall is constant, a summation of forces in the axial direction yields:

$$P(\pi a^2) - (P + \Delta P)(\pi a^2) + \tau_0(2\pi a\ L) = 0 \qquad \text{(A1)}$$

where ΔP is the static pressure drop along a length, L, of the pipe and a is the radius of the pipe. Solving for the shear stress at the wall :

$$\tau_0 = \frac{a\Delta P}{2L} \qquad \text{(A2)}$$

Finally the shear velocity can be calculated as:

$$U_\tau = \sqrt{\frac{\tau_0}{\rho}} = \sqrt{\frac{a\Delta P}{2\rho L}} \qquad \text{(A3)}$$

where the density, ρ, and the pressure drop along the pipe are measured during testing.

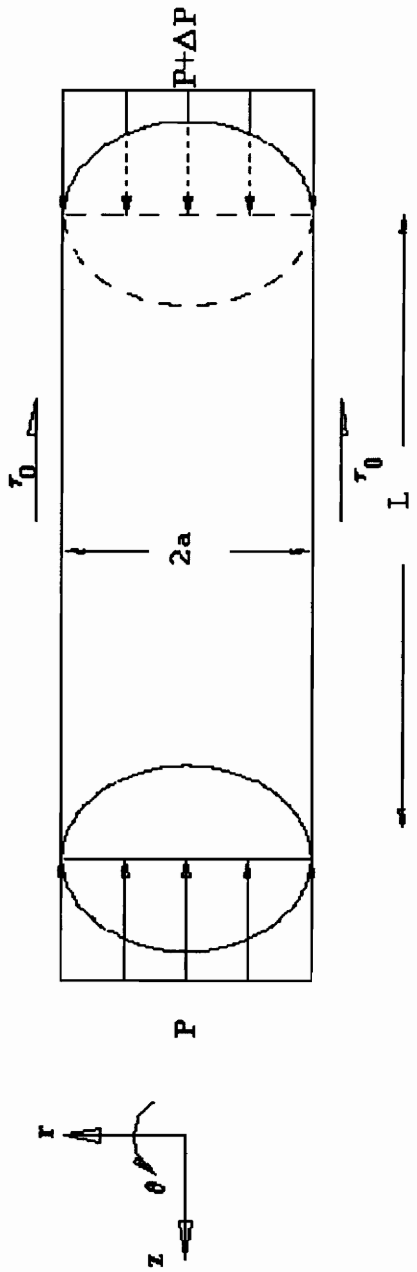

Figure A1. Control Volume For Fully Developed Pipe Flow

A.2. Radial Shear Stress Distribution

In fully developed, steady, incompressible flow in a pipe a force balance taken on a differential annulus results in:

$$\frac{\partial}{\partial r}(r\tau_{RZ}) = r\frac{\partial P}{\partial Z} \tag{A4}$$

Assuming a constant radial pressure gradient:

$$\frac{\partial P}{\partial Z} = -\frac{\Delta P}{L}. \tag{A5}$$

Then by integrating (A4) from the centerline (r = 0) to a radius r:

$$\tau(r) = -\frac{r\Delta P}{2L} \tag{A6}$$

dividing this by the result at r = a ($\tau_{rz}(a) = -\tau_0$) yields:

$$\frac{\tau_{rz}(r)}{\tau_0} = -\frac{r}{a}. \tag{A7}$$

Expanding the shear stress, τ_{rz}, into laminar and turbulent components:

$$\tau_{rz} = \mu \frac{\partial U_z}{\partial r} - \rho \overline{u_r u_z} \cong -\rho \overline{u_r u_z} \qquad \text{(A8)}$$

since the laminar shear stress is negligible compared to the turbulent shear stress except near the wall. By substituting (A8) into (A7) and since $U_\tau^2 = \tau_0/\rho$:

$$\frac{\overline{u_r u_z}}{U_\tau^2} = \frac{r}{a}. \qquad \text{(A9)}$$

This relation gives a linear variation of $\frac{\overline{u_r u_z}}{U_\tau^2}$ in the radial direction from r = a to r = -a.

Appendix B
Hot Wire Calibration Procedure

The following method was used to experimentally determine the calibration constants **a** and $\mathbf{k^2}$. The modified form of the cosine law used was:

$$E^a = Q_0(\cos^2\Phi + k^2\sin^2\Phi) \tag{B1}$$

where E is the wire voltage, Q_0 is the magnitude of the velocity, Φ is the wire yaw angle and **a** and $\mathbf{k^2}$ are the calibration constants to be determined. The factor **a** is used to account for the deviation from linearity when the velocity is varied. This can also be done by improved linearization. The $\mathbf{k^2}$ factor is used to account for the deviation from the cosine law when the velocity is held constant and the incidence angle is varied.

B.1. Determination of **a**

The determination of **a** was performed by placing the wire normal to the flow at the exit of the calibration pipe and varying the exit velocity. When the wire is normal to the flow (Φ=0) Equation (B1) reduces to:

$$E^a = Q_0 \tag{B2}$$

where Q_0 varies with the exit velocity, which is measured indirectly through a correlation between the upstream static pressure and the exit velocity. This correlation for Q_0 was:

$$Q_0 = 4.21\sqrt{\Delta P} \tag{B3}$$

where ΔP is the static pressure 5.9 meters upstream of the pipe exit expressed in mm H_20 scale of a micro manometer. Thus a set of readings in the form of $E_i^a = Q_0$ was obtained. This set of equations can be written as:

$$\left(\frac{E_i}{E_1}\right)^a = \frac{Q_i}{Q_1} \tag{B4}$$

where the subscript 1 refers to the reference position which is the maximum flow rate where E_1 was set to one volt. Taking the natural logarithm of both sides of Equation (B4) yields:

$$a \ln\left(\frac{E_i}{E_1}\right) = \ln\left(\frac{Q_i}{Q_1}\right). \tag{B5}$$

The calibration constant a is determined by minimizing the sum of the squares of the errors:

$$S = \sum_i \left[a \ln\left(\frac{E_i}{E_1}\right) - \ln\left(\frac{Q_i}{Q_1}\right)\right]^2. \tag{B6}$$

Taking the derivative with respect to a and setting equal to zero yields:

$$2\sum_i \left[a \ln\left(\frac{E_i}{E_1}\right) - \ln\left(\frac{Q_i}{Q_1}\right)\right] \ln\left(\frac{E_i}{E_1}\right) = 0. \tag{B7}$$

Solving for a:

$$a = \frac{\sum_i \left[\ln\left(\frac{Q_i}{Q_1}\right) * \ln\left(\frac{E_i}{E_1}\right)\right]}{\sum_i \left[\ln\left(\frac{E_i}{E_1}\right)\right]^2} \tag{B8}$$

B.2.) k^2 determination

To determine the calibration constant $\mathbf{k^2}$, the flow rate was kept constant at the maximum value and the wire yaw angle, Φ, was varied from 0° to 70°. From this, a set of equations for E_i as a function of Φ, was obtained:

$$E_i^a = Q_o\sqrt{\cos^2\Phi_i + k^2\sin^2\Phi_i} \tag{B9}$$

The wire voltage was set to one volt when Φ=0, resulting in Q_0 =1.

$$E_i^{2a} = \cos^2\Phi_i + k^2\sin^2\Phi_i \tag{B10}$$

Then, minimizing the sum of the squares of the errors in E^{2a} as before:

$$S = \sum_i \left(E_i^{2a} - \cos^2\Phi_i - k^2\sin^2\Phi_i\right)^2 \tag{B11}$$

taking the derivative with respect to Φ and setting equal to zero yields:

$$k^2 = \frac{\sum_i E_i^{2a}\sin^2\Phi_i - \sum_i \cos^2\Phi_i\sin^2\Phi_i}{\sum_i \sin^4\Phi_i} \quad . \tag{B12}$$

B.3.) Calibration Curves

A calibration curve of the rotatable x-wire probe is shown in Fig. B1. Here it can be seen that the linearity constants for wires A and B are very close to unity (1.009 and 1.013 respectively) indicating that the linearizer output is very close to being linear.

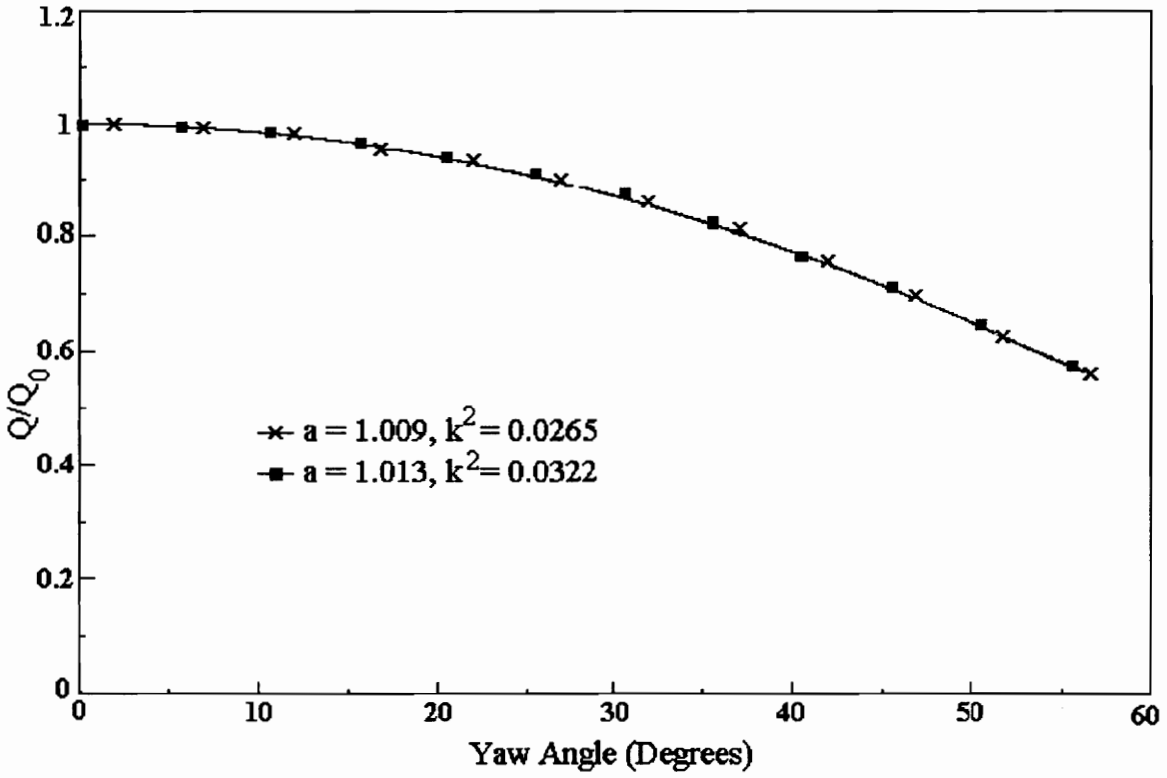

Figure B1. Calibration Curve for Rotatable X-Wire Probe

Appendix C
Calculation of Mean Velocity Components

The determination of the mean velocity components at a point is accomplished through the use of a mean square fitting. The accuracy of the results is strengthened with an increased number of probe angular settings. An effective cooling velocity (Q) is calculated for each wire (i) at each angular probe setting (j) from the wire mean voltage (E):

$$Q_{ij} = E_{ij}^{a_i} \tag{C1}$$

where a is the calibration constant previously determined. The effective cooling velocity is related to the wire position through the modified cosine law:

$$Q_{ij} = Q_0 \sqrt{\cos^2\left(\Phi_{ij}\right) + k_i^2 \sin^2\left(\Phi_{ij}\right)} \tag{C2}$$

Where:

Q_0 = normalized velocity magnitude (normalized by Q_{ref})

Φ_{ij} = wire yaw angle

k_i^2 = calibration constant

For each wire orientation, the wire yaw angle can be expressed using the sine law for spherical trigonometry as:

$$\sin\Phi_{ij} = \cos\alpha_{0_{ij}} \cos\alpha_r \cos\left(\alpha_p + \alpha_{w_{ij}}\right) + \sin\alpha_r \sin\alpha_{0_{ij}} \tag{C3}$$

where α_0, α_w, α_r and α_p are defined in Figure C1. Here α_0, α_w, α_r and α_p are unknown. The wire angles $\alpha_{0,ij}$ and wire rotational positions, $\alpha_{w,ij}$ are known quantities which specify the wire orientation relative to the fixed coordinate frame.

The solution is performed by iterating on the flow angles α_r and α_p in the set of equations (C3), and solving for the value of Q_0 predicted by each orientation:

$$Q_{o_{ij}} = \frac{Q_{ij}}{\sqrt{\cos^2(\Phi_{ij}) + k_i^2 \sin^2(\Phi_{ij})}} \tag{C4}$$

a least squares fitting is then applied to the result of this by evaluating the sum of the squares of the errors in $Q_{0,ij}$:

$$S = \sum_{ij} \left(Q_{mean} - Q_{0_{ij}} \right)^2 \tag{C5}$$

where S is the sum of the errors and Q_{mean} is the average of the $Q_{0,ij}$'s. The iteration is performed until S is minimized.

Knowing Q_0, α_r and α_p, the mean velocity components can be calculated:

$$\begin{aligned} U &= Q_0 Q_{ref} \cos\alpha_r \cos\alpha_p \\ V &= -Q_0 Q_{ref} \cos\alpha_r \sin\alpha_p \\ W &= -Q_0 Q_{ref} \sin\alpha_r \end{aligned} \tag{C6}$$

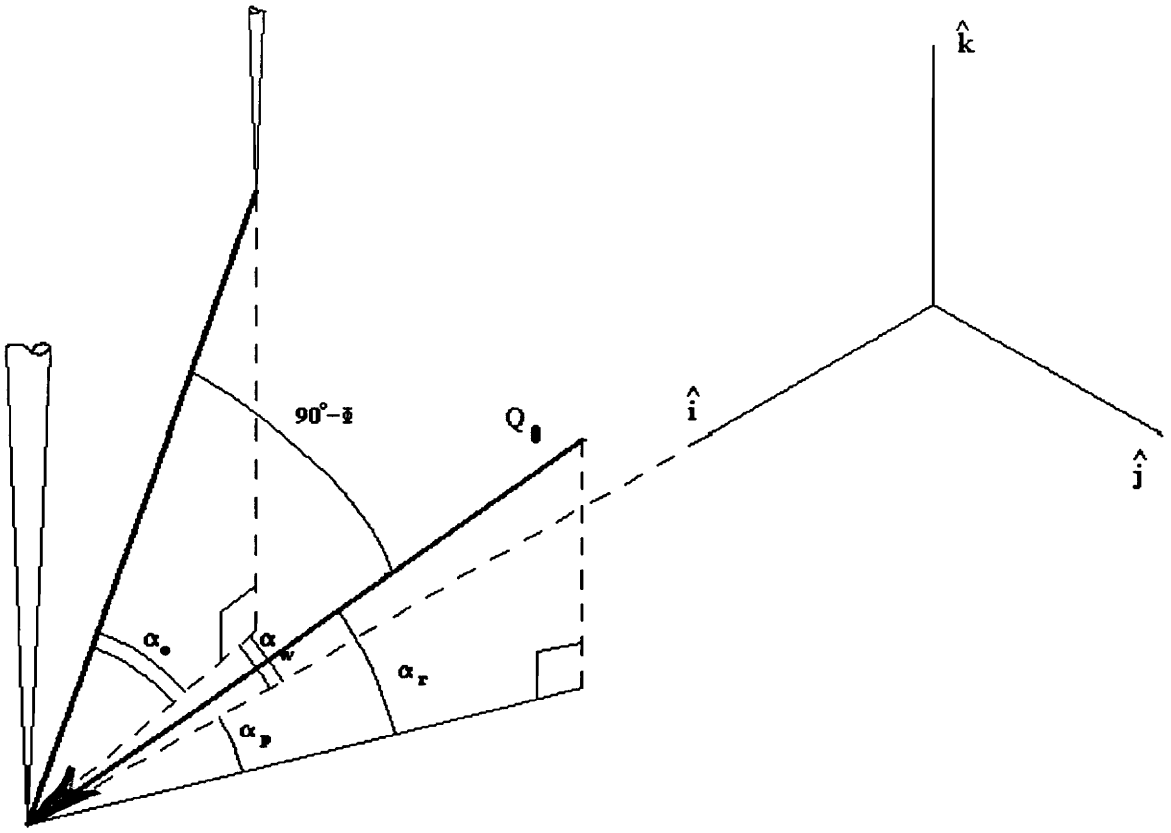

Figure C1. Geometry for Velocity Direction Solution

Appendix D
Development of the Hot Wire Equations

In this section, the equations used to determine the components of the stress tensor are developed after Gorton and Lakshminarayana [7] and Shaffer [3]. The final equations were written into Fortran programs (SP7.FOR for pipe flow and SPL.FOR for cascade flow) to simplify the calculation from mean and fluctuating hot wire voltage signals.

D.1. Linearized Hot Wire Response Equations

Consider a single hot wire with respect to the fixed coordinate system $(\hat{i}, \hat{j}, \hat{k})$. The hot wire has an orthogonal coordinate system (AX, N1, N2) attached to the wire as shown in Figure D1. The total instantaneous cooling velocity can be resolved into its components in the AX, N1 and N2 directions by applying the modified cosine law:

$$(Q+q) = \sqrt{(Q+q)_{N1}^2 + (Q+q)_{N2}^2 + k^2 (Q+q)_{AX}^2}\,. \tag{D1}$$

The three component cooling velocities can be related to the instantaneous velocities in the fixed coordinate frame by:

$$\begin{aligned}
(Q+q)_{AX} &= a_1(U+u) + b_1(V+v) + c_1(W+w) \\
(Q+q)_{N1} &= a_2(U+u) + b_2(V+v) + c_2(W+w) \\
(Q+q)_{N2} &= a_3(U+u) + b_3(V+v) + c_3(W+w)
\end{aligned} \tag{D2}$$

where $a_{1\text{-}3}$, $b_{1\text{-}3}$ and $c_{1\text{-}3}$ are the direction cosines (see section D.2).

Then equations (D2) are substituted into (D1), resulting in:

$$\begin{aligned} Q+q = [\,& a_4\left(U^2+u^2+2Uu\right)+b_4\left(V^2+v^2+2Vv\right) \\ & +c_4\left(W^2+w^2+2Ww\right)+d_4\left(UV+uv+Uv+uV\right) \\ & +e_4\left(UW+uw+Uw+uW\right)+f_4\left(VW+vw+Vw+vW\right)]^{\frac{1}{2}} \end{aligned} \tag{D3}$$

where $a_4,\ldots,f_4$ are groupings of the previous constants:

$$\begin{aligned} a_4 &= a_2^2+a_3^2+k^2a_1^2 \\ b_4 &= b_2^2+b_3^2+k^2b_1^2 \\ c_4 &= c_2^2+c_3^2+k^2c_1^2 \\ d_4 &= 2\left(a_2b_2+a_3b_3+k^2a_1b_1\right) \\ e_4 &= 2\left(a_2c_2+a_3c_3+k^2a_1c_1\right) \\ f_4 &= 2\left(b_2c_2+b_3c_3+k^2b_1c_1\right) \end{aligned} \tag{D4}$$

Then, Eq. (D3) is made linear by factoring $\sqrt{a_4}\left(U+u\right)$ from the right hand side, expanding by:

$$\sqrt{1+x} = 1 + \frac{x}{2} - \frac{x^2}{8} + \cdots,$$

and neglecting terms of order three or greater, resulting in:

$$\begin{aligned} Q+q = {} & a_5(U+u) + a_6(V+v) + a_7(W+w) \\ & + a_8\left(\frac{V^2}{U} + \frac{v^2}{U}\right) + a_9\left(\frac{W^2}{U} + \frac{w^2}{U}\right) + a_{10}\left(\frac{VW}{U} + \frac{vw}{U}\right) \\ & + a_{11}\frac{Vv}{U} + a_{12}\frac{Ww}{U} + a_{13}\left(\frac{Vw}{U} + \frac{vW}{U}\right) + O(\varepsilon). \end{aligned} \tag{D5}$$

where again the constants are groupings of the previous constants:

$$a_5 = \sqrt{a_4}$$

$$a_6 = \frac{d_4}{2}\sqrt{a_4}$$

$$a_7 = \frac{e_4}{2}\sqrt{a_4} \tag{D6}$$

$$a_8 = \sqrt{a_4}\left[\frac{b_4}{2a_4} - \frac{1}{8}\left(\frac{d_4}{a_4}\right)^2\right]$$

$$a_9 = \sqrt{a_4}\left[\frac{c_4}{2a_4} - \frac{1}{8}\left(\frac{e_4}{a_4}\right)^2\right]$$

$$a_{10} = \sqrt{a_4}\left[\frac{f_4}{2a_4} - \frac{1}{4}\left(\frac{d_4 e_4}{a_4^2}\right)\right]$$

$$a_{11} = \sqrt{a_4}\left[\frac{b_4}{a_4} - \frac{1}{4}\left(\frac{d_4}{a_4}\right)^2\right] \qquad (D6)$$

$$a_{12} = \sqrt{a_4}\left[\frac{c_4}{a_4} - \frac{1}{4}\left(\frac{e_4}{a_4}\right)^2\right]$$

$$a_{13} = a_{10}$$

Time averaging (D5) results in:

$$Q = a_5 U + a_6 V + a_7 W + a_8\left(\frac{V^2}{U} + \frac{\overline{v^2}}{U}\right) + a_9\left(\frac{W^2}{U} + \frac{\overline{w^2}}{U}\right) + a_{10}\left(\frac{VW}{U} + \frac{\overline{vw}}{U}\right) \qquad (D7)$$

By subtracting (D7) from (D5) an expression for instantaneous fluctuation is obtained:

$$q = a_5 u + a_6 v + a_7 w + a_8\left(\frac{v^2}{U} - \frac{\overline{v^2}}{U}\right) + a_9\left(\frac{w^2}{U} - \frac{\overline{w^2}}{U}\right) + a_{10}\left(\frac{vw}{U} - \frac{\overline{vw}}{U}\right) + a_{11}\frac{Vv}{U} + a_{12}\frac{Ww}{U} + a_{13}\left(\frac{Vw}{U} + \frac{vW}{U}\right) \qquad (D8)$$

Squaring (D8) and taking the time averaged results in a linear equation for $\overline{q^2}$ in terms of the Reynolds stresses:

$$\begin{aligned}\overline{q^2} = a_5^2\overline{u^2}[a_6^2 + a_{11}^2\left(\frac{V}{U}\right)^2 + a_{13}^2\left(\frac{W}{U}\right)^2 + 2a_6a_{11}\left(\frac{V}{U}\right) + 2a_6a_{13}\left(\frac{W}{U}\right)\\ +2a_{11}a_{13}\left(\frac{VW}{U^2}\right)]\overline{v^2} + [a_7^2 + a_{12}^2\left(\frac{W}{U}\right)^2 + a_{13}^2\left(\frac{V}{U}\right)^2 + 2a_7a_{12}\left(\frac{W}{U}\right)\\ +2a_7a_{13}\left(\frac{V}{U}\right) + 2a_{12}a_{13}\left(\frac{VW}{U^2}\right)]\overline{w^2} + \left[2a_5a_6 + 2a_5a_{11}\left(\frac{V}{U}\right) + 2a_5a_{13}\left(\frac{W}{U}\right)\right]\overline{uv} \qquad (D9)\\ +\left[2a_5a_7 + 2a_5a_{12}\left(\frac{W}{U}\right) + 2a_5a_{13}\left(\frac{V}{U}\right)\right]\overline{uw} + [2a_6a_7 + (2a_6a_{12+}2a_7a_{13})\frac{W}{U}\\ +(2a_6a_{13+}2a_7a_{11})\frac{V}{U} + \left(2a_{11}a_{12+}2a_{13}^2\right)\left(\frac{VW}{U^2}\right) + 2a_{11}a_{13}\left(\frac{V}{U}\right)^2 + 2a_{12}a_{13}\left(\frac{W}{U}\right)^2]\overline{vw} + o(\varepsilon)\end{aligned}$$

By multiplying (D8) for wire A by (D8) for wire B and time averaging, an equation for the mean product of the two wire signals is obtained:

$$\begin{aligned}\overline{q_Aq_B} = a_5b_5\overline{u^2} + [a_6b_6 + a_{11}b_{11}\left(\frac{V}{U}\right)^2 + a_{13}b_{13}\left(\frac{W}{U}\right)^2 + (a_6b_{11} + a_{11}b_6)\left(\frac{V}{U}\right) + (a_6b_{13} + a_{13}b_6)\left(\frac{W}{U}\right)\\ +(a_{11}b_{13} + a_{13}b_{11})\left(\frac{VW}{U^2}\right)]\overline{v^2} + [a_7b_7 + a_{12}b_{12}\left(\frac{W}{U}\right)^2 + a_{13}b_{13}\left(\frac{V}{U}\right)^2 + (a_7b_{12} + a_{12}b_7)\left(\frac{W}{U}\right)\\ +(a_7b_{13} + a_{13}b_7)\left(\frac{V}{U}\right) + (a_{12}b_{13} + a_{13}b_{12})\left(\frac{VW}{U^2}\right)]\overline{w^2} + [a_5b_6 + a_6b_5 + (a_5b_{11} + a_{11}b_5)\left(\frac{V}{U}\right)\\ +(a_5b_{13} + a_{13}b_5)\left(\frac{W}{U}\right)]\overline{uv} + [a_5b_7 + a_7b_5 + (a_5b_{12} + a_{12}b_5)\left(\frac{W}{U}\right) + (a_5b_{13} + a_{13}b_5)\left(\frac{V}{U}\right)]\overline{uw} \qquad (D10)\\ +[a_6b_7 + a_7b_6 + (a_6b_{12} + a_{12}b_6 + a_7b_{13} + a_{13}b_7)\frac{W}{U} + (a_6b_{13} + a_{13}b_6 + a_7b_{11} + a_{11}b_7)\frac{V}{U}\\ +(a_{11}b_{12} + a_{12}b_{11} + 2a_{13}b_{13})\frac{VW}{U^2} + (a_{11}b_{13} + a_{13}b_{11})\frac{V^2}{U^2} + (a_{12}b_{13} + a_{13}b_{12})\frac{W^2}{U^2}]\overline{vw} + O(\varepsilon)\end{aligned}$$

where b_5 ,....,b_{13} are the coefficients for wire B corresponding to the coefficients a_5 ,....,a_{13} for wire A in (D6). This final result gives three equations; (D9) for $\overline{q_a^2}$ *and* $\overline{q_b^2}$, (D10) for $\overline{q_a q_b}$. The mean velocities (U, V, W) are first solved for as in Appendix C then these three equations are solved for the stress tensor.

D.2. Relating (AX, N1, N2) Coordinates to ($\hat{i}$, $\hat{j}$, $\hat{k}$) Coordinates

The direction cosines in (C2) can be expressed in terms of the known angles α_o and α_w shown in Figure (D1). Figure (D2) shows a vertical stemmed probe with wire coordinate directions (AX, N1, N2) and fixed coordinate directions $(\hat{i}, \hat{j}, \hat{k})$. The unit vectors (AX, N1, N2) can be written in terms of their components in the $(\hat{i}, \hat{j}, \hat{k})$ directions as follows:

$$\begin{aligned} AX &= (\cos\alpha_0 \cos\alpha_w)\hat{i} + (\cos\alpha_0 \sin\alpha_w)\hat{j} - (\sin\alpha_0)\hat{k} \\ N1 &= -(\sin\alpha_w)\hat{i} + (\cos\alpha_w)\hat{j} + 0\hat{k} \\ N2 &= (\sin\alpha_0 \cos\alpha_w)\hat{i} + (\sin\alpha_0 \sin\alpha_w)\hat{j} + (\cos\alpha_0)\hat{k}. \end{aligned} \tag{D11}$$

The direction cosines for use in (D2) can then be written as:

$$\begin{aligned} a_1 &= \cos\alpha_0 \cos\alpha_w & b_1 &= \cos\alpha_0 \sin\alpha_w & c_1 &= -\sin\alpha_0 \\ a_2 &= -\sin\alpha_w & b_2 &= \cos\alpha_w & c_2 &= 0 \\ a_3 &= \sin\alpha_0 \cos\alpha_w & b_3 &= \sin\alpha_0 \sin\alpha_w & c_3 &= \cos\alpha_0. \end{aligned} \tag{D12}$$

For a given x-wire probe, the direction cosines are geometric constants.

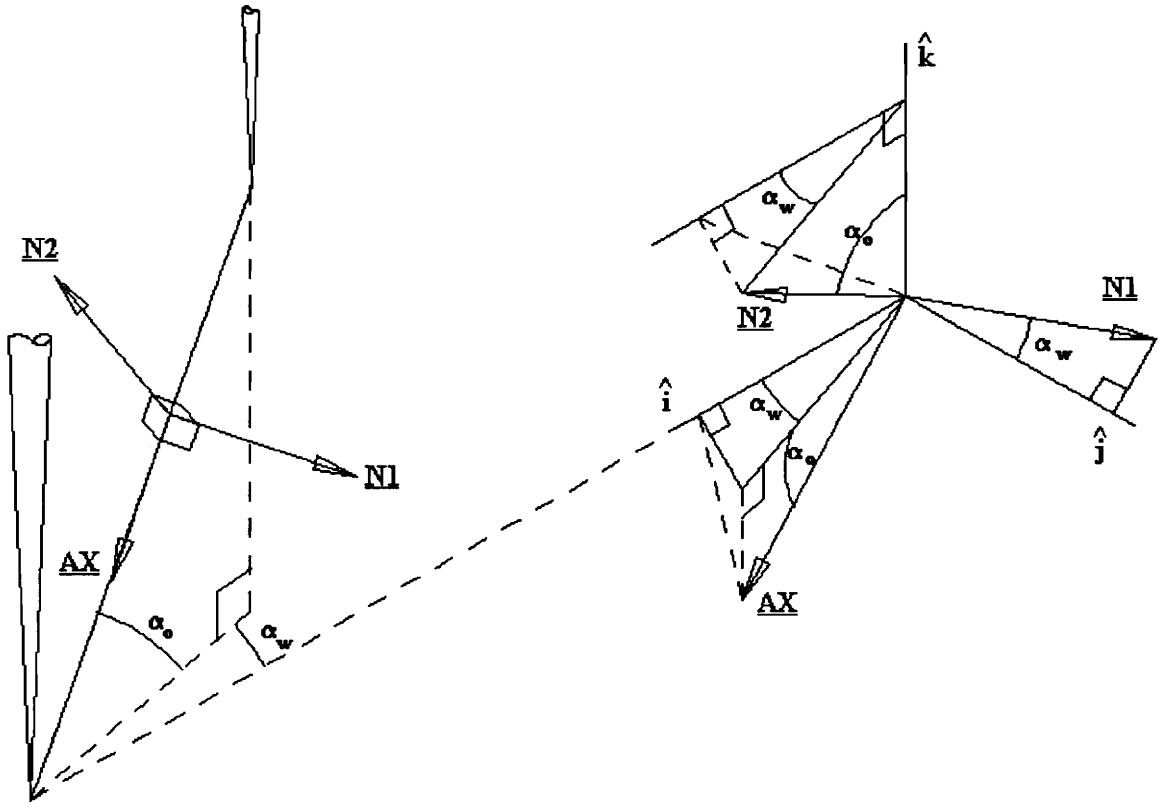

Figure D1. Geometry for Direction Cosine Evaluation

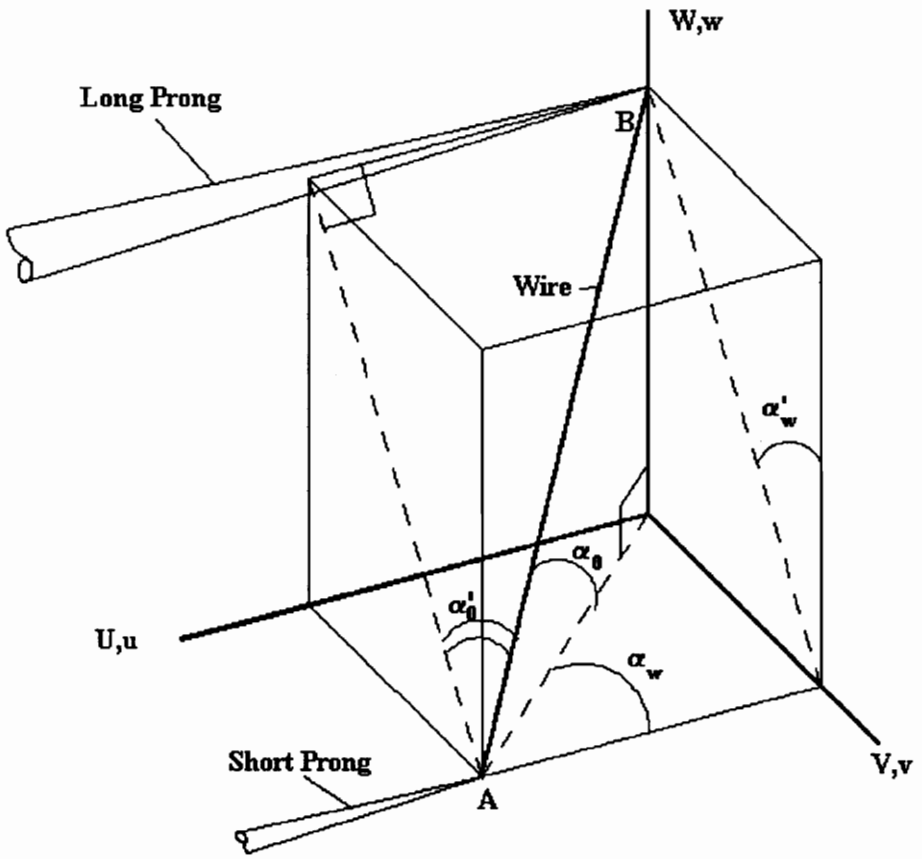

Figure D2. Probe Wire Geometry

D.3. Relating Voltages and Velocities

As discussed in Appendix B, the hot wire output follows a power law:

$$E^a = Q \tag{D13}$$

where E is the hot wire voltage, Q is the normalized fluid flow velocity and a is the wire linearity calibration constant.

The instantaneous voltage (E+e) is related to the instantaneous velocity (Q+q) by:

$$Q+q=(E+e)^a = E^a(1+\tfrac{e}{E})^a. \tag{D14}$$

This can be linearized by the expansion:

$$(1+x)^a = 1+ax+\tfrac{a(a-1)}{2}x^2+\cdots \quad .$$

By letting x=e/E and neglecting the higher order terms, (D14) becomes:

$$Q+q = E^a\left[1+a\left(\frac{e}{E}\right)\right]. \tag{D15}$$

Squaring both sides:

$$Q^2+2Qq+q^2 = E^{2a}\left[1+2a\left(\tfrac{e}{E}\right)+a^2\left(\tfrac{e}{E}\right)^2\right] \tag{D16}$$

Time averaging (D16) yields:

$$Q^2 + \overline{q^2} = E^{2a}\left[1 + \frac{a^2}{E^2}\overline{e^2}\right] \quad . \tag{D17}$$

By subtracting (D17) from (D16), assuming that $q^2 - \overline{q^2}$ and $e^2 - \overline{e^2}$ are negligible and rearranging with (D13) yields the following expression for the instantaneous velocity fluctuation q:

$$q = aE^{a-1}e = Le. \tag{D18}$$

Considering the two wires A and B, the wire response equations can be written:

$$\begin{aligned} \overline{q_A^2} &= L_A^2 \overline{e_A^2} \\ \overline{q_B^2} &= L_B^2 \overline{e_B^2} \\ \overline{q_A q_B} &= L_A L_B \overline{e_A e_B}. \end{aligned} \tag{D19}$$

Where L_a and L_b are known from the wire calibration constants, a, for wire A and wire B and $\overline{e_A^2}, \overline{e_B^2}$ *and* $\overline{e_A e_B}$ are obtained directly from the digitally processed hot wire signal.

Equations (D19) are then used as inputs to solve equations (D9A), (D9B) and (D10) for Reynolds stress.

Vita

Scott Patrick Heckel was born on June 7, 1969 in Appleton Wisconsin. He is married to his wife of two years, Cheryl, and is the father of one year old Layla. He received his Bachelor of Science in Mechanical Engineering in May of 1991 from the University of Wisconsin - Milwaukee. He entered graduate school in the Mechanical Engineering department at Virginia Polytechnic Institute and State University, Blacksburg, Virginia. Here he served as a Graduate Teaching Assistant for two semesters, teaching Mechanical Engineering Laboratory after which he served as a Graduate Research Assistant under the supervision of Dr. John Moore. He will obtain the degree of Master of Science in Mechanical Engineering in December of 1992.

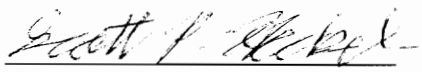

Scott P. Heckel